CURRENT RESEARCH IN SCIENCE AND MATHEMATICS

JUNE 2022

EDITOR
PROF. DR. HASAN AKGÜL

gece kitaplığı

İmtiyaz Sahibi / Publisher • Yaşar Hız
Genel Yayın Yönetmeni / Editor in Chief • Eda Altunel
Kapak & İç Tasarım / Cover & Interior Design • Gece Kitaplığı
Editör / Edıtor • Prof. Dr. Hasan AKGÜL
Birinci Basım / First Edition • © Haziran 2022
ISBN • 978-625-430-195-7

Gece Kitaplığı / Gece Publishing
Türkiye Adres / Turkey Address: Kızılay Mah. Fevzi Çakmak 1. Sokak Ümit Apt. No: 22/A Çankaya / Ankara / TR
Telefon / Phone: +90 312 384 80 40
web: www.gecekitapligi.com
e-mail: gecekitapligi@gmail.com

Baskı & Cilt / Printing & Volume
Sertifika / Certificate No: 47083

Current Research in Science and Mathematics

June 2022

Editor
Prof. Dr. Hasan Akgül

CONTENTS

CHAPTER 1

THE USAGE OF MICROMETRIC TURKEY FEATHER POWDER TO IMPROVE FUNDAMENTAL CHARACTERISTICS OF RIGID POLYURETHANE FOAM: THERMAL AND MECHANICAL ANALYSES

Ugur SOYKAN[1]

Seda KARABOGA[2]

1 Ugur SOYKAN, Assist. Prof. Dr., Bolu Abant Izzet Baysal University, Yenicaga Yasar Celik Vocational School, Turkey. 14300. Orcid ID: 0000-0002-9244-026

2 Seda KARABOGA, Research Assistant Dr., Bolu Abant Izzet Baysal University, Department of Chemistry, 14300, Turkey. Orcid ID: 0000-0003-2681-382X

1. An Overview on Rigid Polyurethane Foams

The polymer-based foamy materials can be seen as a significant member of the modern materials with their functional and wide usage potential in many areas such as industrial, architectural, medical, construction and buildings as well as buoyancy, cushioning, flotation (Chaturvedi, 2018). Polymeric foamy materials are produced from the plastic, elastomers and other polymer-based compounds with varying porosity levels, unique appearance and peculiar cellular structures. Such materials include the porous topology at which the gaseous molecules is surrounded by solid polymeric phase. Simply, the expanded version of the rubber, elastomer and plastics are called as polymeric foam. The combination of solid and gas phases in the matrix constitutes some particular and distinctive properties for the polymeric foams, which enables them to be used with the purpose of the insulation, soundproofing, permeation or water proofing. Moreover, thanks to their lightweight, high mechanical and peculiar microstructural features, the foamy polymeric materials has attracted much attention in the engineering fields, especially in the production of the vehicle interior and crashworthiness parts (Chen & Das, 2022; Khemani, 1997). Their noteworthy shock absorption and impact damping characteristics allow the scientist to fabricate more durable and strong foamy materials. The polymeric foam materials can be categorized into six main types in terms of the topological characteristics; open cellular, flexible, closed cellular, rigid, syntactic and reticular, as depicted in Figure 1. In more detail, there is an interconnection between holes and cells in the open cellular polymeric foams, while there does not exist a interconnection between hole and cells in the closed cellular polymeric foams. Flexible polymeric foams can easily bend and flex without any formation of cracks and delimitation, whereas rigid polymeric foams have slight or no flexibility (Wolfe & Reges, 1972). Reticular polymeric foams possess the open structure. (Feldman, 2010). Finally, syntactic foams make up of the rigid microspheres or glass micro-holes connecting the matrix (Rittel, 2005).

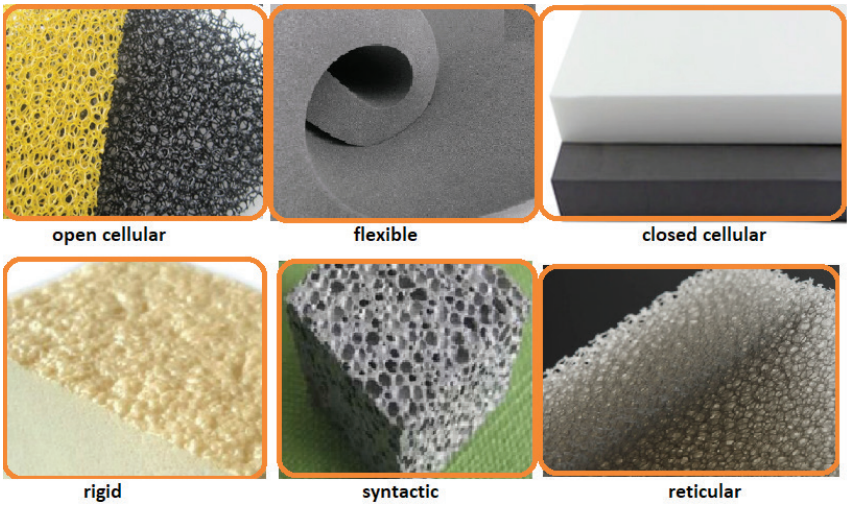

Figure 1. Types of polymeric foam materials in term of the cellular structures.

It is well know that there exists lots of plastic foamy materials such as polyurethane, polyisocyanurate, polyamide, polyimide, polyurea and polycarbodiimide and, they are fabricated with the method of the polyaddition, polycondensation and polycyclotrimerization reactions (Y. Liu, Qin, & Tang, 2018). Among these mentioned polymeric foams, polyurethane plays a critical role in the world polymer industry thanks to their wide usage fields such as wound dressing application, surface coating, thermal insulation, textiles, the production of the vehicle components, soft sponge, food packaging, shoes, electronic device etc (Akindoyo et al., 2016). Polyurethanes are formed as a result of the polyaddition chemical reaction taking placing between reactive hydroxyl (-OH) and isocyanate (-NCO) groups to established urethane linkages (-NH-CO-O-) in the main polymer backbone. These reactive molecules bearing hydroxyl and isocyanate groups in their molecular structure may be di, tri or polyfunctional. The functionality degree of the components undoubtedly determines how the main characteristics of the final polyurethane product are. That is, the variation of the reactants in terms of functionality brings about the fabrication of lots of polyurethane types (Lee, Park, & Ramesh, 2007). For example, in order to obtain the polyurethane having linear polymer chains, difunctional reactants must be used, whereas, in order to produce crosslinked polyurethane, it must be chosen the polyfunctional reactants. It must to be state herein that, among polyurethane based foam materials, the rigid polyurethane foams (RPUFs) are more favorable one since the production value of RPUFs in the world reached 5 million metric tones in 2020 and, it is estimated that this value will become

roundly 81 billion $ trade volume in 2023 (Mahmood, Yuan, Schmidt, Tymchyshyn, & Xu, 2016). RPUFs are the specific materials consisting of the honeycomb shaped polyurethane closed walls and struts in which the gaseous molecules are encapsulated. RPUFs are produced with the reaction between polyol and polyisocynate. Synthetic and plant-based polyether polyol, polyester polyol or polyolefins with hdroxly groups with terminal position are utilized as a polyol, whereas methylene diphenyl diisocyanate (MDI), toluene diisocyanate (TDI) or aliphatic diisocyanates were used an isocyanate source (Anthuvan, Kalaignan, & Vincent, 2011; Jalilian, Yeganeh, & Haghighi, 2008). At the production mechanism of RPUFs, gas generation has critical significance since it provides the occurrence of the peculiar cellular structure with substantial porosity. The materials forming the gas during foaming reaction are defined as the blowing agent (Yakushin, Cabulis, Fridrihsone, Kravchenko, & Pauliks, 2021). CO_2 gas is generated as consequence of the exothermic reaction between isocyanate and water used as a blowing agent as shown simply in Figure 2. Additionally, since the foaming process of polyurethane is considerably sophisticated and indicates delicate equilibrium, the addition of some additives like catalyst and surfactant are required. They establish a balance among the blowing (to form CO_2), gelling (to form polyurethane) and trimerisation (to form related polymerization of pMDI) reactions (Gu, Lyu, Cheng, & Liu, 2021). As for the surfactant, the main role of the surfactant in the foaming process of polyurethane is to make stable the cellular structures of the foam by reducing the surface tension between the gas and solid phases in the matrix during foam rising.

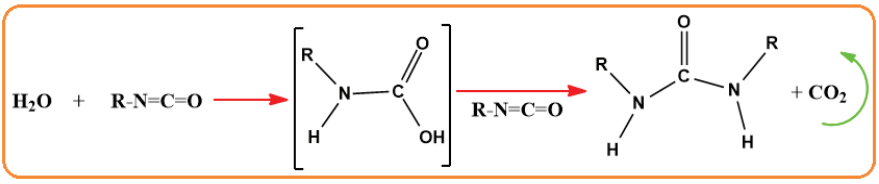

Figure 2. *Simplified reaction between isocyanate and water to produce CO_2 blowing agent.*

Chemically, the foaming systems are performed using three types of polymerization reaction mechanism. These are one-step one-shut (one-shut free rise), quasi pre, full-pre polymerization methods (Iqbal, Mubashar, Ahmed, Arif, & Din, 2022; Mahmoud, Nasr, Zulfiqar, Sarwar, & Maamoun, 2021; Xue & Sun, 2015). In one-shut free-rise method, Component A (contains only polyisocyanate) and component B (includes catalyst, blowing agent, surfactant as well as polyol) are prepared separately and mixed according to the certain volume ratio to form foam, as described in Figure 3.

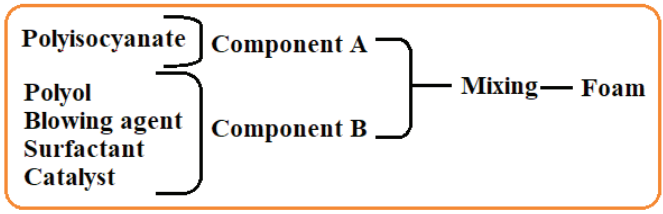

Figure 3. *One-shut one step polymerization system.*

In quasi pre polymer system, Component A is composed of both polyisocyanate and polyol, while Component B is formed by the combination of catalyst, blowing agent, surfactant and polyol, as seen in Figure 4.

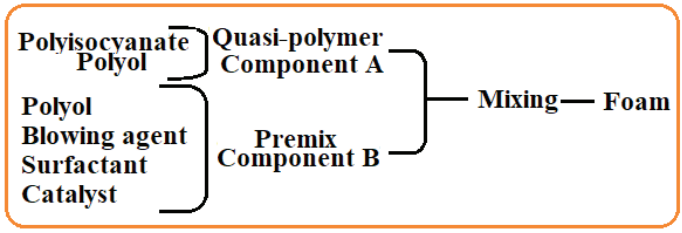

Figure 4. *Quasi pre polymerization system*

Finally, in full-pre polymerization system, first polyol and polyisocyanate are mixed and then, the other reagents such as blowing agent, surfactant and catalyst are added in this previously prepared mixture, as shown in Figure 5.

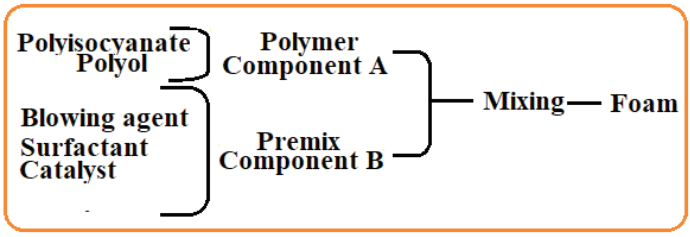

Figure 5. *Full-pre polymerization system.*

2. Bio-Based Filler Usage in Rigid Polyurethane Foams

Since conventional polymers do not decompose in short time in nature, bio-based polymers has attracted more attention on the global world where the environmental pollution has reached to the serious and dangerous level. Because of that, the researchers recently have tried to find the bio-degradable polymeric materials as well as to produce the

novel, polyfunctional bio-based and naturally sourced fillers in order to both improve the present polymeric materials and reduce their ecological damages (Helanto, Matikainen, Talja, & Rojas, 2019; Vaisanen, Das, & Tomppo, 2017). With this perspective, lots of properties can be imparted to the polymeric materials with the use of such green fillers in the form of the fiber or particle (powder) since the bio-based fillers are sustainable, cheap, low-density (roundly 45 % lower than the glass fiber (Bledzki, Zhang, & Chate, 2001)) and easy-producible (Tao, Li, & Cai, 2016). Bio-based fillers generally consists of ether, ester and amide functional groups which are decomposed easily by the bacteria. Thus, they have little or no harm to the environment since the naturally byproducts like carbon dioxide, water, nitrogen gas, biomass and salts are generated during their decomposition. It is well-known that such fillers were utilized for the improvement of RPUFs (Akdogan & Erdem, 2021; Kuznia et al., 2021; Leszczynska et al., 2021). Correspondingly, in several studies, in order to augment their reactivity or functionality in the RPUF matrix, the natural fillers were exposed to some treatments (Czlonka, Strakowska, & Kairyte, 2020; Qiu et al., 2021; Strakowska, Czlonka, & Kairyte, 2020). These used fillers for RPUFs generally are plant-based, animal-sourced and polymer based materials in various structural forms. Depending on that, several studies have been reported. For examples, the effect of cellulose fibers obtained from pineapple (Ananas comosus) leaf on the mechanical characteristics of RPUF was studied by Jabbar et al (Jabber, Grumo, Alguno, Lubguban, & Capangpangan, 2021). They found that the increasing of the content level of the cellulose fiber in RPUF matrix gave rise to the consistent decrement in both the compressive strengths and apparent densities of the resulting foams due to the fact that the cellulose fibers limited or hindered the reactivity of the components during the foam expansion. In another study, the coconut coir fibers were used to reinforce RPUFs (Azmi, Yusoff, Abdullah, & Idris, 2012). The obtained results revealed that the densities of the produced foams decreased as the coir fiber content increased, and especially, the foam with 5 % of coir fiber showed better maximum force and shear stress, which were recorded as 88 N and 60 KPa, respectively. This result was believed to be caused form the formation of considerable effective interfacial adhesion between RPUF matrix and coir fibers, which provides the sufficient resistance against to the deformation when the external force was applied. Moreover, Li et al. dealt with the production of kenaf fiber-filled RPUF via one shut free rise method and their dielectric features depending on the temperature and fiber content (Li, Tao, & Shi, 2014). They reported that the addition of the kenaf fiber into RPUF matrix brought about the enhancement in both the dielectric constant and loss tangent. That is, with this study, it was found that the ability of the energy dissipation and the dielectric capability of RPUF could be

improved by using natural fiber. Furthermore, several researches focusing of the usage of the wood flour (including naturally free -OH groups with chemical bonding potential) as a filler for the reinforcement of RPUF have announced in the literature. Namely, Yuan and Shi produced wood flour-added RPUF by reducing 20 % of polyol by the weight and, the mechanical and thermal stability properties of the fabricated foams were investigated (Yuan & Shi, 2009). The incorporation of wood flour with RPUF matrix improved both the thermal stability and compressive modulus (about 19 %) of the resulting foam composites. The similar results were also obtained in the studies reported previously (Aranguren, Gonzalez, & Mosiewicki, 2012; Mosiewicki, Dell'Arciprete, Aranguren, & Marcovich, 2009). In addition to that, adding of plant-sourced natural fillers into RPUF matrix affects considerably the insulation and permeability properties of RPUFs. By adding proper and favorable natural fillers, thermal insulation, sound absorption, gas and water permeability properties of RPUF can be modified since such characteristics depends highly on the interaction between the components, vacancy level of the foam, cellular topology of the foam, foaming process etc (Kuranska & Prociak, 2012). In our previous study (Khaleel, Soykan, & Cetin, 2021), the turkey feather fibers having substantially amount of the honeycomb shaped micro cells were used as a filler to improve RPUF. The addition of turkey feather fiber to RPUF yielded noteworthy contribution to the thermal insulation, sound absorption performances as well as thermal stability. Moreover, Bakare et al studied RPUF filled with sisal fibers. They reported that RPUF producing by using the sisal fibers provides better insulation and mechanical performances (Bakare, Okieimen, Pavithran, Khalil, & Brahmakumar, 2010). Shortly, as apparently seen above, various properties of RPUF can be modified by using the naturally sourced fillers as a secondary materials in the matrix.

3- Materials and Methods

In this part of study, the used materials and experimental procedures were given in detail. The main components, polyol and diphenylmethane di-isocyanate (MDI), to fabricate RPUFs via one-shut free-rise method, were supplied from Kimteks Chemistry Textile Products Trade Incorporated Company (Istanbul, Turkey). The main structural features of these components were meticulously given in Table 1 as taken from the company as previously reported (Soykan, 2022). The TFPs powders produced directly from waste turkey feathers were kindly taken from Bolca Hindi (Erpilic, Bolu, Turkey), the images of TFPs were presented in Figure 6. The volume-weighted mean of TFPs was determined as 382.111 μm. Moreover, it must to be stated that the supplied TFPs were dried at 80 °C before using for the foam composites.

Table 1. *The characteristics of polyol and polymeric isocyanate (pMDI) (Soykan, 2022).*

Materials	Properties	Values
Polyol	Density (20 °C)	1.03 g/cm^3
	Viscosity (25 °C)	400.0 m.Pa.s
	Acid value	<1
	Functionality	4
	Hydroxyl value	265 mgKOH/g
PMDI	Density (20 °C)	1.23 g/cm^3
	Viscosity (25 °C)	2.5 m.Pa.s
	NCO content	31.5
	Functionality	2.8

Figure 6. *Micro-sized turkey feather powders (TFPs).*

The production of both reference RPUF and TFPs-loaded RPUF was performed by vigorously mixing of the polyol (65 ml) and polyisocyanate (78 ml) with the volumetric ratio of roundly 0.83 in the closed mold having 250×250×50 mm^3 volume at 45 °C reaction temperature. One-shut free rising method was used in this polymerization reaction. The percentage of TFPs in the foam specimens varied in the range of 3-15 wt.%.

The obtained foam samples were analyzed by taking into consideration the thermal behavior and mechanical performance. Thermal properties were evaluated by using Shimadzu TA-60 WS Differential Scanning Calorimeter (DSC, Shimadzu, Japan) and Perkin–Elmer Diamond Thermogravimetric Analyser (TGA, Perkin Elmer In., Shelton, USA), while mechanical performance of the foam specimens were examined by means of universal mechanical test machines. The tensile and compression strengths of the test samples were determined by means of BESMAK (Besmak Inc., Ankara, Turkey) according to ASTM D1623-09 standard (Yu, Choi, Nam, & Lee, 2014) and ASTM D1621-1 standard (Peng et al., 2019), respectively. The impact tests were carried out using Testform SDTC impact test machine (Testform, Ankara, Turkey) according to ISO 179-1 standard (Njuguna et al., 2021).

4-The Effect of TFPs Adding on Thermal Behavior of the Produced RPUFs

Since RPUFs are highly combustible organic material, the thermal behavior of them becomes significant phenomenon in their usage areas. Especially, in the buildings, constructions, walls, flooring, car components, roofing, domestic refrigerators, freezers, which are indispensible parts of the people daily life, the importance of this aspect is better understood. Having more flammability of RPUFs may cause both growing of the fire destruction during a fire accident and releasing of lots of the corrosive and toxic gases like CO_2, CO, NO, NH_3, benzene, toluene, HCN, HCl, HF, HBr during its combustion and ignition (Son, Kim, Jo, & Kwon, 2021; Vitkauskiene, Makuska, Stirna, & Cabulis, 2011; Wang, Chen, & Zhang, 2014). These generated gases have asphyxiant effects and, may leads to the death of the people during fire (Ikegaya et al., 2001; Piantadosi, 2004; Son et al., 2021). So as to cope with this apparent major drawback, lots of studies trying to improve the thermal stability of RPUF were done by applying several physical and chemical modification (Pang, Xin, Shi, & Xu, 2019; Xing et al., 2013; W. Zhou, Bo, Jia, Zhou, & Zhang, 2019). Such modifications mainly base on reducing its flammability, limiting amount of emitted smoke and hindering the toxicity and corrosiveness of the released gases (Oliwa et al., 2021). Accordingly, with this purpose, the flame retardant compounds generally are used to gain thermal stability to RPUF since they make RPUF low flammable and more durable against degradation when exposured to the elevated temperature. (F. Zhou et al., 2020). The main role of the flame retardants is to decrease the emission of smoke and heat by decelerating the degradation and ignition of RPUFs. Moreover, in the literature, the studies focusing on the usage of the filler particles was encountered to impart thermal stability to RPUFs (D. Y. Liu, Zhao, Wang, Liu, & Liu, 2018; Pham et al., 2020). Thermal stability of filler-loaded RPUFs is dependent on the degree of aromatic segments in the molecular structure of polyol, filler properties, the chemical interaction between foam matrix and filler, isocyanurate content level, crosslinking degree in RPUF matrix and degree of crystallinity of RPUFs etc (Vitkauskiene et al., 2011). In more detail, the increment in the aromatic fragments in the chain backbone of polyol brings about that RPUF illustrates better thermal stability thanks to that aromatic rings are more chemically stable than aliphatic one (Awasthi & Agarwal, 2007). Moreover, the presence of more isocyanurates into RPUFs matrices provides thermal (fire) resistance since the isocyanurates are more stable compared to urethane bonds (Modesti & Lorenzetti, 2003). Additionally, the formation of strong primarily or secondary chemical bonds between the components also creates the positive effect on the thermal stability of RPUFs (Z et al., 2022) since such

molecular interactions provides the retardation thermal decomposition of RPUF by increasing the temperature value at which the degradation begins. All in all, the thermal stability of RPUFs are highly dependent on the chemical structures of the components, physical characteristics of components and interaction between components in the reaction mixture during foaming. Thus, in this part of current study, for clear understanding, the effect of TFPs addition on the thermal behavior of both reference RPUF and TFPs-filled RPUFs was investigated meticulously by means of differential scanning calorimeter (DSC) and thermogravimetric analysis (TGA) techniques. The obtained thermograms and change in weight-loss (%) with the temperature for all produced foam samples were presented in Figure 7 and 8, respectively. DSC results showed that there was no apparent endotherm showing that the melting temperature of soft segment (at about 60 °C). However, it was seen a small shoulder at about 310 °C, which was attributed to the liquefaction temperature of TFPs due to its mostly keratin structure. Furthermore, the broad exothermic peaks detected between 380-395 °C was believed to be caused from the occurrence of some omnipresent exothermic reactions between the compounds produced during the combustion. The similar results were announced in the study done by He et al (He et al., 2008).

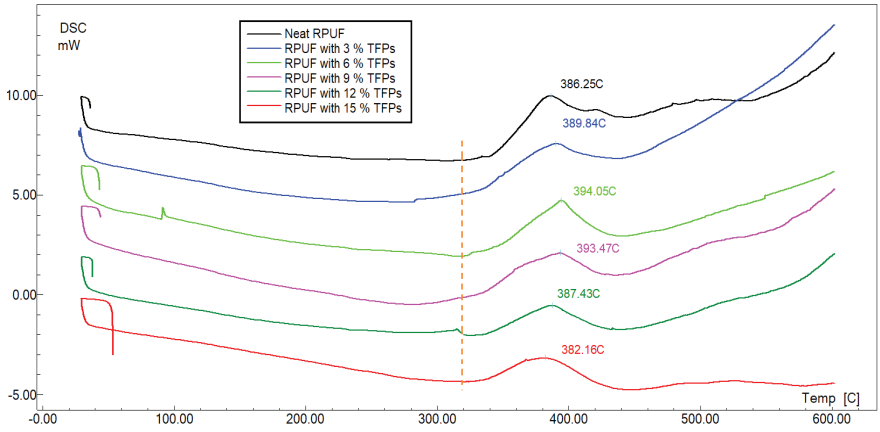

Figure 7. *DSC thermograms of all the produced foam specimens.*

As for TGA analysis carried out in N_2 atmosphere, one can see easily decomposition behavior of neat TFPs and RPUF as well as all TFPs-loaded RPUFs samples from Figure 8. It was found that the temperatures at which neat TFPs reached about 1.0 % and 5.0 % weight losses were 84 °C and 216 °C, respectively. Moreover, the serious weight loss, which was equal to roundly 55.0 % for neat TFPs was recorded in the range of 230-370 °C. This weight loss was apparently corresponded to the breaking of

the peptide bonds in the keratin protein, which results in the occurrence of volatile conventional fire gases when burning of protein based materials (Popescu & Augustin, 1999). Furthermore, the obtained results depicted that neat TFPs possessed higher amount of residue among the materials analyzed. Correspondingly, at about 600 °C, the amount of residue was found to be approximately 20 % for TFPs. When examining TGA curve of neat RPUF, the first weight loss (about % 1) was observed at 193 °C, which was attributed to the decomposition of rigid segments of RPUF accompanied by the dissociation of chemical linkages of urethanes. Moreover, it was obvious from the figure that neat RPUF lost considerable weight (~83 %) in the temperature range of roundly 270-310 °C, which was presumably related to decomposition mechanism of soft segments of polyurethane polymer. The minimum residue, about 11 %, at 600 °C was also obtained with neat RPUF. As for TFPs-added RPUFs, it was seemed that loading of TFPs into RPUF matrices created the slight effect on the thermal behavior. Especially at the foam sample with 9.0 % of TFPs, as deduced from relevant TGA curve, little thermal stability was gained to RPUF. Interestingly, the relatively higher mechanical performances were also recorded at this content (Figure 9). This could be seen an experimental sign regarding that that strong chemical bonds between the functional groups in both polyurethane and keratin chains were formed. This meant that the taking place of novel chemical crosslink bridges and linkages in the matrices, which makes RPUF more endurable against the thermal degradation. However, this effect was not remained with the increasing of TFPs content level in the matrices. As seen from the figure, especially at the foam specimens with 12.0 and 15.0 % started to degrade at relatively lower temperatures compared to the foam specimens with low contents and, 10.0 % of weight losses were reached at 297 °C and 294 °C for these foam samples, respectively.

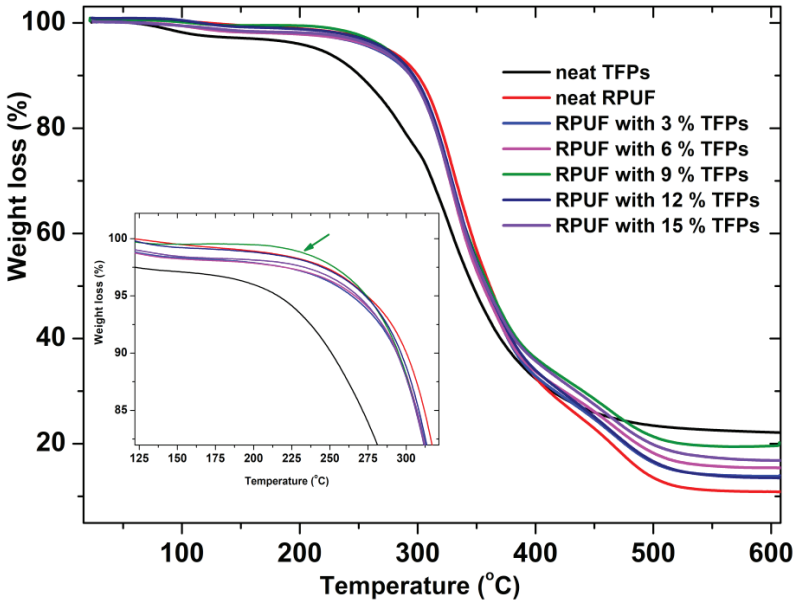

Figure 8. *TGA decomposition curves belonging to all the produced foams in N_2 atmosphere.*

5-The Effect of TFPs Adding on Mechanical Performance of the Produced RPUFs

Since RPUF materials are widely utilized in the global world industry, it is required that they must also be strong and endurable against external impacts and other mechanical threats. In this regard, secondary materials like fillers can be used in order to increase the mechanical performance of RPUFs. However, while providing this mechanical reinforcement, it is apparent fact that several parameters regarding to the fillers such as type, size and shapes, chemical and microstructural structure, content level, compatibility with RPUF, reaction possibility with RPUF component must be taken into account (Akdogan & Erdem, 2021; Cheng, Shi, Zhou, & Chen, 2014; Yurtseven, Tarakcilar, & Topcu, 2013). The used filler for this purpose can be in fibrillated form or particle form with regular or irregular structure and different size. The characteristics properties of fillers affected directly the final performance of the foams since it causes noteworthy changes in the cell structure, regularity of cells, distribution and level of closed cells of the foams as well as kinetics and foaming process in the reaction medium (Czlonka, Kairyte, Miedzinska, & Strakowska, 2021). For instance, the decrement in the surface energy of the fillers by exposed pre-treatment like surface treatment brings about the relatively lower agglomeration or accumulation when the fillers were mixed with the polyol. Consequently, these well-dispersed fillers can act

as a tertiary component hindering the continuity of the cell during cell formation, which results in the occurrence of distorted and ruptured cell walls, edges and struts (Kerche, Bock, Delucis, Magalhaes, & Amico, 2021; Kerche, Delucis, Petzhold, & Amico, 2021). Thus, such final foams may show lower mechanical performance. On the other hand, the addition of the fillers in the form of fibril may improve the mechanical properties of the rigid polyurethane foam since they enhance the alignment and orientation of the polymer chains during foaming process. In fact, such fillers actuate as a nucleating agent, which brings about the augmentation in the number of closed cells accompanied by the decrement in the cell diameters accompanied by reducing of the cell anisotropy (Czlonka, Sienkiewicz, Strakowska, & Strzelec, 2018). That is, the features of the fillers may change the mechanical performance of RPUF by influencing nucleation process during polymerization reaction. In addition to the characteristics of the used fillers, the production method, cell topology, main materials for manufacturing and the pressure of the gas generated during the polymerization reactions affect the mechanical performance of the resulting RPUFs (Srivastava & Srivastava, 2014). Moreover, these parameters also indicates the apparent density of the final RPUFs.

In the light of that mentioned above, in order to figure out the effect of the micron sized TFPs particle content level on the mechanical properties of RPUFs, the variations in the tensile, compression and impact strengths of RPUFs were discussed in this part of the study. The the calculated data corresponding to the tensile and compression strengths and the obtained relevant curves regarding the mechanical behaviors during tests were presented in Table 2 and Figure 9, respectively. As for the tensile test results, one can see from the figure that, all the manufactured RPUFs including TFPs showed lower mechanical performance with the comparison of neat RPUF and, correspondingly, the minimum tensile strength, 55.68 kPa was recorded with the RPUF product containing 15.0 % of TFPs. This results was presumably caused by that the chosen fillers damaged the regular occurrence of cell walls, struts and edges in the matrices although there existed lots of common functional groups having the potential to form secondary bonds in the chemical structures of both. These interferences probably brought about the relatively lower interfacial adhesion between components, which ends up that the produced RPUFs depicted lower tensile strength. Interestingly, when evaluating only RPUFs with TFPs, the initial addition of TFPs into the matrix led to the increment in the tensile strength. Among these foam specimens, the maximum tensile strength value was found to be 118.80 kPa at 6.0 % TFP content level. This result revealed that TFPs particles assisted the stress transfer distribution throughout the matrix although the addition of TFPs damaged the general cell regularity

when compared to neat one. The similar behavior was encountered in the study done with Kairyte et al (Kairyte et al., 2019) However, at high contents, the results showed that the presence of relatively high number of TFPs in the RPUF matrix inhibited the formation of the desired and strong cell morphology. Additionally, since the free movement ability of the polyurethane chains was presumably reduced due to TFPs, it was seen that the polymer chains belonging to RPUF could not easily distribute the applied tensile force throughout the matrix. As a result of these negative dual effects, the cell walls and struts become more thinner and flimsy, thus lower tensile strengths were recorded at high TFPs content. Regarding the compression tests, the similar tendency like tensile strengths was observed in the foam products. That is, the compression strength of the foam specimens decreased with the increasing of the percentage of TFPs in the matrix. The minima, 0.136 kPa was recorded with RPUF containing 15.0 % of TFPs, whose value was almost twice less than the value that neat RPUF had (0.238 kPa). This was apparently related to the damaging of cell morphological structure as revealed form tensile tests. Namely, the presence of high number of micron-sized TFPs in the matrix probably led to breaking or rupturing of cell walls as well as the formation relatively weaker cell struts. Consequently, this meant the reduction of the buckling levels of the matrix, thus the applied compression force did not distributed efficiently inside the matrix, which results in the lower compression strength. Moreover, since TFPs had inhomogeneous particle size distribution, at high contents, it seemed that the cellular structure of the foam specimens distorted. In short, the obtained results from both tensile and compression tests showed that the optimum addition content level of TFPs to produce mechanically improved RPUF was 6.0 %, as clearly observed in Figure 9.a and b.

Table 2. *Tensile and compression strength results belonging to produced foam samples*

Specimens	Tensile strength (kPa)	Compression strength (kPa)
Neat RPUF	196.29±0.32	0.238±0.005
RPUF with 3.0 % TFPs	98.88±2.36	0.168±0.005
RPUF with 6.0 % TFPs	118.80±3.71	0.189±0.011
RPUF with 9.0 % TFPs	89.68±2.88	0.166±0.008
RPUF with 12.0 % TFPs	71.12±2.34	0.148±0.006
RPUF with 15.0 % TFPs	55.68±1.95	0.136±0.014

Furthermore, the function of micron sized-TFPs addition on the Charpy impact strength of the foam samples was also examined in this study. The

change in the impact strengths of the foam with TFPs was schematically depicted in Figure 9.c with the standard deviations. At first glance at the figure, it could be said that the first addition of TFPs gave rise to slight improvement in the impact energy absorption ability, but not noteworthy. It almost remained plateau. In relation to that, the impact strength of the reference foam was found to be 2.05 kj/m^2, whereas it was recorded as 2.08 kj/m^2 at the foam with 6.0 % of TFPs. It must be also stated here that the better impact performance was observed at 6.0 % at which the maximum tensile and compression performances were also recorded at this content. However, at TFPs content greater than 6.0 %, the impact strengths showed the decreasing trend and, at 15.0 % of TFPs, reached to minima (1.90 kj/m^2) among all the produced foams, whose value was 7.3 % smaller than those of reference RPUF. The impact test findings also showed that the over addition of TFPs had a negative effect on the mechanical properties. This was probably due to the reduced molecular mobility of the hard polyurethane chains responsible for the mechanical properties as well as due to the inability to effectively distribute the applied impact force due to the irregularity in the cell structures in the matrix.

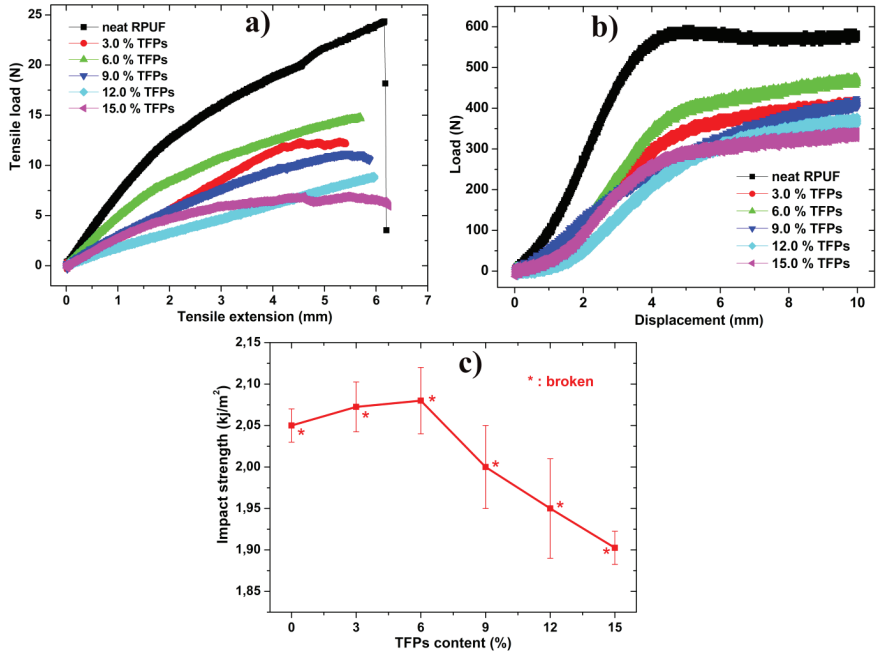

Figure 9. *a) Load versus extension curves, b) load-displacement graph and c) impact strength of the produced foams containing varying amount of TFPs.*

6- Conclusion

In this comprehensive study, the preparation, thermal properties and mechanical performance of rigid polyurethane foams (RPUFs) loaded with the micron-sized turkey feather powder (TFPs) were studied in detail for the first time. The production of TFPs as a novel filler was performed by the effective grinding process, and used as received from the company after drying. Both neat RPUF and TFP-filled RPUFs were fabricated with the method of one-shut one step polymerization. The thermal and mechanical behavior of these produced samples were investigated meticulously with DSC, TGA and universal mechanical test techniques by taking into consideration the content level of TFPs in the foam matrices. The thermal analysis of the foam samples showed that the incorporation of TFPs with RPUF gained slightly thermal stability to RPUF although neat TFPs began to degrade at low temperature. Adding of TFPs into RPUF led to decrement in the mechanical performance when compared to reference RPUF due to the fact that TFPs hindered the regular-shaped cellular topology. However, among TFPs-loaded RPUFs, the presence of TFPs created positive effect on the mechanical property. It was concluded that tensile, compression and impact tests unveiled that the optimum TFPs loading level was 6.0 %. All things considered, this study presented the novel potential usage area of TFPs being a green filler obtained from turkey feather wastes and revealed the crucial results showing a roadmap for usage of TFPs in RPUFs.

Acknowledgments

This work was supported by BAIBU research fund with the grant number of BAP 2020.29.02.1474. Furthermore, the authors wishes to express his deepest gratitude to Kimteks Chemistry Textile Products Trade and Erpiliç company for supplying of the raw materials for the production of foams and the turkey feather powders, respectively. In addition, the authors thank Assoc. Prof. Dr. Sedat ÇETİN for allowing us to use his laboratory for conducting the experimental procedures.

REFERENCES

Akdogan, E., & Erdem, M. (2021). Improvement in physico-mechanical and structural properties of rigid polyurethane foam composites by the addition of sugar beet pulp as a reactive filler. Journal of Polymer Research, 28(3).

Akindoyo, J. O., Beg, M. D. H., Ghazali, S., Islam, M. R., Jeyaratnam, N., & Yuvaraj, A. R. (2016). Polyurethane types, synthesis and applications - a review. Rsc Advances, 6(115), 114453-114482.

Anthuvan, J. T., Kalaignan, G. P., & Vincent, B. J. (2011). Synthesis and Characteristics of Two Component Polyurethane Coatings Based on Epoxy Polyol with Polyisocyanate. Asian Journal of Chemistry, 23(9), 4130-4134.

Aranguren, M. I., Gonzalez, J. F., & Mosiewicki, M. A. (2012). Biodegradation of a vegetable oil based polyurethane and wood flour composites. Polymer Testing, 31(1), 7-15.

Awasthi, S., & Agarwal, D. (2007). Influence of cycloaliphatic compounds on the properties of polyurethane coatings. Journal of Coatings Technology and Research, 4(1), 67-73.

Azmi, M. A., Yusoff, M. F. C., Abdullah, H. Z., & Idris, M. I. (2012). Rigid Polyurethane Foam Reinforced Coconut Coir Fiber Properties. International Journal of Integrated Engineering, 4(1), 11-15.

Bakare, I. O., Okieimen, F. E., Pavithran, C., Khalil, H. P. S. A., & Brahmakumar, M. (2010). Mechanical and thermal properties of sisal fiber-reinforced rubber seed oil-based polyurethane composites. Materials & Design, 31(9), 4274-4280.

Bledzki, A. K., Zhang, W. Y., & Chate, A. (2001). Natural-fibre-reinforced polyurethane microfoams. Composites Science and Technology, 61(16), 2405-2411.

Chaturvedi, A. (2018). Recent developments in the field of metal foam-polymer hybrid materials: A brief overview. Journal of Metals Materials and Minerals, 28(1), 136-140.

Chen, Y. M., & Das, R. (2022). A review on manufacture of polymeric foam cores for sandwich structures of complex shape in automotive applications. Journal of Sandwich Structures & Materials, 24(1), 789-819.

Cheng, J. J., Shi, B. B., Zhou, F. B., & Chen, X. Y. (2014). Effects of Inorganic Fillers on the Flame- Retardant and Mechanical Properties of Rigid Polyurethane Foams. Journal of Applied Polymer Science, 131(10).

Czlonka, S., Kairyte, A., Miedzinska, K., & Strakowska, A. (2021). Casein/ Apricot Filler in the Production of Flame-Retardant Polyurethane Composites. Materials, 14(13).

Czlonka, S., Sienkiewicz, N., Strakowska, A., & Strzelec, K. (2018). Keratin feathers as a filler for rigid polyurethane foams on the basis of soybean oil polyol. Polymer Testing, 72, 32-45.

Czlonka, S., Strakowska, A., & Kairyte, A. (2020). Effect of walnut shells and silanized walnut shells on the mechanical and thermal properties of rigid polyurethane foams. Polymer Testing, 87.

Feldman, D. (2010). Polymeric foam materials for insulation in buildings. Materials for Energy Efficiency and Thermal Comfort in Buildings(14), 257-273.

Gu, X. H., Lyu, S., Cheng, W. D., & Liu, S. W. (2021). Effect of different catalysts on recovery and reuse of waste polyurethane rigid foam. Materials Research Express, 8(3).

He, X. M., Wang, L., Pu, W. H., Ren, J. G., Wu, W., Jiang, C. Y., & Wan, C. R. (2008). Thermal Analysis of Sulfurization of Polyacrylonitrile with Elemental Sulfur. Journal of Thermal Analysis and Calorimetry, 94(1), 151-155.

Helanto, K., Matikainen, L., Talja, R., & Rojas, O. J. (2019). Bio-based Polymers for Sustainable Packaging and Biobarriers: A Critical Review. Bioresources, 14(2), 4902-4951.

Ikegaya, H., Iwase, H., Hatanaka, K., Sakurada, K., Yoshida, K., & Takatori, T. (2001). Diagnosis of cyanide intoxication by measurement of cytochrome c oxidase activity. Toxicology Letters, 119(2), 117-123.

Iqbal, N., Mubashar, A., Ahmed, S., Arif, N., & Din, E. U. (2022). Investigating relative density effects on quasi-static response of high-density Rigid Polyurethane Foam (RPUF). Materials Today Communications, 31.

Jabber, L. J. Y., Grumo, J. C., Alguno, A. C., Lubguban, A. A., & Capangpangan, R. Y. (2021). Influence of cellulose fibers extracted from pineapple (Ananas comosus) leaf to the mechanical properties of rigid polyurethane foam. Materials Today-Proceedings, 46, 1735-1739.

Jalilian, M., Yeganeh, H., & Haghighi, M. N. (2008). Synthesis and properties of polyurethane networks derived from new soybean oil-based polyol and a bulky blocked polyisocyanate. Polymer International, 57(12), 1385-1394.

Kairyte, A., Vaitkus, S., Kremensas, A., Pundiene, I., Czlonka, S., & Strzelec, K. (2019). Moisture-mechanical performance improvement of thermal insulating polyurethane using paper production waste particles grafted with different coupling agents. Construction and Building Materials, 208, 525-534.

Kerche, E. F., Bock, D. N., Delucis, R. D., Magalhaes, W. L. E., & Amico, S. C. (2021). Micro fibrillated cellulose reinforced bio-based rigid high-density polyurethane foams. Cellulose, 28(7), 4313-4326.

Kerche, E. F., Delucis, R. D., Petzhold, C. L., & Amico, S. C. (2021). Rigid bio-based wood/polyurethane foam composites expanded under confinement. Journal of Cellular Plastics, 57(5), 757-768.

Khaleel, M., Soykan, U., & Cetin, S. (2021). Influences of turkey feather fiber loading on significant characteristics of rigid polyurethane foam: Thermal degradation, heat insulation, acoustic performance, air permeability and cellular structure. Construction and Building Materials, 308.

Khemani, K. C. (1997). Polymeric foams: An overview. Polymeric Foams, 669, 1-7.

Kuranska, M., & Prociak, A. (2012). Porous polyurethane composites with natural fibres. Composites Science and Technology, 72(2), 299-304.

Kuznia, M., Magiera, A., Zygmunt-Kowalska, B., Kaczorek-Chrobak, K., Pielichowska, K., Szatkowski, P., . . . Jerzak, W. (2021). Fly Ash as an Eco-Friendly Filler for Rigid Polyurethane Foams Modification. Materials, 14(21).

Lee, S. T., Park, C. B., & Ramesh, N. S. (2007). Polymeric Foams: Science and Technology. Polymeric Foams: Science and Technology, 1-220.

Leszczynska, M., Malewska, E., Ryszkowska, J., Kuranska, M., Gloc, M., Leszczynski, M. K., & Prociak, A. (2021). Vegetable Fillers and Rapeseed Oil-Based Polyol as Natural Raw Materials for the Production of Rigid Polyurethane Foams. Materials, 14(7).

Li, P., Tao, Y. B., & Shi, S. Q. (2014). Effect of Fiber Content and Temperature on the Dielectric Properties of Kenaf Fiber-filled Rigid Polyurethane Foam. Bioresources, 9(2), 2681-2688.

Liu, D. Y., Zhao, B., Wang, J. S., Liu, P. W., & Liu, Y. Q. (2018). Flame retardation and thermal stability of novel phosphoramide/expandable graphite in rigid polyurethane foam. Journal of Applied Polymer Science, 135(27).

Liu, Y., Qin, A. J., & Tang, B. Z. (2018). Polymerizations based on triple-bond building blocks. Progress in Polymer Science, 78, 92-138.

Mahmood, N., Yuan, Z. S., Schmidt, J., Tymchyshyn, M., & Xu, C. B. (2016). Hydrolytic liquefaction of hydrolysis lignin for the preparation of bio-based rigid polyurethane foam. Green Chemistry, 18(8), 2385-2398.

Mahmoud, A. A., Nasr, E. A., Zulfiqar, S., Sarwar, M. I., & Maamoun, A. A. (2021). Fabrication of castor oil-derived polyurethane mortar composites with energy saving and sound absorption characteristics. Journal of Polymer Research, 28(12).

Modesti, M., & Lorenzetti, A. (2003). Improvement on fire behaviour of water blown PIR-PUR foams: use of an halogen-free flame retardant. European Polymer Journal, 39(2), 263-268.

Mosiewicki, M. A., Dell'Arciprete, G. A., Aranguren, M. I., & Marcovich, N. E. (2009). Polyurethane Foams Obtained from Castor Oil-based Polyol and

Filled with Wood Flour. Journal of Composite Materials, 43(25), 3057-3072.

Njuguna, J. K., Muchiri, P., Mwema, F. M., Karuri, N. W., Herzog, M., & Dimitrov, K. (2021). Determination of thermo-mechanical properties of recycled polyurethane from glycolysis polyol. Scientific African, 12.

Oliwa, R., Ryszkowska, J., Oleksy, M., Auguscik-Krolikowska, M., Gzik, M., Barton, J., & Budzik, G. (2021). Effects of Various Types of Expandable Graphite and Blackcurrant Pomace on the Properties of Viscoelastic Polyurethane Foams. Materials, 14(7).

Pang, X. Y., Xin, Y. P., Shi, X. Z., & Xu, J. Z. (2019). Effect of different size-modified expandable graphite and ammonium polyphosphate on the flame retardancy, thermal stability, physical, and mechanical properties of rigid polyurethane foam. Polymer Engineering and Science, 59(7), 1381-1394.

Peng, H. K., Wang, X. X., Li, T. T., Lou, C. W., Wang, Y. T., & Lin, J. H. (2019). Mechanical properties, thermal stability, sound absorption, and flame retardancy of rigid PU foam composites containing a fire-retarding agent: Effect of magnesium hydroxide and aluminum hydroxide. Polymers for Advanced Technologies, 30(8), 2045-2055.

Pham, C. T., Nguyen, B. T., Phan, H. T. Q., Pham, L. H., Hoang, C. N., Nguyen, N. N., . . . Hoang, D. (2020). Highly efficient fire retardant behavior, thermal stability, and physicomechanical properties of rigid polyurethane foam based on recycled poly(ethylene terephthalate). Journal of Applied Polymer Science, 137(37).

Piantadosi, C. A. (2004). Carbon monoxide poisoning. Undersea and Hyperbaric Medicine, 31(1), 167-177.

Popescu, C., & Augustin, P. (1999). Effect of chlorination treatment on the thermogravimetric behaviour of wool fibres. Journal of Thermal Analysis and Calorimetry, 57(2), 509-515.

Qiu, Q. L., Yang, X., Zhang, P. H., Wang, D. Y., Lu, M., Wang, Z. Q., . . . Li, J. (2021). Effect of fiber surface treatment on the structure and properties of rigid bagasse fibers/polyurethane composite foams. Polymer Composites, 42(6), 2766-2773.

Rittel, D. (2005). Adiabatic shear failure of a syntactic polymeric foam. Materials Letters, 59(14-15), 1845-1848.

Son, M. H., Kim, Y., Jo, Y. H., & Kwon, M. (2021). Assessment of chemical asphyxia caused by toxic gases generated from rigid polyurethane foam (RPUF) fires. Forensic Science International, 328.

Soykan, U. (2022). Development of turkey feather fiber-filled thermoplastic polyurethane composites: Thermal, mechanical, water-uptake, and morphological characterizations. Journal of Composite Materials, 56(2), 339-355.

Srivastava, V., & Srivastava, R. (2014). On the polymeric foams: modeling and properties. Journal of Materials Science, 49(7), 2681-2692.

Strakowska, A., Czlonka, S., & Kairyte, A. (2020). Rigid Polyurethane Foams Reinforced with POSS-Impregnated Sugar Beet Pulp Filler. Materials, 13(23).

Tao, Y. B., Li, P., & Cai, L. P. (2016). Effect of Fiber Content on Sound Absorption, Thermal Conductivity, and Compression Strength of Straw Fiber-filled Rigid Polyurethane Foams. Bioresources, 11(2), 4159-4167.

Vaisanen, T., Das, O., & Tomppo, L. (2017). A review on new bio-based constituents for natural fiber-polymer composites. Journal of Cleaner Production, 149, 582-596.

Vitkauskiene, I., Makuska, R., Stirna, U., & Cabulis, U. (2011). Thermal Properties of Polyurethane-Polyisocyanurate Foams Based on Poly(ethylene terephthalate) Waste. Materials Science-Medziagotyra, 17(3), 249-253.

Wang, S. P., Chen, H. X., & Zhang, L. H. (2014). Thermal Decomposition Kinetics of Rigid Polyurethane Foam and Ignition Risk by a Hot Particle. Journal of Applied Polymer Science, 131(4).

Wolfe, H. W., & Reges, B. M. (1972). Urethane Foams - Flexible and Rigid. Rubber Age, 104(3), 64-&.

Xing, W. Y., Yuan, H. X., Zhang, P., Yang, H. Y., Song, L., & Hu, Y. (2013). Functionalized lignin for halogen-free flame retardant rigid polyurethane foam: preparation, thermal stability, fire performance and mechanical properties. Journal of Polymer Research, 20(9).

Xue, B. L., & Sun, R. C. (2015). Producing lignin-based polyols through microwave-assisted liquefaction for rigid polyurethane foam production. Abstracts of Papers of the American Chemical Society, 249.

Yakushin, V., Cabulis, U., Fridrihsone, V., Kravchenko, S., & Pauliks, R. (2021). Properties of polyurethane foam with fourth-generation blowing agent. E-Polymers, 21(1), 763-769.

Yu, Y. H., Choi, I., Nam, S., & Lee, D. G. (2014). Cryogenic characteristics of chopped glass fiber reinforced polyurethane foam. Composite Structures, 107, 476-481.

Yuan, J., & Shi, S. Q. (2009). Effect of the Addition of Wood Flours on the Properties of Rigid Polyurethane Foam. Journal of Applied Polymer Science, 113(5), 2902-2909.

Yurtseven, R., Tarakcilar, A. R., & Topcu, M. (2013). The Effects of Different Fly Ash Fillers on the Mechanical Properties, Thermal and Fire Behaviors of Rigid Polyurethane Foams. Journal of the Faculty of Engineering and Architecture of Gazi University, 28(4), 841-853.

Z, Bin, Yang, S. J., Liu, X. Y., Zou, Y., Kan, Y. C., Deng, D., . . . Tang, G. (2022). Rigid polyurethane foam composites based on bivalent metal phytate:

thermal stability, flame retardancy, and fire toxicity. Polymer-Plastics Technology and Materials.

Zhou, F., Zhang, T., Zou, B., Hu, W. Z., Wang, B. B., Zhan, J., . . . Hu, Y. (2020). Synthesis of a novel liquid phosphorus-containing flame retardant for flexible polyurethane foam: Combustion behaviors and thermal properties. Polymer Degradation and Stability, 171.

Zhou, W., Bo, C. Y., Jia, P. Y., Zhou, Y. H., & Zhang, M. (2019). Effects of Tung Oil-Based Polyols on the Thermal Stability, Flame Retardancy, and Mechanical Properties of Rigid Polyurethane Foam. Polymers, 11(1).

CHAPTER 2

X-RAY OBSERVATIONS OF THE CRAB NEBULA

E. NİHAL ERCAN[1]

1 Prof. Dr., Boğaziçi University, Physics Departme

Introduction

The famous Crab Nebula goes by many names; M1, NGC 1952, or Taurus A. It is discovered to be a supernova remnant and pulsar wind nebula in the constellation of Taurus on the Perseus Arm of the Milky Way galaxy, about 6500 light-years from Earth. The Crab Nebula is the most luminous and stable source of gamma-rays but emits energies in the range of the entire electromagnetic spectrum. The Crab Pulsar (NP 0532) is a neutron star discovered to be the nebula's heart that produces the energy that makes the Crab Nebula shine in radio, visible, x-ray, and gamma-ray wavelengths.

The term pulsar wind nebula can be explained as follows: electrons and positrons ejected from the pulsar at the heart of the nebula encounter interstellar mediums, which induce a shock. Outside of the shock, high-energy particles produce synchrotron radiation. The pulsar wind nebulae lack the defining shell of supernova remnants, and they are powered by the rotational energy loss of a neutron star resulting from a core-collapse supernova explosion.

The Crab Nebula's brightness, stability, the clock-like punctual heart of a neutron star, and wide range of emission spectrum made it a perfect calibration source for the x-ray astronomer since 2000 after many precise data were accumulated from many observations.

Observational History

When Chinese astronomers first spotted the Crab Nebula in July 1054, the exploding supernova was observable to the naked eye in daylight for 23 days and almost two years in the night sky. It is the first astronomical object discovered to be an aftermath of a supernova explosion. Although, the first identification of the nebula was not until 1731, by John Bevis. It was rediscovered and listed as the first of the "Messier objects" by Charles Messier. Hence the name M1 was given in 1758. In 1928, Edwin Hubble was the first to connect the explosion event of 1054 to the nebula, and Nicholas Mayall proved it. This event drove astronomers to discover other supernovae remnants observed as star explosions in history.

The name "Crab Nebula" was given by the 3rd Earl of Rosse, William Parsons, as he observed the nebula numerous times and concluded its image at the time resembled a crab. Even though the nebula has an ever-changing appearance, the name has stuck for centuries. In 1913, John Charles Duncan discovered that the object was expanding.

Gratton and Wilson (1972) developed the first analytic models to understand the structure of the Crab Nebula. Even though the nebula's size and spectral shape were well explained in the model, they assumed the

particles produced by the pulsar in the middle were ejected by diffusion, with loss of energy through synchrotron radiation and overlooked the effects of the magnetic field that is present. Kennel and Coroniti (1984) improved the model of the object with a toroidal magnetic field that links the pulsar to the nebula. However, the observations were not matching outside the x-ray region. (Madsen et al., 2015)

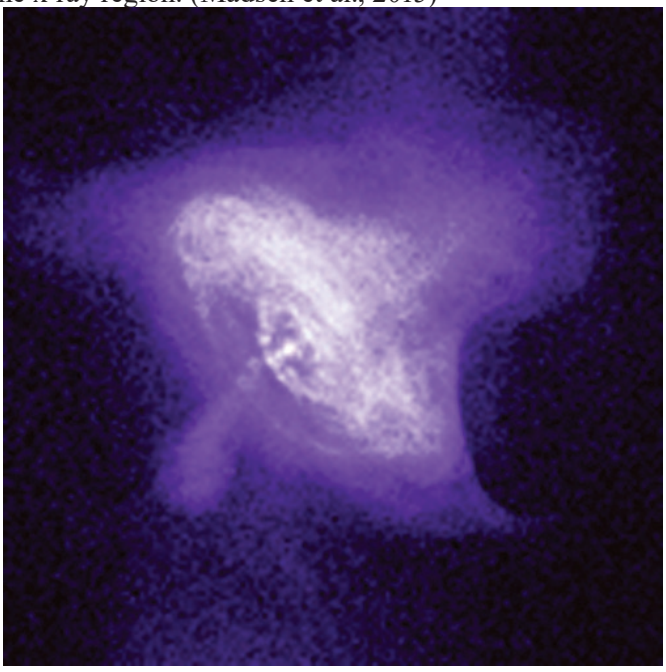

Figure 1 - The first Chandra image from August 29, 1999 /Credit: NASA

In 1985, using the Einstein Observatory High-Resolution Imager (HRI), researchers were able to examine the energy injection mechanism and the emission process of the Crab Nebula for the first time, as the new data from the Exosat satellite were still being processed. The conclusion was that the emission mechanism was far more complex than they had predicted that there must be a particle re-acceleration process. (Brinkmann et al. 1985)

Chandra has repeatedly observed the Crab Nebula since its launch in 1999. One of its primer observations was the bright ring of the Crab Nebula's high-energy particles that were never seen before. About two dozen knots that keep changing and emitting particles in the ring were their following observation in 2002 with the aid of the Hubble Telescope. The particles emitted from the central pulsar ran into the surrounding gas and created these knots. (Seward et al. 2006)

Mori et al. (2004) derived the spatial variations of x-rays from the torus and the jet in terms of the photon index. They hypothesized that the outer boundary of the torus acts like a "synchrotron burn off boundary", but the torus is not simply a result of the synchrotron loss becoming insignificant. The photon index at the core is similar to that of the torus, which translates to the electron spectra resembling the two directions of particle injection, jet and torus. It means the acceleration of the particles is the same in both radial and axial directions. They have also concluded that matter ejected from the supernova covering the pulsar wind nebula acts like an optical filament that absorbs some of the soft x-ray emission.

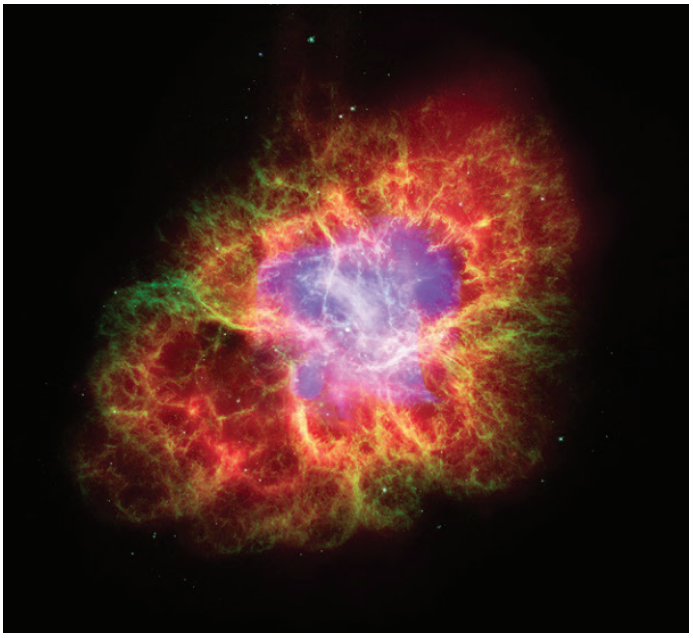

Figure 2 - *The first composite Chandra in light blue for x-ray, Hubble in green and dark blue for visible, and Spitzer in red for infrared. Credit: NASA*

NASA's "Great Observatory" program was completed when the Spitzer Space Telescope was launched in 2003. In 2006, they released the first composite of the Crab Nebula, as shown in *figure 2*.

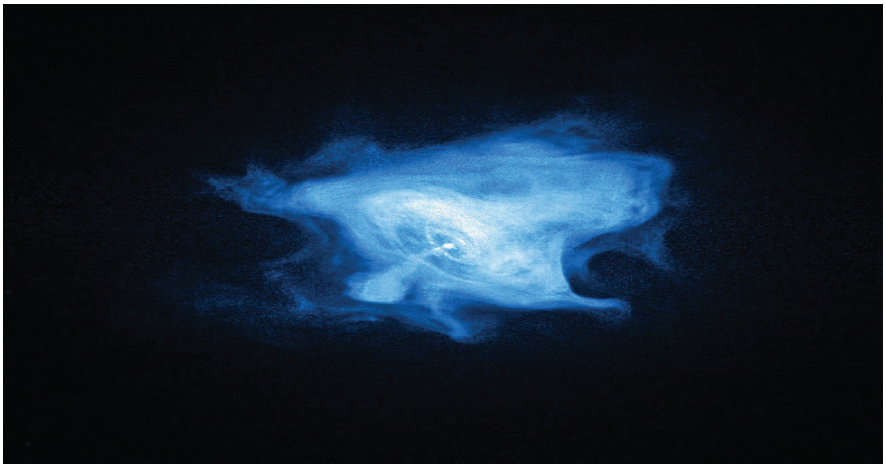

Figure 3 – The First clear view of the Crab Nebula from the Chandra Credit: NASA

Figure 4 - The x-ray image from Chandra is blue, the Hubble Space Telescope optical image is red and yellow, and the Spitzer Space Telescope's infrared observation is purple. Credit: NASA

Figure 3 consists of the first clear view of the boundary of the Crab Nebula's x-ray emitting pulsar wind nebula with the rapidly rotating, highly magnetized neutron star as the white dot near the middle. The pulsar creates an ejection of matter and antimatter from the poles and the equatorial direction of the pulsar due to its rotating nature and magnetic

field that results in a strong electromagnetic field. The inner x-ray ring is considered a shock wave. The electromagnetic field and less energized material scattered around the nebula control the outer particles and their motion, creating what astronomers call “fingers, loops, and bays”.

In 2011, Nasa’s Chandra recorded the data from the Crab Nebula for months to create a movie that shows the expansion of a ring and changes in x-ray emission around the Crab Pulsar near the middle of the nebula and the gamma-ray flares.

On January 5, 2020, researchers from NASA’s Universe of Learning program combined all of the data from NASA’s Great Observatory program with every part of the electromagnetic spectrum to visualize how the Crab Nebula looks in a three-dimensional representation.

Figure 5 - This image combined in 2017 consists of the observations from five different telescopes that observed five different types of radiation in the electromagnetic spectrum. The Karl G. Jansky Very Large Array (VLA) for radio in red, Spitzer Space telescope for infrared in yellow, Hubble Space telescope’s optical image in green, MXM- Newton for ultraviolet in blue, Chandra for x-ray in purple are all shown. Credit: NASA

Conclusion

The Crab Nebula has been an astronomical icon for many of its properties. Its discovery and further observation have contributed to astronomy and physics in ways no one could predict. Even after its prime

time -in terms of its properties being discovered one after another- the Crab Nebula still serves a great purpose to the astrophysics society even more as a reference point. Its ever-changing nature countered with its stable and astronomical properties creates a perfect balance worth observing.

I want to thank Begüm Yıldırım, one of the undergraduate students, for her help in combining the references in this study.

REFERENCES

Aharonian, Hitomi Collaboration, et al. "Search for Thermal X-Ray Features from the Crab Nebula with the Hitomi Soft X-ray Spectrometer*." *Publications of the Astronomical Society of Japan*, vol. 70, no. 2, 2018, https://doi.org/10.1093/pasj/psx072.

Brinkmann, W., et al. "X-Ray Morphology of the Crab Nebula." *Nature*, vol. 313, no. 6004, 1985, pp. 662–664., https://doi.org/10.1038/313662a0.

"Crab Nebula." *Chandra X-ray Observatory - NASA's Flagship X-Ray Telescope*, 2020, https://chandra.harvard.edu/photo/2020/crab3d/.

Kouzu, Tomomi, et al. "Spectral Variation of Hard X-Ray Emission from the Crab Nebula with the Suzaku Hard X-Ray Detector." *Publications of the Astronomical Society of Japan*, vol. 65, no. 4, 2013, p. 74., https://doi.org/10.1093/pasj/65.4.74.

Madsen, Kristin K., et al. "Broadband X-Ray Imaging and Spectroscopy of the Crab Nebula and Pulsar with *NuStar*." *The Astrophysical Journal*, vol. 801, no. 1, 2015, p. 66., https://doi.org/10.1088/0004-637x/801/1/66.

Seward, F. D., et al. "Faint X-ray Structure in the Crab Pulsar Wind Nebula." *The Astrophysical Journal*, vol. 652, no. 2, 2006, pp. 1277–1287., https://doi.org/10.1086/508532.

Weisskopf, Martin C., et al. "Discovery of Spatial and Spectral Structure in the X-Ray Emission from the Crab Nebula." *The Astrophysical Journal*, vol. 536, no. 2, 2000, https://doi.org/10.1086/312733.

Willingale, R., et al. "New Light on the X-Ray Spectrum of the Crab Nebula." *Astronomy & Astrophysics*, vol. 365, no. 1, 2001, https://doi.org/10.1051/0004-6361:20000114.

"Photo Album:: Crab Nebula:: May 11, 2011." *Chandra*, 2011, https://chandra.harvard.edu/photo/2011/crab/.

Images

"Photo Album :: Crab Nebula :: 28 Sep 99." *Chandra*, 1999, https://chandra.harvard.edu/photo/1999/0052/.

"Photo Album:: Crab Nebula:: October 24 06." *Chandra*, 2006, https://chandra.harvard.edu/photo/2006/crab.

"Photo Album:: Crab Nebula:: November 5, 2008." *Chandra*, 2008, https://www.chandra.harvard.edu/photo/2008/crab/.

X-ray: NASA/CXC/SAO/F.Seward; Optical: NASA/ESA/ASU/J.Hester & A.Loll; Infrared: NASA/JPL-Caltech/Univ. Minn./R.Gehrz F.Seward et al 2006, ApJ, 652, 1277 "Photo Album :: Crab Nebula :: November 23, 2009." *Chandra*, 2009, https://chandra.harvard.edu/photo/2009/crab.

G., Dubner. "Crab Nebula." *Chandra X-ray Observatory - NASA's Flagship X-Ray Telescope*, 2017, https://chandra.harvard.edu/photo/2017/crab/.

CHAPTER 3

X-RAYS FROM JUPITER

E.Nihal Ercan[1]

1 Prof.Dr., Boğaziçi University, Physics Department

What are X-rays?

There are various types of electromagnetic radiation. Only a small portion of that spectrum is visible to the human eye which we call visible or optical light. One type of electromagnetic waves that is not seen by us was discovered by a physicist Wilhelm Roentgen in 1895 called X-rays. [1] Since very little was known about this radiation, it is called X-Ray radiation.

X-Rays are generated from various sources in the cosmos. It is related to an object's physical properties such as its temperature because it determines the wavelength of radiation it emits. For one object to emit X-Rays, very high temperatures such as millions of Celsius degrees is needed.[1] Such temperatures may only be reached when there is vast gravity, for example black holes, neutron stars, white dwarfs and high magnetic fields.

In our solar system, there are many X-ray sources including our Sun which is one of the well-known X-ray sources since its outer atmosphere, which is called Corona, is very hot and suitable to emit X-rays. Even though planets, satellites and comets [2] do not have as high temperature as the Sun's surface, they are also X-ray sources which emit X radiation in various ways. One of the X-ray sources in our solar system is the planet Jupiter. This study will focus on these specific aspects in terms of how X-rays are produced in the Jupiter, how and through which satellites we may observe X-rays and what are some properties of these satellites, theories on X-rays coming from Jupiter and its compatibility with observations, properties of Jupiter that is deduced by observed X-rays, recent research and possible future works on X-rays coming from Jupiter.

Planet Jupiter and Its Properties

Before getting into X-rays coming from Jupiter, we may talk about Jupiter as a planet of our solar system and its properties.

With its 318 Earth mass, which is about 1.9x10^27 kg, Jupiter is the most massive planet in our solar system. It is more than twice as massive as the rest of the planets in the solar system added up. Continuing numerical properties, according to NASA, a year on Jupiter contains 4331 Earth days.[3] By its -110 degree mean temperature which is the average surface temperature of the planet, and due to its deep atmosphere, unknown surface pressure makes Jupiter unlikely for potential life. However, one of Jupiter's moons, Europa is one of the likeliest places to find life in our solar system according to NASA Scientists.[4]

X-rays and Its Properties

As briefly mentioned in the introduction paragraph, X-rays are electromagnetic waves which means that they are just another form of light.

To determine what form of light is, one checks the energy of it. X-rays are highly energetic waves and can break up the molecules. In other words, X-rays in the 2-20 keV (kilo-electron volt) range are readily absorbed by the materials.

X-ray emissions that are detected, counted, and analyzed in our world may be seen from various astronomical objects.[5] Brighter sources are usually referred to a Galactic which are often lie in Milky Way, however the fainter and more uniformly distributed sources are usually called extragalactic according to Cosmic X-ray Astronomy book by J. Adams.

X-ray Emission Types

X-ray output from astronomical objects may be explained by two emission mechanisms called thermal and non-thermal. Thermal emissions are emitted from very hot bodies whose temperature is a million degrees of Kelvin. (Cosmic X-ray Astronomy-Adams) It can be observed in two main types. First one of thermal emission is called black body radiation and the second one is called the Bremsstrahlung. Before getting into detail of those two thermal emission types, we may briefly talk about non-thermal emissions. As the name implies, non-thermal emissions do not require millions of degrees temperatures, in other words they are temperature independent events. Synchrotron radiation, comptonization and reverse Compton scattering are involved in non-thermal emission type.

In thermal emission type, (Cosmic X ray Astronomy, Adams) blackbody and Bremsstrahlung emission differs by whether an object is optically thick or thin. In an optically thin case, which also may be understood as a geometrically thick object, blackbody emission is observed. Bremsstrahlung emission occurs when an electron slows down, because due to conversion of energy a photon is emitted in the X-ray form. For non-thermal radiation type, we mentioned synchrotron radiation which happens when accelerating charged particles in magnetic field.[5]

X-ray Observational Characteristics of Jupiter

X-rays are being detected from exotic sources such as pulsars far away, neutron stars, or black holes as mentioned in the previous paragraph. However, there are many X-ray sources right here in our solar system. One of these sources is Jupiter. First X-ray spotted from Jupiter was by NASA's Einstein X-ray Satellite in 1979 [6]. After this first detection, throughout the years, X-ray detections from Jupiter had kept going with various satellites such as Rosat and Chandra. Detected X-rays were understood mostly coming from Jupiter's northern hemisphere, but it was not very clear enough to detect exactly where. According to NASA Scientists, these were due to powerful auroras. It is also identified in research done in 2016

that X-ray emissions from Jupiter are from hot spots at each pole as North and South. [7]

One important difference between Earth's and Jupiter's auroras is the source of charged particles.[7] For Jupiter, raining electrons and ions come from volcanoes. In this matter, Gladstone says seeing sulfur and oxygen spectral lines from volcanic elements will mean that Jupiter satellite Io is involved.[7]

With the data coming from one of the most famous X-ray Satellites Chandra revealed that this is indeed true. According to it, X-rays came from Jupiter was from its hot spot located very close to Jupiter's north magnetic pole and it showed also that it pulsed.[7]

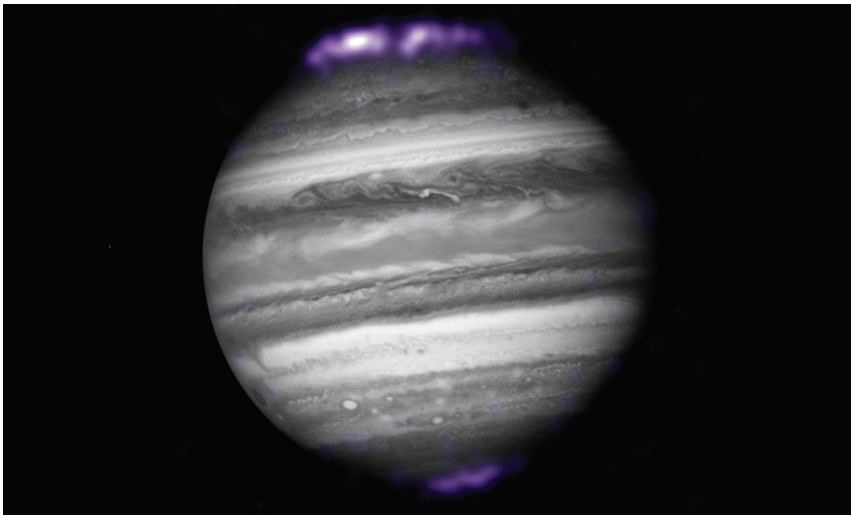

Figure1: The purple hues in this image show X-ray emissions from Jupiter's auroras, detected by NASA's Chandra Space Telescope in 2007. They are overlaid on an image of Jupiter taken by NASA's Hubble Space Telescope. Jupiter is the only gas giant planet where scientists have detected X-ray auroras. [1]

Another data from Chandra talks about hot spot pulsing 15 times during one Jupiter day which is 10-hour rotation according to 1 Earth hour. Due to basic calculation of dividing 10 hours to 15 tells that approximately every 45 minutes, an X-ray source blinks.[7]

The reason behind X-rays coming from Jupiter is something that researchers were curious about for many years. One theory on X-ray auroras being caused by interactions at the boundary between Jupiter's magnetic field and the solar wind which is particles coming from Sun moving as in the motion of high-speed flow.[7]

There were various explanations on X-ray production mechanisms on Jupiter. One was assuming neutral sulfur molecules that were ionized by solar UV light. It was not clear with spatial resolutions whether emission is from large radial distances or the magnetosphere of the planet, which is the surrounding space in which the magnetic field affects charged particles. However, it was understood after Chandra and XMM-Newton observations.

To simply explain the mechanism of this interaction between the magnetic field of Jupiter and solar wind, we may say that the magnetic field is vibrated due to this interaction, and it causes magnetic waves. And according to NASA Scientists [7], via Chandra and XMM-Newton, bright flashes of X-rays are observed due to collisions.

Just as mentioned on the above as 15 minutes, with recent studies it is given as 11 minutes, it represents the time interval to travel along magnetic field lines of Jupiter.[7]

Charge Exchange

We may get into the Charge Exchange mechanism more, to understand X-rays aurora of Jupiter. Solar winds are the charged particles, continuously flowing, from the Sun to the Solar System. At the end of 1990's, charge transfer was understood as solar wind heavy ions which are any ion heavier than Helium in Astrophysics. The exchange process may be simply explained as ions interacting with neutral particles. After the interaction, if relaxation of the ion occurs, photons may be emitted which is an important emission process throughout the universe.

As just given the definition, if this process happens due to solar winds, it is called Solar Wind Charge Exchange or in short SWCX. [15] As stated in the same paper, this charge exchange emissivity is said to be proportional with the densities of neutral atoms and solar wind and solar wind's velocity.

According to Branduardi's paper on X-ray from solar objects, 2016, solar winds play an important role in the soft X-ray aurora of Jupiter.

Briefly mentioning the kinds of X-ray light coming from Jupiter, it can be said that they are classified into two types by some scientists, which are soft and hard X-rays. These two types differ by the energy of the emitted X-ray. As the name suggests, soft X-rays have smaller energy than hard X-ray types. [12]

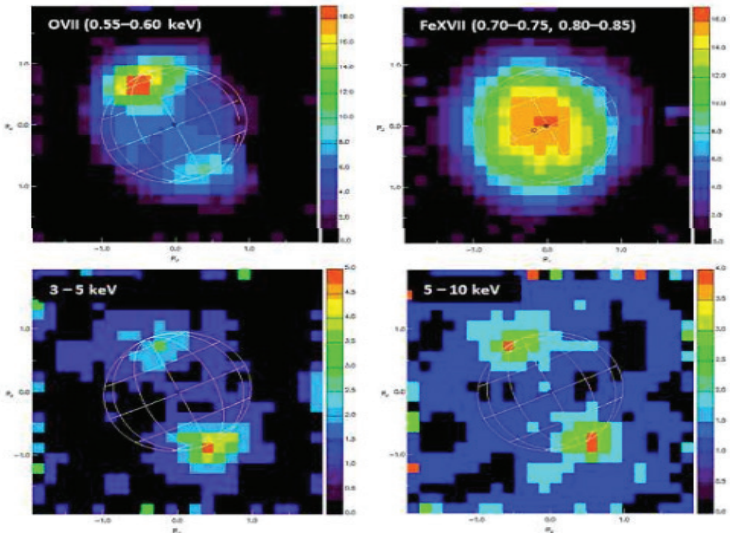

Figure 3: XMM-Newton Spectral Maps of Jupiter's aurorae,

Below two figures shows X-rays emission at energies higher than 3 keV (kilo-electron volt) [3]

From the XMM-Newton data (Branduardi-Raymont et al. 2007), spectral maps of Jupiter's aurora may be seen in the figure 3. Colour scale bar is in units of EPIC counts. [10] Auroral emission, which is mentioned as seen from poles of Jupiter, is also observed as hard X-rays which are higher energies. It is analyzed as bremsstrahlung emission due to its featureless continuum shape (Branduardi, 2016), as seen from figure 3.

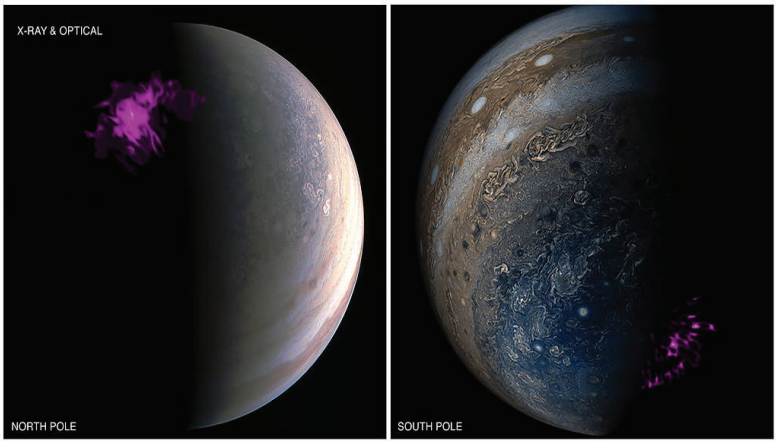

Figure 4: X-ray Auroras from Poles of Jupiter [4]

It was a mystery where the energy comes from to make X-rays because Jupiter has the most powerful aurora. It was being expected that data coming from Chandra, XMM-Newton and Juno may help answering this question according to NASA scientists.[7]

To understand the mechanism to derive Jupiter's luminous X-rays was an ongoing research subject. After forty years of research, scientists have announced that it is now understood with the data coming from Juno. These questions are answered with the phenomenon called EMIC waves which are known to exist due to interactions between a planet's magnetosphere and its plasma sphere.[8] Particles follow along those magnetic field lines and those ions are called to surf those EMIC Waves and as they crash into atmosphere, they are said to form auroras.

"What we see in the Juno data is this beautiful chain of events. We see the compression happen, we see the EMIC wave triggered, we see the ions, and then we see a pulse of ions traveling along the field line," said William Dunn of the Mullard Space Science Laboratory, University College London, and a co-author of the paper. "Then, a few minutes later, XMM sees a burst of X-rays."[9]

Theoretical Aspect of X-rays from Jupiter

In the paper "A Study of Jupiter's Aurorae with XMM-Newton" of G. Branduardi-Raymont and her colleagues, high energy continuum component of X-ray emission that has energy of above 2 kilo-electron volt is mentioned as Jupiter's EMIC Spectra. As following the description on spectral shape of high energy component, it is told that bremsstrahlung model approximates the best when the flux is low.[10] This thermal emission type, mentioned above, was expected to be responsible of UV Aurora Oval according to the same study.

One of Jupiter's moons, Io is also guessed as the cause of Jupiter's observed X-rays. Gasses produced in Io's Volcanoes is trapped in Jupiter's orbit and in there, they reach high speeds and are accounted for observed X-rays of Jupiter.[11]

X-ray Observations: X-ray Telescopes

From our daily lives, we are familiar with the fact that visible light reflects through mirrors. However, X-rays do not reflect off in the same manner due to their high energy, they go through the mirror. Therefore, X-ray telescopes are very different than optical telescopes. For example, hyperbolic mirrors are used in X-ray telescopes. Throughout the years, various countries have sent various X-ray Satellites including X-ray telescopes such as Uhuru, Rosat and as mentioned in this paper a couple of times XMM-Newton and Chandra. XMM and Chandra were both sent

to space in 1999. Even though Chandra was mainly designed to study supermassive black holes and center of galaxies [13] and XMM for spectra of supernova remnants, accretion disks around black holes, stars and other types of sources [13], they are both very important to study X-rays coming from Jupiter.

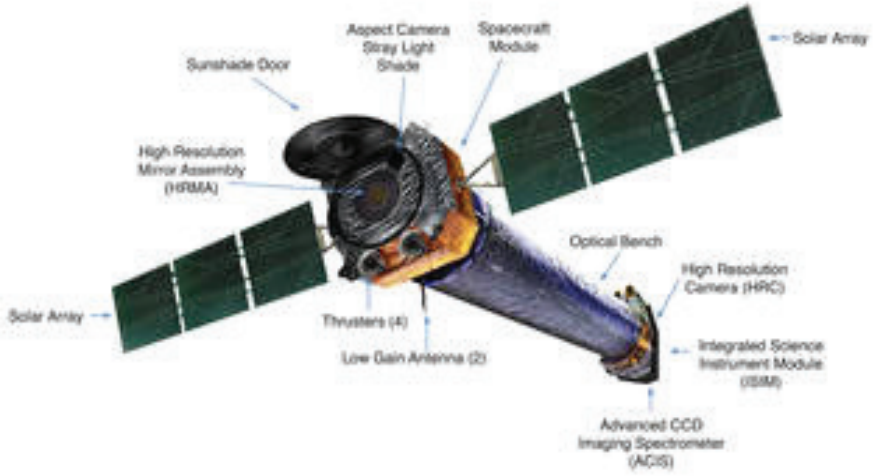

Figure 2: Chandra Telescope System [2]

Conclusions : Even though, for many years scientists are observing, analyzing, and understanding X-rays, there are so many properties that we lack mechanisms that are not explained. For the biggest planet in our solar system, despite the fact that it is approximately 850 million kilometers away [14], it is pretty close to Earth if we consider the whole universe. However, in 21th century, which is the time that humans think they can understand and solve everything with mind, unsolved mysteries of X-rays coming from Jupiter so to speak taunts this mistaken understanding. According to astrophysicists, new data that hopefully will come from satellites such as Chandra or XMM-Newton is going to be very helpful to learn more on X-rays.

I would like to thank Betül Baysal for her help in preparing this manuscript.

REFERENCES

[1] https://chandra.harvard.edu/xray_astro/xrays.html

[2] https://chandra.harvard.edu/xray_sources/solar_system.html

[3] https://nssdc.gsfc.nasa.gov/planetary/factsheet/

[4] https://solarsystem.nasa.gov/planets/jupiter/in-depth/#otp_rings

[5] X-ışınları ve Evren, Nihal Ercan

[6] https://science.nasa.gov/science-news/science-at-nasa/2002/07mar_jupiterpuzzle

[7] https://www.nasa.gov/mission_pages/chandra/images/the-dynamic-duo-jupiters-independently-pulsating-x-ray-auroras.html

[8] https://www.vice.com/en/article/y3d577/jupiter-pulses-with-energy-like-clockwork-and-now-we-finally-know-why

[9] https://www.nasa.gov/feature/jpl/40-year-mystery-solved-source-of-jupiter-s-x-ray-flares-uncovered

[10] Branduardi-Raymont et al., 2007 https://www.aanda.org/articles/aa/pdf/2007/08/aa6406-06.pdf

[11] https://chandra.harvard.edu/xray_sources/solar_system.html

[12] Bhardwaj et al., 2007, https://fr.art1lib.org/book/3889375/a1d683

[13] https://chandra.harvard.edu/chronicle/0202/40years/index.html

[14] https://www.space.com/18383-how-far-away-is-jupiter.html#:~:text=How%20far%20is%20Jupiter%20from,miles%20(588%20million%20kilometers).

[15] G. Branduardi-Raymont, X-ray studies of solar system objects: past, present and the next decade, 2016

https://discovery.ucl.ac.uk/id/eprint/1569540/1/Branduardi%20Raymont_X-ray%20studies%20of%20solar%20system%20objects%20Past%20present%20and%20the%20next%20decade_2.pdf

FIGURES

[1] https://www.nasa.gov/feature/jpl/40-year-mystery-solved-source-of-jupiter-s-x-ray-flares-uncovered

[2] https://www.nasa.gov/mission_pages/chandra/spacecraft/index.html

[3] Branduardi-Raymont et al., 2007 https://www.aanda.org/articles/aa/pdf/2007/08/aa6406-06.pdf

[4] https://www.nasa.gov/mission_pages/chandra/images/the-dynamic-duo-jupiters-independently-pulsating-x-ray-auroras.html

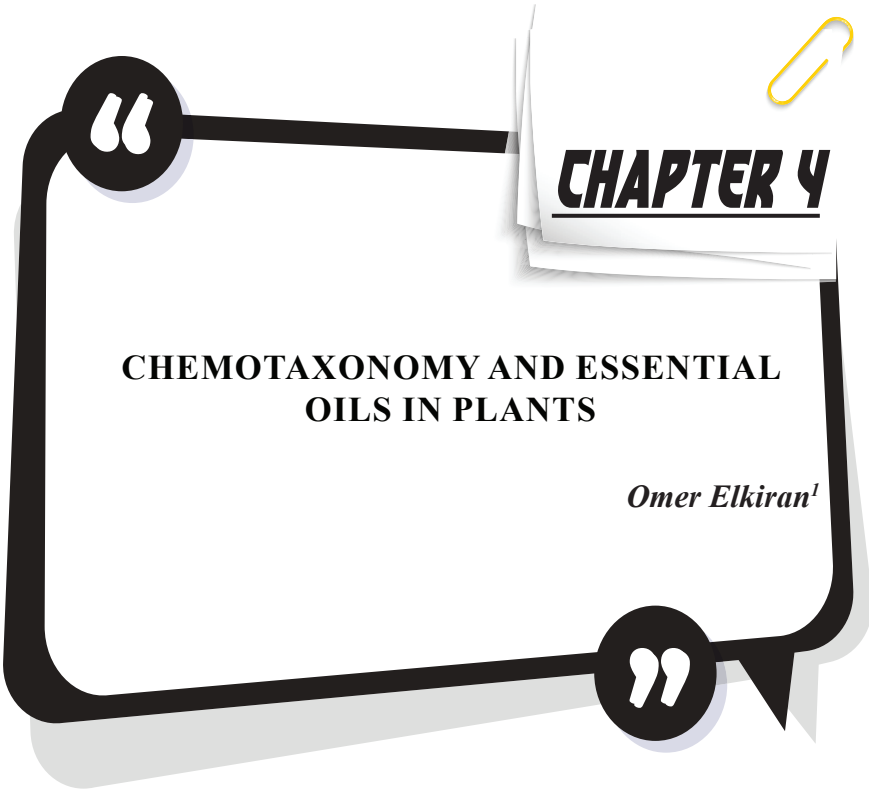

CHAPTER 4

CHEMOTAXONOMY AND ESSENTIAL OILS IN PLANTS

Omer Elkiran[1]

1 Omer Elkiran, Ph.D. Assistant Professor, Vocational School of Health Services, Environmental Health Programme, Sinop University, Turkey, (ORCID: 0000-0003-1933-4003)

Living things on Earth are members of the environment in which we live together with humans. As it is already known, the environment consists of inanimate (water, air, soil, etc.) and living (animals and plants) elements. Living things make up the living (biotic) part of this composition. Although the number of species living in the world varies according to the authors, it is estimated to be 2.5-3 million in our time. Approximately 400-500.000 of these are plants and the rest are animals.

It is easy to distinguish higher organisms like plants and animals; however, it is very difficult for some primitive organisms (especially single-celled organisms) to be separated from each other in this way. For this reason, living things that were previously divided into two main groups as plants and animals, with some difficulty, are now divided into different groups in recent years.

Scientists have started to examine and classify them by putting together similar ones because there are many species of living things, and thus the science called Taxonomy-Systematics emerged (Avesis, 2022).

Taxonomy is the branch of science facilitating the study of living things by dividing them into groups according to their similarities or differences. Taxonomy examines this distribution on the earth and their short habitat characteristics by naming these creatures in line with systematic rules.

The duties of taxonomy can be summarized as follows;

1) To examine each taxon or species and to determine their unique characteristics,

2) To find out which of these characteristics are common in certain taxa, and from which biological reasons the differences and common characteristics emerge,

3) Reaching variations within the taxa,

4) To perform basic tasks such as examining and grouping plants into small and large groups, taking into account their natural affinity with each other and based on their phylogenetic development (Digrak and Ilçim, 2002; Uma, 2010).

The science of taxonomy undertakes the identification and expression of living things. “Classification” is different from taxonomy. It is possible to summarize the study subject of classification only by grouping living things and grading them. Classification is the ordering of living or extinct organisms into groups.

Systematics, on the other hand, can be defined as the branch of science examining the evolutionary kinship relations, similarities, and differences of living things, different from taxonomy and classification in a much more

comprehensive manner. In other words, it relates systematic, taxonomy groups to each other. Nomenclature is the sub-branch of systematics and deals with naming living things according to certain rules (Tübitak, 2008).

Different methods that are used in the classification of plants allow plants to be known better, to understand their characteristics, and uncover their potential for use. Living things were initially classified only based on their external appearances and technological conditions. Later, the taxonomic perspective was enriched with the developments in different fields of science. Chemotaxonomy, which contributes to the classification of living things, is a taxonomic method that emerged after the use of chemical groups in secondary metabolites in plants. As well as the morphological, anatomical, palynological, physiological, molecular and cytological classification used in plant taxonomy, chemotaxonomy is used in plants with secondary metabolites (Labra et al., 2004; Cruz et al., 2008; Bernath and Nemeth, 2007; Yurteri et al., 2021).

Secondary metabolites are chemicals produced by the plant whose roles in growth, photosynthesis, crop transformation, or other primary functions have not yet been uncovered (Anonymous 1).

More than 100.000 variants of secondary metabolites have been identified so far. In these varieties, the main classes of organic compounds are unique carbon skeletons, diversity of functional groups such as aliphatic, aromatic, hydroaromatic, and heterocyclic. It was reported in previous studies that complex compounds differ from organ to organ, and sometimes among plants and species, and can sometimes be used as taxonomic characters in plant classification (Wink, 2009; Alaca and Arslan, 2012).

Many plant secondary products can be recatabolized into primary metabolic materials. It was previously believed that all secondary products were inactive wastes and storage products accumulating unchanged throughout plant life. However, it was later realized that all secondary products could be transformed except polymers such as tannins, lignin, and rubber. According to recent studies, different secondary products can be reduced to primary metabolic products after some time, and in this way, C and N can be used as energy sources. Evidence of catabolization of secondary products was the subject of 2 types of studies. First, the amounts of many plant secondary products are seasonal or even daily. Second, when secondary products are labeled as radioactive, the radioactivity disappears after a few hours or a few days. For this reason, many secondary products, such as many primary metabolic products, play roles as primary metabolic in the plant (Unay, 2004; Alaca and Arslan, 2012).

Secondary metabolites were known by humans for thousands of years, and their hypothesized biological functions are discussed although

they are used in dyes (e.g. indigo, shikonin), spices (vanillin, capsaicin, mustard oil), fragrance (rose, lavender, and other essential oils), stimulants (caffeine, nicotine, ephedrine), and hallucinogens (morphine cocaine, scopolamine, tetrahydrocannabinol), insecticide (nicotine, piperine, phyrethrin, rotenone), vertebrate and human poisons (coniine, strchnine, acanitine, colchicine, cardiac glycosides) and therapeutic (atropine, quinine, cardenolide, codeine) (Alaca and Arslan, 2012).

The discovery of chemical components used in chemotaxonomy in plants and the detection of trace amounts of chemicals accelerated in parallel with the rapid developments in analytical techniques (Bhargava et al., 2013). Although the chemical composition is mainly under genetic control, the chemical profile remains essentially constant after several years in different environments. In such a case, it is considered to be a "chemotype" (Sadeghi et al., 2015). A chemotype is a chemically distinct structure in a plant differing in secondary metabolite composition. Small genetic and epigenetic changes with little or no effects on morphology or anatomy might cause large changes in chemical phenotype. Chemotypes are usually defined by the chemical most abundantly produced by the individual, and this concept was useful in studies by chemical ecologists and natural product chemists (Keefover-Ring et al., 2009; Yurteri et al., 2021). Various factors such as genetic variations, plant varieties, plant nutrition, fertilizers used, geographical location of plants, stress factors during growth or ripening, as well as post-harvest drying and storage might affect the amount and variety of plant chemicals (Raut and Karuppayil, 2014).

Although the potential value of plant secondary metabolites, which make up the content of chemotaxonomy, to taxonomy has been recognized for about 200 years, their practical applications have been limited to this century, mainly the last 45 years. The first comprehensive advocate of chemical taxonomy was McNair (1935), who examined the distribution of essential oils, fixed oils, and alkaloids in Angiospermae. Also, the first comparative analyzes were reported and most of these analyzes included essential oils of Myrtaceae, particularly Eucalyptus. Although these studies confirmed the chemical diversity of different taxa even at this early stage, they also demonstrated the possibility of interspecies variation in chemistry (Wink and Waterman, 1999).

Phenolics, alkaloids, terpenoids, and amino acids, which do not participate in the structure of proteins, are four important groups of compounds used widely for chemotaxonomic classification (Smith, 1976) and show a wide variety in chemical diversity, distribution, and function (Hegnauer, 1986). The chemotaxonomic classification system is based on the similarity of the chemical components of the taxon (Atal and Kapur, 1982; Rasool, 2010; Singh, 2016).

The important technical development allowing the establishment of chemotaxonomy was paper chromatography, which allowed multiple samples to be extracted and compared regarding the presence or absence of specific metabolites. Flavonoids and related phenolic compounds have proven particularly suitable for investigation, first by Paper Chromatography and later by Thin Layer Chromatography (TLC). It was the distribution of some common phenolics in Angiospermae that was first studied in more detail. Other methods developed in the 1970s and 1980s essential to the advancement of chemotaxonomy and phytochemistry were capillary column (or high-resolution) Gas-Liquid Chromatography (GLC), High-Performance Liquid Chromatography (HPLC), Mass Spectrometry (MS, especially GLC-MS, LC-MS), and Nuclear Magnetic Resonance (1H, 13C-NMR) (Yaprak, 2022).

Malvaceae, Ranunculaceae, Magnoliaceae, Polygonaceae, and Solanaceae families are used extensively in the chemotaxonomic field (Sivarajan, 1991; Singh, 2016).

Essential oils are oily mixtures usually colorless or light yellow in color, volatile, strong-smelling, and volatile oils, produced from parts of plants or plant sources such as roots, stems, leaves, fruits, barks, and flowers, liquid at room temperature, sometimes freeze, easily crystallize. These oils are called “essential oils” because they can evaporate even at room temperature when left in the open, “etheric oil” because they evaporate like ether, and “essential oil” because they are fragrant and used in the perfume industry. Since essential oils have a wide range of usage areas, their chemical structures were examined and their biological activities were a matter of curiosity (Yaylı, 2013; Aydın, 2019).

Although essential oils are called “oil” since they do not mix with water and accumulate as an oily layer on the water surface, there are important differences between fixed oils and essential oils. These:

· Although essential oils can be dragged by water vapor and do not leave a stain on the filter paper, fixed oils are not dragged by water vapor, but leave a permanent, oily stain when dripped onto the filter paper.

· Unlike essential oils, fixed oils are generally insoluble in aqueous alcohols.

· Fixed oils are compounds that have the form of esters formed by glycerol, which is trivalent alcohol, and fatty acids but essential oils are composed of a mixture of many compounds from different classes.

· Essential oils do not become bitter over time because they are not in a fatty acid-glycerol ester structure and they oxidize and become resinous over time in the face of light and air.

· As the name suggests, essential oils evaporate at room temperature while fixed oils are liquid or solid.

Essential oils contain terpenic or non-terpenic volatile compounds (Tanker and Tanker, 1990). They all consist of hydrocarbons and their oxygenated derivatives. Some may contain nitrogen or sulfur and may be available in the form of alcohol, acid, ester, epoxide, aldehyde, ketone, amine, sulfite, etc. Non-terpenic hydrocarbons are paraffin (alkanes and alkenes) derivatives that are derived from methane. Terpenes are formed by the bonding of isoprene units. Monoterpenes, sesquiterpenes, and even diterpenes are included in the composition of most essential oils. Phenylpropanoids, fatty acids, and esters and their degradation products can be present in essential oils (Baser, 2009).

Essential oils are mostly found in the glandular hairs or secretory pockets of the epidermis, in the essential oil cells of the inner tissues, and the large secretion pockets in the interior through the schizogen, lysigene, or schizolizigen route (Sakar and Tanker, 1991, Aydın, 2019). Essential oils not only make up the structure of the hormones in plant cells but also play roles in the transmission of information between cells and in the defense mechanisms of plants. They have shown themselves with medical and cosmetic applications as bactericidal, virucidal, fungicidal, antiparacidal, and insecticidal since the middle ages, and have been used extensively in pharmacology, food and cleaning industries, and aromatherapy in recent years (Baser, 2000; Çelik and Çelik, 2007; Bakkali et al., 2008; Erdoğan, 2012; Temel et al., 2018). Also, it has recently found use in animal production, poultry, and beekeeping (Baser, 2000; Temel et al., 2018).

Their functions in plants in general and their importance in plants will be more understandable with the following list:

- The fact that plants can reproduce by pollination, and that animals are attracted by essential oils in spreading fruits and seeds to the environment and distant areas show the main importance of these oils. The realization of these events depends on the secretion period of essential oils in plants and the way they accumulate in flowers, seeds, and fruits.
- Essential oils regulate very important events (e.g. balanced evaporation of water in plants, protection of plants from the stress of solar radiation, the adaptation of plants to sunlight during the day, and cooling at night). They also reduce the stress on the plant by balancing the movement of water.
- Essential oils play also important roles in the protection of the plants from diseases, pests, and animals, in the rapid healing of

wounds on the bark and woods, in the protection of the plant from microorganisms, and in strengthening the immune system.

- Essential oils give plants allelopathic characteristics with which plants slow down the development of other species in the environment where they grow and create a suitable environment for their development (Mammadov, 2014).

All applications of essential oils (i.e. industrial, commercial value, etc.) are judged directly based on their chemical composition, physicochemical characteristics, biological activities, and the most abundant or sometimes the least abundant chemical component. For example, if an essential oil sample is rich in monoterpenes or sesquiterpenes, it shows low solubility in the water-alcohol environment and for this reason, is not widely accepted in the perfume industry. On the other hand, although safrole is not suitable for use in food products with its known genetic and carcinogenic effects, essential oils rich in thymol or carvacrol are preferred for their antiseptic and antimicrobial characteristics (Mastelic' et al., 2008; Giray and Kırıcı, 2021).

The quality of essential oils may vary in amount and composition according to the age of the plant, the plant organ (morphogenetic variation), the development periods of the plant (ontogenetic variation), and even the harvest time (diurnal variation), as well as environmental factors such as climate, soil composition, geographical region, the soil moisture content in the growing season (Kırıcı and Inan, 2001; Giray et al., 2008; Kaya et al., 2012; Maral et al., 2018; Maral and Kırıcı, 2019; Çalışkan et al. 2019; Kırıcı and Giray, 2021). However, when previous studies were reviewed, it was seen that the main components of the same taxa taken from different geographies were generally common. The number of chemical components in the essential oil can also vary. Especially the proportions of the main components in the essential oils of some plants determine the medicinal and economic value of the oil. In the essential oil studies that were conducted previously with the laurel (*Laurus nobilis* L.) plant, which is common in Turkey, the amount of 1,8-cineole (eucalyptol) component, which is the main component of the essential oil content, was found to be lower in the samples taken from the Black Sea region, especially in the samples from the Mediterranean Region (Sangun et al., 2007; Karık et al., 2015; Elkiran et al., 2018; Elkiran and Karakaya, 2021). Similar results were reported in essential oil studies conducted with different plants in different parts of the world. However, these different results in biological activity studies showed that essential oil contents and amounts may vary depending on the geographical conditions of the plant. The amount and content of essential oils produced in plants also differ according to various plants. It does not occur at all or occurs in trace amounts in some plants,

and it is produced much more in others. The genetic characteristics of the plant also have effects on the potential of the plant to produce essential oil.

Turkey has a rich flora because of its location and shows the characteristics of different biogeographic regions. For this reason, there is a wide variety of plants containing essential oils. In other words, they have medicinal and aromatic characteristics. not every plant can be used in essential oil studies, different parts of the plants can be used, or the amount and content of volatile substances in different organs can be different. These parts are the leaves (eucalyptus, cedar, laurel), leafy branches (pine), aerial parts (thyme, mint, sage), dry buds (stick clove), bark (Ceylon cinnamon, Chinese cinnamon), wood (sandalwood, cedarwood, rosewood), roots (angelica, vetiver), rhizomes (ginger, violet root), corms (garlic, onion), fruits (aniseed, fennel, coriander, cumin, juniper), fruit peels (orange, lemon), seeds (cardamom, nutmeg), lichens (oak lichen, tree lichen), balsam (saxula oil, Peru balsam, myrrh), oleogumrezin (gum mastic), and oleoresin (terementi, opopanax). Essential oils can also be obtained from animal products such as moschus moschiferus and civet cat (Baser, 2009; Aydın, 2019) (Table 1).

Table 1. *Plant organs that contain essential oils (Handa, 2008)*

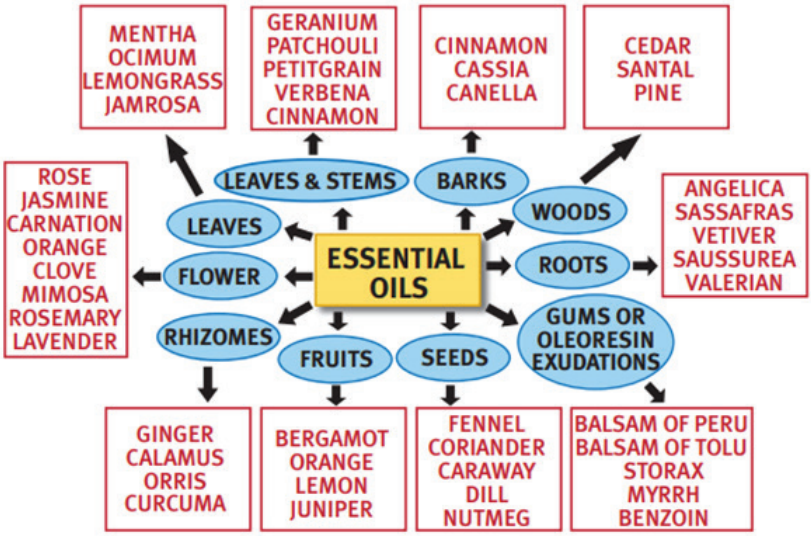

When the world flora is evaluated, approximately 1/3 of the plant families that make up the flora contain essential oil. Some of these families in the first place are; Apiaceae-Umbelliferae, Cupressaceae, Brassicaceae, Iridaceae, Myrtaceae, Rosacea, Lauraceae, Lamiaceae, Geraniaceae, Zingiberaceae, Compositeae, Pinaceae (Mammadov, 2014). It may differ

in the organs in which essential oil is produced (Table 2). A total of 30% of the species of the flora of Turkey are aromatic plants. Aromatic plants are the main sources of essential oils and approximately 65% are obtained from woody plants (trees or shrubs) (De Silva, 1995; Yollu, 2009).

Table 2. *Family-specific plant tissues are responsible for producing or storing essential oil (Handa, 2008)*

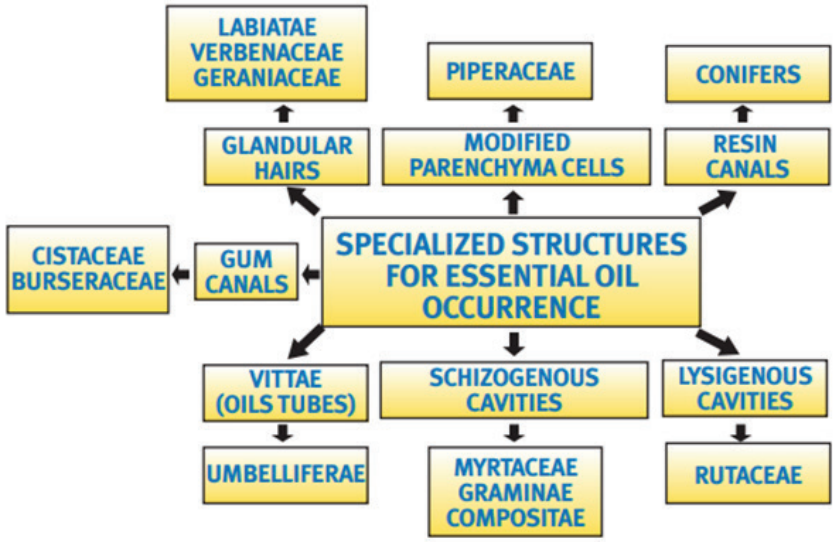

Essential oil extraction methods also affect the amount of oil to be obtained. Different methods can be used according to the type and amount of the plant, purpose of use, etc. in obtaining essential oil. Although it is obtained in smaller amounts for scientific studies, higher amounts of essential oil are obtained because of its economic importance. The methods of obtaining essential oil are as follows in general;

1. Distillation method: It is the separation method that performs with the difference in boiling points of liquids.

a) Distillation with water

b) Steam distillation (SD)

c) Vacuum distillation

2. Extraction method: In general, it is a method of extracting essential oil in a solvent.

a) Solvent extraction

b) Supercritical fluid extraction

c) Microwave extraction

d) Compressed solvent extraction

e) Solid-phase microextraction

f) Multidirectional extraction

3. Mechanical method: It is a method of obtaining the oil by placing the peels of lemons and oranges in a cloth bag and squeezing them under cold hydraulic presses (Yaylı, 2013; Aydın, 2019).

The increased use of essential oils in many fields and the results of the studies reporting the benefits in the field of health have led to an increase in the current value of essential oils and the plants from which they are obtained. Especially the scientific acceptance of some of the alternative medicine methods increased the tendency of people to nature as it was centuries ago and increased the value of raw materials. Essential oil plants and essential oils that have a significant economic share in Turkey and the world are considered local livelihoods for people. The important thing is to be aware of the existing natural riches at hand and to use their potential and yields fully.

The world trade of essential oils is estimated to be around 120.000 - 130.000 tons and over 1 billion USD. A total of 15 essential oils, each of which with an annual production of more than 500 tons, corresponding to 90% of world production. The value of the 18 most important essential oils covers 75% of the total production value.

A total of 65% of the total essential oil production is obtained from woody plants (i.e. trees and shrubs), which include light in weight but heavy in value citrus oils, and light in weight but heavy in value rose, jasmine and vetiver oils. Citrus and peppermint oils lead the world's essential oil market.

Developing countries have tremendous potential in essential oil production (65% of world essential oil production in developing countries and 35% in developed countries). It is expected that the production rate in developing countries will increase in the coming years. Seven leading countries (i.e. China, Brazil, India, Indonesia, Egypt, Morocco, and Turkey) are responsible for 85% of the essential oil production of developing countries.

Major essential oil-exporting countries are China, the European Union, the USA, Brazil, Indonesia, and India, which realize 66% of essential oil exports (Baser, 2000).

Developed countries are the main users of essential oils. The European Union, USA, Japan, Switzerland, and Canada make up 70% of the total

imports (the European Union alone 43%). Annual imports of essential oils are estimated to be around 95.000 tons versus 900 million US dollars.

in the pharmaceutical industry, approximately 25% of the plants are used as raw materials. It is necessary to know the plants better to better know the plants as a source of healing for people with their different characteristics aside from their essential oils and to use their full potential. Chemotaxonomy, which is among the classification methods used for the identification of plants, and the importance of essential oils used in the creation of chemotaxonomy are better understood with the developing technology and new studies are constantly added to the literature. The importance of essential oils in the use of living things and plant classification is increasing. When the economic benefits are considered, it can be argued that the importance of being well known to people increased even more. There is no doubt that when these riches, which nature provides free of charge, are fully understood, the awareness of their values and importance will increase. The tendency to plants and their products is increasing with each passing day in the most developed countries of the world. The usage areas of essential oils, which are under the title of secondary metabolites, are expanding and new theories are emerging in this regard. Conscious and controlled use of these components will lead to the emergence of new fields. It is clear that the inclusion of products of nature in life by preserving their main structure and analyzing them will lead to innovations in many areas, especially healthcare.

What is needed to do is to be aware of the existing riches and protect them and provide scientifically new data to be able to use the main structures without disturbing their naturalness. Basing the theories in this field on scientific data will increase the reliability of these components. For this reason, care should be taken that their use is based on products that have been proven by scientific studies. People should be informed about the ways of conscious consumption, and products that are inspected and approved by the relevant institutions should be preferred because they provide economic gains. Controlled use and results will increase the protection and value of these riches. The versatile use of essential oils in different fields is among the important indicators of richness and free gifts of nature.

REFERENCES:

Alaca, F., & Arslan, N. (2012). Sekonder metabolitlerin bitkiler açısından önemi. *Ziraat Mühendisliği*, (358), 48-55.

Atal, C. K., & Kapur, B. M. (1982). Cultivation and utilization of aromatic plants.

Avesis. (2022). Bitkilerin sınıflandırılması ders notları. İstanbul Üniversitesi.

Aydın, E. (2019). Sabit ve uçucu yağların sağlık ve kozmetikte kullanımı. Erciyes üniversitesi, bitirme ödevi.

Bakkali, F., Averbeck, S., Averbeck, D., & Idaomar, M. (2008). Biological effects of essential oils–a review. *Food and chemical toxicology*, *46*(2), 446-475.

Başer, K. H. C. (2000). Uçucu yağların parlak geleceği. *Tıbbi ve Aromatik Bitkiler Bülteni*, *15*, 20-33.

Başer, K. H. C. (2009). Uçucu yağlar ve aromaterapi. *Fitomed*, 7, 8-25.

Bhargava, V. V., Patel, S. C., & Desai, K. S. (2013). Importance of terpenoids and essential oils in chemotaxonomic approach. *International Journal of Herbal Medicine*, *1*(2), 2321-2187.

Bernáth, J., Németh, É. (2007). Chemical systematization of the genus Foeniculum Mill. based on the accumulation and qualitative differentiation of the essential oil. *Natural Product Communications*, *2*(3), 1934578X0700200313.

Cruz, A. V. M., Ferreira, M. J., Scotti, M. T., Kaplan, M. A., Emerenciano, V. P. (2008). Chemotaxonomic relationships in Celastraceae inferred from principal component analysis (PCA) and partial least squares (PLS). *Natural Product Communications, 3*(6), 1934578X0800300617.

Çalışkan, T., Maral, H., Pala, C., Kafkas, E. & Kırıcı, S. (2019). Morphogenetic variation for essential oil content and composition of sage (*Salvia officinalis* L.) in Çukurova conditions*. Arabian Journal of Medicinal and Aromatic Plants, 5*(1):32-38.

Çelik, E., & Çelik, G. Y. (2007). Bitki uçucu yağlarının antimikrobiyal özellikleri. *Orlab On-Line Mikrobiyoloji Dergisi*, *5*(2), 1-6.

De Silva, T. (Ed.). (1995). *A manual on the essential oil industry*. United Nations Industrial Development Organization.

Dığrak, M., & İlçim, A. (2002). Sistematiğin Esasları. Kahramanmaraş Sütçü İmam Üniversitesi Fen Edebiyat Fakültesi Biyoloji Bölümü, Kahramanmaraş, 71.

Elkiran, O., Akbaba, E., & Bagci, E. (2018). Constituents of essential oils from leaves and seeds of Laurus nobilis L.: A Chemotaxonomic approach. *Bangladesh Journal of Botany*, *47*(4), 893-901.

Elkiran, Ö., & Karakaya, M. (2021). The Essential Oils of Laurus nobilis L. and Molecular-Spectroscopic Analysis for 1, 8-Cineole. *Sakarya University Journal of Science*, *25*(3), 718-726.

Erdoğan, E. A. (2012). Bitki uçucu yağlarının kullanım alanları ve muhtemel genetik etkileri. *Mersin Üniversitesi Tıp Fakültesi Lokman Hekim Tıp Tarihi ve Folklorik Tıp Dergisi*, *2*(2), 21-24.

Giray. S. & Kırıcı, S. (2021). Esans yağlarda etkicil madde belirleme yöntemleri. Esans yağlar, İksad publishing house, 3:55.

Handa, S. S. (2008). An overview of extraction techniques for medicinal and aromatic plants. *Extraction technologies for medicinal and aromatic plants*, *1*, 21-40.

Hegnauer, R. (1986). Phytochemistry and plant taxonomy-An essay on the chemotaxonomy of higher plants. *Phytochemistry*, *25*(7), 1519-1535.

Karık, Ü., Çiçek, F., Tutar, M., & Fırat, A.Y.A.S. (2015). Türkiye defne (Laurus nobilis L.) populasyonlarının uçucu yağ bileşenleri. *Anadolu Ege Tarımsal Araştırma Enstitüsü Dergisi*, *25*(1), 1-16.

Kaya, D.A, İnan, M., Giray, E.S. & Kırıcı, S. (2012). Diurnal, ontogenetic and morphogenetic variability of *Lavandula stoechas* L. ssp. stoechas in East Mediterranean Region. *Revista de Chimie* 63(8):749-753.

Kırıcı, S. & Giray. (2021). Aromatik bitkilerden esans yağ elde etmede kullanılan ekstraksiyon yöntemleri. Esans yağlar, İksad publishing house, 2:27.

Kırıcı, S. & İnan, M. (2001). Effect of different harvesting time on the essential oil content of the rosemary (*Rosmarinus officinalis* L.) in the Çukurova condition, *Workshop on Agricultural and Quality Aspects of Medicinal and Aromatic Plants* 29 May – 1 June. Proceeding Book S.263-272. Adana, Türkiye.

Labra, M., Miele, M., Ledda, B., Grassi, F., Mazzei, M., Sala, F. (2004). Morphological characterization, essential oil composition and DNA genotyping of *Ocimum basilicum* L. cultivars. *Plant Science, 167*(4), 725-731.

Mammadov, R. (2014). Tohumlu Bitkilerde Sekonder Metabolitler. Nobel Akademik Yayıncılık, Yayın No: 841. *Fen Bilimleri*, (978-605), 133-743.

Maral, H. & Kırıcı, S. (2019). Changes within the daytime of essential oil content and composition of zahter (*Thymbra spicata* L.) grown in Ermenek conditions. *Turkish Journal of Agriculture-Food Science and Technology* 7(2):13-16.

Maral, H., Çalışkan, T., Yıldırım, C.D., Akdoğ an, M. E., Kafkas, N.E.& Kirici S. (2018). The influence of harvesting period and cutting hour on yield and quality in thyme (*Thymus vulgaris* L.) in Çukurova condition. *ARCTIC Journal*, 71(11):82-88.

McNair, J. B. (1935). Angiosperm phylogeny on a chemical basis. *Bulletin of the Torrey Botanical Club*, 515-532.

Rasool, R., Ganai, B. A., Akbar, S., Kamili, A. N., & Masood, A. (2010). Phytochemical screening of Prunella vulgaris L.-an important medicinal plant of Kashmir. *Pak. J. Pharm. Sci*, *23*(4), 399-402.

Raut, J. S., & Karuppayil, S. M. (2014). A status review on the medicinal properties of essential oils. *Industrial crops and products*, *62*, 250-264.

Sangun, M. K., Aydin, E., Timur, M., Karadeniz, H., Caliskan, M., & Ozkan, A. (2007). Comparison of chemical composition of the essential oil of Laurus

nobilis L. leaves and fruits from different regions of Hatay, Turkey. *Journal of Environmental Biology*, *28*(4), 731-733.

Singh, R. (2016). Chemotaxonomy: a tool for plant classification. *Journal of Medicinal Plants*, *4*(2), 90-93.

Sivarajan, V. V., & Robson, N. K. (1999). *Introduction to the principles of plant taxonomy*.

Smith, P. M. (1976). *The chemotaxonomy of plants* (No. 581.192 S5).

Tanker, M., & Tanker, N. (1990). Farmakognozi. *Ankara Üniversitesi Eczacılık Fakültesi Yayınları*, *65*(2), 301-302.

Temel, M., Tinmaz, A. B., Öztürk, M., & Gündüz, O. (2018). Dünyada ve Türkiye'de tıbbi-aromatik bitkilerin üretimi ve ticareti. *Kahramanmaraş Sütçü İmam Üniversitesi Tarım ve Doğa Dergisi*, *21*, 198-214.

Tübitak. (2008). Tübitak Bilim ve Teknik Dergisi. Eylül sayısı.

Uma, M.M. (2010). Bitki toplama, teşhis ve herbaryum teknikleri. Çukurova Üniversitesi, Fen Bilimleri Enstitüsü. Yüksek Lisans Tezi.

Wink, M., & Waterman, P. G. (1999). Chemotaxonomy in relation to molecular phylogeny of plants. *Annual Plant Reviews*, *2*, 300-341.

Yaprak, A.E. (2022). https://acikders.ankara.edu.tr/course/info.php?id=868.

Yaylı, N. (2013). Uçucu Yağlar ve Tıbbi Kullanımları, Karadeniz Teknik Üniversitesi Eczacılık Fakültesi Yayınları, 1-2-4.

Yollu, B. (2009). *Myrtus communıs* (Yabani mersin) türünün farklı kısımlarında (yaprak, meyve ve odun) kimyasal bileşenlerin belirlenmesi. *Fen Bilimleri Enstitüsü, Orman Endüstri Mühendisliği Anabilim Dalı. Yüksek Lisans Tezi, 110s*.

Yurteri E., Küplemez, H. and Seyis, F. (2021). Esans yağ üretiminde yaygın olarak kullanılan aromatik bitkiler ve bu bitkilerin kısımları. Esans Yağlar, İksad Yayınevi, Ankara, 5:123.

CHAPTER 5

EFFECTS OF LEAVES AND LITTER OF *OLEA EUROPAEA* L. ON SOIL ORGANIC CARBON MINERALIZATION: A LABORATORY STUDY

Burak KOÇAK[1]

Şahin CENKSEVEN[2]

1 Research Assistant Dr., Department of Biology, Faculty of Science and Arts, Cukurova University, Adana, Turkey, *Corresponding Author: bkocak@cu.edu.tr, ORCID ID: 0000-0003-4144-6079

2 Lecturer Dr., Department of Soil Science and Plant Nutrition, Faculty of Agriculture, Cukurova University, E-mail: scenkseven@cu.edu.tr, ORCID ID: 0000-0003-2330-8668

1. INTRODUCTION

Soil microorganisms are unique organisms that are important players in the processes of decomposition, mineralization and immobilization of all plant and animal residues (Figure 1). These microorganisms regulate the processes of organic carbon inputs and outputs in the soil ecosystem. It's essential to interpret the behaviours of the soil microorganisms to gain better understanding in the soil carbon sequestration (Brookes et al. 2008).

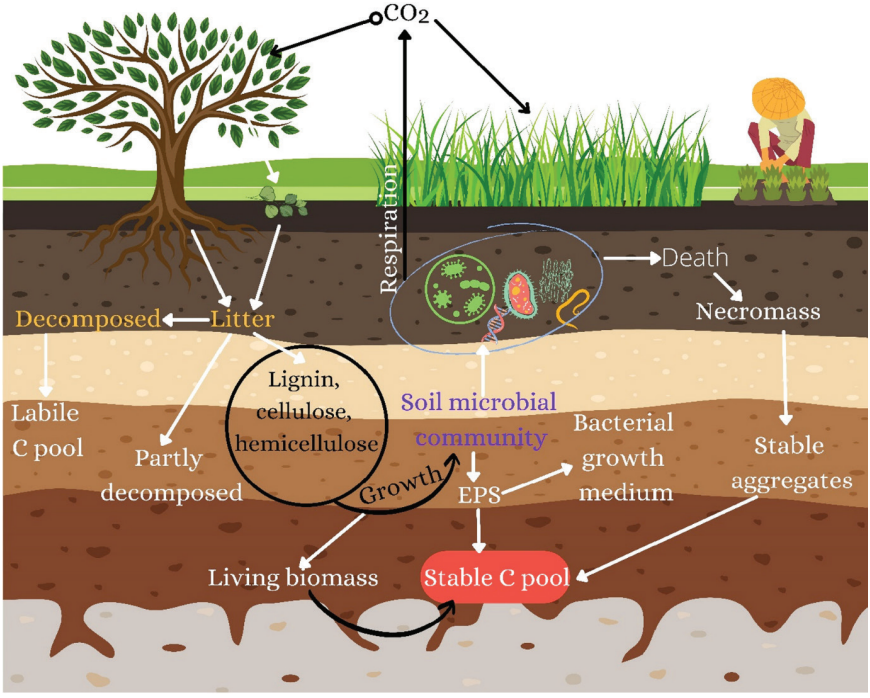

Figure 1 *Relations of soil microbial communities with distinct carbon pools in the soil ecosystems (Bhattacharyya et al., 2022).*

Soil microorganisms sustain their lives by utilizing the two fundamental carbon sources to obtain energy: 1) inputs of fresh plant and animal residues 2) humified soil organic matter (Figure 1). The most readily available and energy producer materials per unit carbon are the fresh biological organic inputs. Large molecules like cellulose and protein are efficiently break down and converted into small subunits like monosaccharide and amino acid that will be assimilated by the microbial cells (Figure 1). During this process, between 40% and 60% of organic carbon in these substrates transformed into CO_2. Soil organic matter fundamentally occur as a result of the functions of soil microorganisms on these fresh inputs. With the continuous recycling of microbial biomass, microorganisms are eventually converted into biological carbon forms

whose half-lives are more than centuries (Jenkinson et al. 1992).

Organic matter stored in the soil is structurally different from organic materials that are freshly introduced to the soil while it has complex chemical structure. This structure can be changed in size and consists of large number of non-sequential molecules and many various functional groups such as carboxyls, fenolic and alcholic hydroxyls, carboniles, amino (Tate III, 1992). Due to irregular reactions catalyzed by the active enzymes in the dead cells and random condensations of reactive products generated from the decomposition of compounds including quinone, lignin, cellulose and nitrogen, these molecules have no stable polymeric characterization which biological macromolecules have (Stevenson, 1994). Deficiency of polymeric structure has an active role in the resistance of soil organic matter to microbial decomposition and the physical protection of organic matter (Watts et al., 2001). However, soil microbial biomass, which survive after months and even years, can slowly mineralize soil organic matter and CO_2 occurs slowly in this process (Figure 2) (Joergensen et al., 1990). High amounts of organic carbon are globally sequestrated in the soils and estimation of this amount was reported as 1400 gigatons at 1 m soil depth (Post et al., 1982). Thus, this magnificent transformation process contributes largely in the Earth's carbon cycle and release of greenhouse gas emissions such as CO_2, NO etc. (Figure 2).

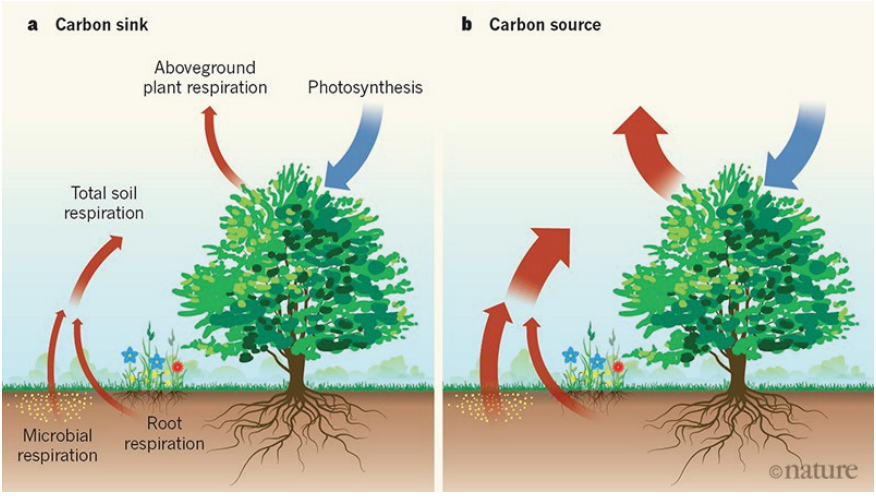

Figure 2 *Carbon fluxes at Earth's surface a. as carbon sink b. as carbon source (Ogle, 2018).*

Two of the main pathways of carbon dioxide release are soil and plant respirations in the terrestrial ecosystems (Glanville et al. 2012). It's noted that soils contain 1500 Pg C pool size which is the twice of atmospheric pool size and global flux from soil respiration was estimated as 73 Pg C

y^{-1} which is more than other terrestrial-atmospheric carbon releases except for gross primary production (Schlesinger and Andrews, 2000; Rustad et al., 2000). Roots of plants and microbial decomposition of organic matter in the soil produce CO_2. Carbon release from soil relies on many soil factors (soil moisture, temperature, pH etc.), plant factors (vegetation communities, root density, litter inputs etc.) and alterations by human intervention (heavy metal accumulation, land use management, pollution etc.) (Raich and Tufekcioglu, 2000). The availability of labile carbon substrates in the soil generally restraint the soil microbial activities and respiration (Demoling et al., 2007), which these substrates are originated from root exudates (Jones et al., 2009) and turnover of dead roots (Gill and Jackson, 2000).

It's reported that area of olive gardens is 10.5 ha in the worldwide (Figure 3) (FAO, 2021). Olive trees have low fruit yields due to water deficiency and in particular they are well adapted to arid regions like areas under Mediterranean climate. Olive is a natural evergreen and essential fruit tree in the Mediterranean Region (Malamidou et al., 2018). Olive trees contribute an important amount of litter to the soil ecosystems and 90% of this amount consists of its leaves (Stevenson, 1994).

Figure 3 *Worldwide distribution of olive trees (Cimato and Attilio, 2011)*

Soil organic carbon (SOC) turnover can be increased in short term by adding an external organic substrate and this is called as "priming effect" (Kuzyakov, 2010). Priming effects of plant materials or easy decomposable substances on soil have been widespread studied which are represent for the organic carbon inputs in the natural ecosystems (Wang et al. 2014). However, it has been reported that directions of priming effects are inconsistent with each other in the different experiments and when organic carbon introduced into the soil, positive priming (Fontaine et al., 2007; Zhang & Wang, 2012), negative priming and neutral priming effects were

found (Hamer & Marschner, 2005; Nottingham et al., 2009). Plant litter is the main source of soil organic carbon in the forest ecosystems and it can change the rate of SOC mineralization (Wang et al., 2014).

In this study, effects of olive leaves and litter on SOC mineralization in the olive trees (*Olea europaea* L., Oleaceae) that naturally grow in Cukurova University Campus (Adana, Southern Turkey). Olive leaves and litter were added to the soil at 0.5% and 1% and these soil+plant material mixtures were humidified at 80% of field capacity and incubated at 28°C for 52 days.

2. MATERIAL AND METHODS

2.1. Material and Study Area

Soil, leaf and litter samples of olive (*Olea europaea* L.) have been taken from a natural olive grove in Cukurova University Campus, Adana (37°3'26" N, 35°21'19" E), Turkey, in October 2021. Mean annual precipitation and temperature in Adana were 659 mm and 19.1°C for 35 years and this region had the semi-arid Mediterranean climate (Kum and Celik, 2014).

After air drying, olive soils were sieved through a 2 mm mesh sieve and olive leaves and litter were powdered before analysis. Soil texture, soil pH and soil field capacity were determined by Bouyoucos hydrometer, a 1:2.5 soil-water suspension with pH-meter (inoLab pH/Cond 720, WTW GmbH, Weilheim, Germany) and 1/3 atmospheric pressure with a vacuum pump, respectively (Kacar, 2012). Organic carbon and total nitrogen concentrations in the olive soil, leaf and litter samples were measured by using a modified Walkley and Black method and Kjeldahl method, respectively (Kacar, 2012).

2.2. Soil Carbon Mineralization and Kinetics

Olive leaves (0.5% Leaf and 1% Leaf) and litter (0.5% Litter and 1% Litter) were mixed with its soil at 0.5% and at %1 doses. For this purpose, 100 g soil and plant material were first mixed and then placed in 750 ml incubation vessels. These mixtures were humidified at the 80% of soil field capacity and then were incubated at 28°C for 52 days. Soils untreated with leaves or litter were used as control. As a result of soil microbial activity, CO_2 was trapped periodically by 10 ml 1 M NaOH solution in beakers which are placed in incubation vessels. Amount of respired CO_2 was determined with the titration with 1 M HCl in the incubation vessels. Three replicates were used for each treatment and control. After 52 days of incubation, all measured CO_2 during the incubation were summed up to calculate cumulative carbon mineralization (C_{min}, mg CO_2-C/100 g soil) and these values were divided by soil organic carbon level to

obtain the rate of C_{min} (Koçak and Darıcı, 2016). A first order kinetic model proposed by Ajwa and Tabatabai (1994) was used to simulate the relationship between the cumulative C_{min} quantity and incubation time in all treatments: $C_{min} = C_0 (1 - e^{-kt})$. C_{min} is the amount of cumulative carbon mineralization through incubation period (days) while C0 is the quantity of potentially mineralizable carbon in the soil and k (day^{-1}) is the mineralization rate constant.

2.3. Statistical Analysis

The data obtained from the laboratory incubation were submitted to ANOVA to show the differences between treatments by using the SPSS v.20 software. The separation of averages of control and treatments were made by using Tukey's HSD and differences between the means of control and treatments were declared as significant at $P<0.05$.

3. RESULTS AND DISCUSSION

3.1. Some Properties of Olive Soil, Leaf and Litter Samples in Cukurova University Campus

Some physical and chemical properties of olive soils and organic carbon and total nitrogen contents of leaves and litter were given in Table 1. Olive soils were sandy clay loam and slightly basic. Organic carbon, total nitrogen contents and C/N rate of soils were 4.23%, 0.520% and 8.13, respectively (Table 1). Koçak and Darıcı (2022) reported that natural olive soils in Cukurova University Campus were clay at 0-10 cm depth while organic carbon contents of soils were between 2.68% and 3.87%, total nitrogen contents of soils were between 0.179% and 0.378%, C/N rates were between 10.46 and 16.28 between 2013-2015. Sağlıker and Darıcı (2005) claimed that natural olive soils were sandy loam at 0-10 cm soil depth in Cukurova University Campus while organic carbon contents of these soils were between 1.99% and 3.31%, total nitrogen contents of soils were between 0.19% and 0.33% and C/N rates were between 11.4 and 11.7 between 1999-2000. Differences in results between the current study and past studies may be caused by different sampling times and sampling trees.

Organic carbon and total nitrogen contents of olive leaves and C/N of leaves were 42.03%, 1.340% and 31.35, respectively (Table 1). These contents and C/N of litter were 31.09%, 0.753% and 41.31, respectively (Table 1). Sağlıker and Darıcı (2005) indicated that organic carbon contents and total nitrogen contents of natural olives leaves were between 35.4% and 47.6% and between 1.15% and 1.77% in Cukurova University Campus, respectively. In the latter study, organic carbon and total nitrogen contents of litter were between 30.0% and 46.9% and between 0.87% and 1.36% (Sağlıker and Darıcı, 2005). Malamidou et al. (2018) noted that

organic carbon and total nitrogen contents (mg g^{-1}) of leaves in a olive grove were 520 and 15.0, respectively. Obtained results of litter and leaves were consistent with these studies.

Table 1 *Some properties of olive soil, leaf and litter samples in Cukurova University Campus (mean±standard error, n=3)*

Olea europaea L. (Olive)				
	Clay (%)	28.67	±	0.68
	Silt (%)	22.82	±	1.79
	Sand (%)	48.51	±	1.18
	Texture	Sandy Clay Loam		
Soil	Field Capacity (%)	37.60	±	0.26
	pH	7.27	±	0.08
	Organic Carbon (%)	4.23	±	0.05
	Total Nitrogen (%)	0.520	±	0.020
	C/N	8.13	±	0.08
	Organic Carbon (%)	42.03	±	1.36
Leaves	Total Nitrogen (%)	1.340	±	0.017
	C/N	31.35	±	0.64
	Organic Carbon (%)	31.09	±	0.75
Litter	Total Nitrogen (%)	0.753	±	0.015
	C/N	41.31	±	1.48

3.2. Soil CO_2 Evolution and Kinetics

The biogeochemical C cycle have an active role in the linkages between plant vegetation and soil ecosystems (Regina and Tarazona, 2000). One of the main significant processes in the regulation of functioning of natural and agricultural ecosystems is the soil organic carbon mineralization (Johnson, 1995). The nutrient flux in the soil is controlled by the rate of carbon mineralization because the energy sources constrain nutrient availability in the soil to maintain the populations of soil microorganisms (Núñez et al. 2001, Saggar et al. 2001). Prediction of carbon mineralization rate is an easy method to control how C stored in terrestrial ecosystems reacts to changes occurred in vegetation or climate because most of the detrital carbon stored in terrestrial ecosystems can be found in mineral soil (Giardian et al., 2001). Thus, evaluation of biological process of ecosystem evolution requires the scientific modelling of soil C mineralization and its pathway in a dynamic environment (Su et al. 2004).

Cumulative carbon mineralizations [mg $C(CO_2)$/100 g soil] in the soils added with olive leaves (0.5% and 1%) and litter (0.5% and 1%) were between 167.46 (control) and 326.07 (1% leaf) in the end of incubation period (Figure 4). Addition of olive leaves and litter in all doses significantly increased soil microbial respiration compared to control ($P<0.05$). However, there

were found no significant differences between the same doses of leaves and litter in the cumulative carbon mineralization.

Rates of carbon mineralizations were between 3.96% (Control) and 7.02% (1% leaf and 1% litter) after 52 days of incubation (Figure 5). C mineralization rates were significantly increased by the addition of olive leaves and litter ($P<0.05$, Figure 5). However, no significant differences were found between the same doses of leaves and litter in rate of carbon mineralization.

Kocak and Darıcı (2016) added the leaves of bay leaves (*Laurus nobilis* L.) to its soil at the half and same amount of soil organic carbon and measured the carbon mineralization under laboratory conditions. After 54 days of incubation, addition of leaves to soil significantly enhanced soil organic carbon mineralization ($P<0.05$). Cenkseven et al. (2017) added the leaves of oleander (*Nerium oleander* L.) to its soil at the half, same and twice of soil organic carbon concentration and measured the carbon mineralization. Addition of oleander leaves stimulated soil organic carbon mineralization in two levels of field capacity (60% and 80% of field capacity)

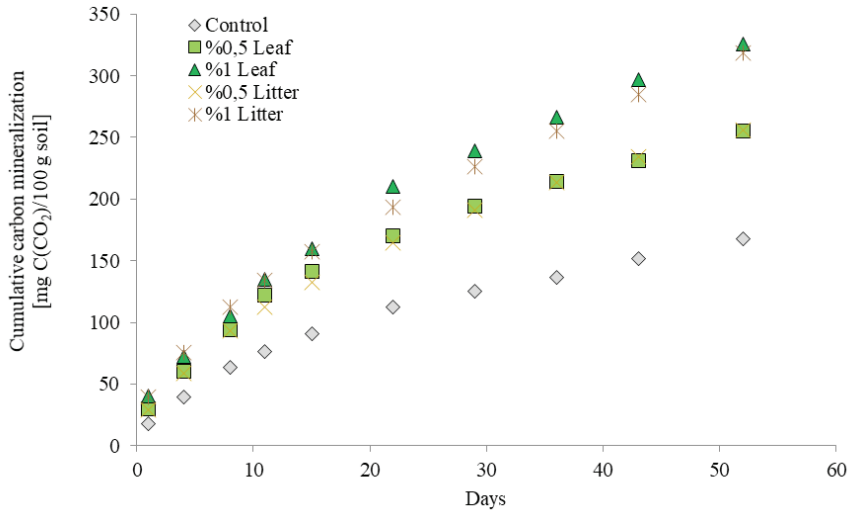

Figure 4 *Cumulative carbon mineralizations in the soils added with olive leaves and litter at 0.5% and 1% (n=3)*

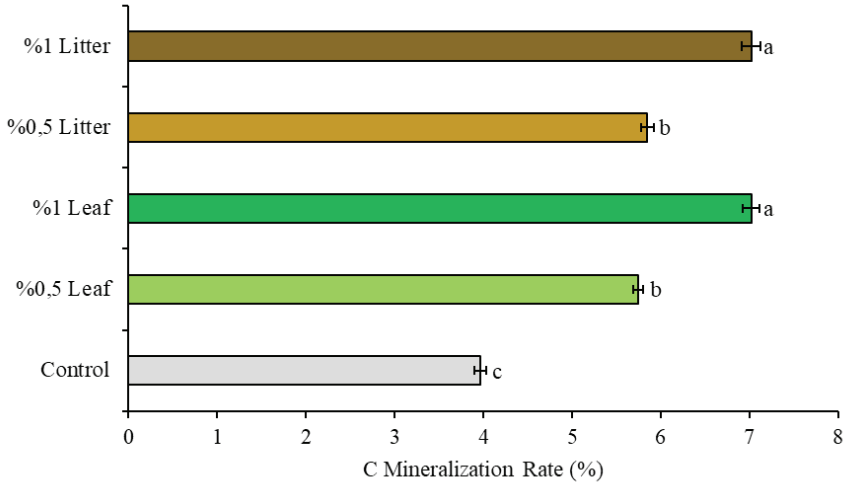

Figure 5 *Rates of carbon mineralization in the soils added with olive leaves and litter at 0.5% and 1%. Each column in graphs represents the mean of three replicates ± standard. Lowercase letters denote significant differences between treatments based on Tukey's HSD (P<0.05).*

In general, carbon mineralization dynamics in incubation studies can be expressed as a mathematical equation to predict the ability of soils in providing potential mineralizable organic carbon and to determine the balance of organic matter (Riffaldi et al., 1996). One of the descriptive ways of soil organic carbon mineralization is the usage of the first-order equation. This model was originally suggested by Jones (1984) for nitrogen mineralization and includes a parameter that defines a pool of decomposable substrate in a easy way which produce a mineralization flush (C_0) in the first incubation interval. In addition, this model is one of the most suitable kinetic models that describe the decomposition and mineralization of various organic material types (Saviozzi et al. 1993). In the current study, potentially mineralizable carbon (C_0, mg $C(CO_2)$ 100 g^{-1} soil) values obtained by the first-order equation ranged from a minimum of 169.17 for control to a maximum of 355.91 (1% leaf) in Table 2. In addition, carbon mineralization constant rates ($days^{-1}$) differed among the treatments and all obtained values in this study were ranged between 0.041 (1% leaf) and 0.054 (0.5% leaf) in Table 2. These k values in the current study indicated that organic materials metabolized in the microbial respiration were similar or had the same levels of availability (Riffaldi et al., 1996).

Table 2 *Parameter estimates according to the first-order equation model for carbon mineralization in the olive soils added with olive leaves and litter (C_0: potentially mineralizable carbon in the soil, C_{min}: mineralized soil carbon at the end of the incubation period, k: mineralization rate constant)*

	C_0	C_{min}	k
	mg $C(CO_2)$/100 g soil		$days^{-1}$
Control	169.17	167.46	0.052
0.5% Leaf	257.91	254.91	0.054
1% Leaf	355.91	326.07	0.041
0.5% Litter	269.68	256.23	0.047
%1 Litter	337.66	318.29	0.043

4. CONCLUSIONS

Soil microorganisms are key players in the mineralization of soil organic matter. Heterotrophic microorganisms require the organic materials such as litter, roots and their exudates to sustain their lives in the soil ecosystems. Decomposition of plant materials in the soil relies on the abiotic (water content, temperature, texture etc.) and biotic (soil microbial communities, microbial enzymes etc.). This study suggested that addition of olive litter and leaves enhanced soil organic carbon mineralization. In conclusion, olive leaves and litter are beneficial for the soil microbial communities.

5. ACKNOWLEDGEMENTS

This study was funded by the Scientific Research Project Unit of Cukurova University under the project number FBA-2021-13905. Authors thank Ecem Abay, Güneş Ayma and İbrahim Mert Kayıran (Cukurova University, Department of Biology) for their contributions in the soil sampling in the field and soil physical and chemical analysis.

REFERENCES

Ajwa, H. A., & Tabatabai, M. A. (1994). Decomposition of Different Organic Materials in Soils. *Biology and Fertility of Soils*, 18(3), 175-182.

Bhattacharyya, S. S., Ros, G. H., Furtak, K., Iqbal, H. M., & Parra-Saldívar, R. (2022). Soil Carbon Sequestration–An Interplay Between Soil Microbial Community and Soil Organic Matter Dynamics. *Science of The Total Environment*, 152928.

Brookes, P.C., Cayuela, M.L., Contin, M., De Nobili, M., Kemmitt, S.J. & Mondini, C. (2008). The Mineralisation of Fresh and Humified Soil Organic Matter by The Soil Microbial Biomass. *Waste Management*, 28, 716-722.

Cimato, A., & Attilio, C. (2011). Worldwide diffusion and relevance of olive culture. In *Olive Diseases and Disorders*, Schena, L., Aosteo, G.E., Cacciola, S.O. (Eds), 1-21, Transworld Research Network.

Demoling, F., Figueroa, D., & Bååth, E. (2007). Comparison of Factors Limiting Bacterial Growth in Different Soils. *Soil Biology and Biochemistry*, 39(10), 2485-2495.

FAO. (2021). http://www.fao.org/faostat/en/#data/QC.

Fontaine, S., Barot, S., Barre, P., Bdioui, N., Mary, B. & Rumpel, C. (2007). Stability of Organic Carbon in Deep Soil Layers Controlled by Fresh Carbon Supply. *Nature*, 450, 277-U210.

Giardina, C. P., Ryan, M. G., Hubbard, R. M., & Binkley, D. (2001). Tree Species and Soil Textural Controls on Carbon And Nitrogen Mineralization Rates. *Soil Science Society of America Journal*, 65(4), 1272-1279.

Gill, R. A., & Jackson, R. B. (2000). Global Patterns of Root Turnover for Terrestrial Ecosystems. The *New Phytologist*, 147(1), 13-31.

Glanville, H., Rousk, J., Golyshin, P., & Jones, D. L. (2012). Mineralization of Low Molecular Weight Carbon Substrates in Soil Solution Under Laboratory and Field Conditions. *Soil Biology and Biochemistry*, 48, 88-95.

Hamer, U. & Marschner, B. (2005). Priming Effects in Different Soil Types Induced by Fructose, Alanine, Oxalic Acid and Catechol Additions. *Soil Biology & Biochemistry*, 37, 445-454.

Joergensen, R.G., Brookes, P.C. & Jenkinson, D.S. (1990). Survival of the Soil Microbial Biomass at Elevated-Temperatures. *Soil Biology & Biochemistry*, 22, 1129-1136

Johnson, W. 1995. Role of carbon in the cycling of other nutrients in forested ecosystems. In *Carbon Forms and Functions in Forest Soils*, Edited by: MeFee, W. W. and Kelly, J. J. 299–328. Madison, Wisconsin

Jones, C. A. (1984). Estimation of an Active Fraction of Soil Nitrogen. *Communications in Soil Science and Plant Analysis*, 15(1), 23-32.

Jones, D. L., Nguyen, C., & Finlay, R. D. (2009). Carbon Flow in the Rhizosphere: Carbon Trading at the Soil–Root Interface. *Plant and Soil*, 321(1), 5-33.

Kacar, B. (2012). *Toprak analizleri* (p. 467s). Ankara: Nobel Yayın Dağıtım.

Kum, G., & Çelik, M. A. (2014). Impacts of Global Climate Change on the Mediterranean Region: Adana as a Case Study. *Procedia-Social and Behavioral Sciences*, 120, 600-608.

Kocak, B. & Darici, C. (2016). Priming Effects of Leaves of *Laurus nobilis* L. And 1,8-Cineole on Carbon Mineralization. *Chilean Journal of Agricultural Research*, 76, 100-104.

Koçak, B., & Darıcı, C. (2022). How Did Soil Depth And Sampling Time Influence on Soil Organic Carbon, Soil Nitrogen, And Soil Biological Properties in a Mediterranean Olive Grove? *Communications in Soil Science and Plant Analysis*, 53(1), 30-44.

Kuzyakov, Y. (2010). Priming Effects: Interactions Between Living and Dead Organic Matter. *Soil Biology & Biochemistry*, 42, 1363-1371.

Nottingham, A.T., Griffiths, H., Chamberlain, P.M., Stott, A.W. & Tanner, E.V.J. (2009). Soil Priming by Sugar and Leaf-Litter Substrates: a Link to Microbial Groups. *Applied Soil Ecology*, 42, 183-190.

Núñez, S., Martínez-Yrízar, A., Búrquez, A., & García-Oliva, F. (2001). Carbon Mineralization in the Southern Sonoran Desert. *Acta Oecologica*, 22(5-6), 269-276.

Ogle, K. (2018). Hyperactive Soil Microbes Might Weaken the Terrestrial Carbon Sink. *Nature* 560, 32-33.

Post, W.M., Emanuel, W.R., Zinke, P.J. & Stangenberger, A.G. (1982). Soil Carbon Pools and World Life Zones. *Nature*, 298, 156-159.

Riffaldi, R., Saviozzi, A., & Levi-Minzi, R. (1996). Carbon Mineralization Kinetics as Influenced by Soil Properties. *Biology and Fertility of Soils*, 22(4), 293-298.

Su, Y., Zhao, H., Li, Y., & Cui, J. (2004). Carbon Mineralization Potential in Soils of Different Habitats in The Semiarid Horqin Sandy Land: A Laboratory Experiment. *Arid Land Research and Management*, 18(1), 39-50.

Malamidou, T., Nikolaidou, A.E., Mamolos, A.P., Pavlatou-Ve, A.K., Kostopoulou, S.K., Menexes, G.C., Anagnostopoulos, C.D. & Kalburtji, K.L. (2018). Litter Dynamics of *Olea europaea* subsp. *europaea* Residues Related to Soil Properties and Microbial N-Biomass in A Mediterranean Agroecosystem. *European Journal of Soil Biology*, 84, 11-18.

Qayyum, M. F., Steffens, D., Reisenauer, H. P., & Schubert, S. (2012). Kinetics of Carbon Mineralization of Biochars Compared With Wheat Straw in Three Soils. *Journal of Environmental Quality*, 41(4), 1210-1220.

Raich, J. W., & Tufekcioglu, A. (2000). Vegetation and Soil Respiration: Correlations and Controls. *Biogeochemistry*, 48(1), 71-90.

Rustad, L. E., Huntington, T. G., & Boone, R. D. (2000). Controls on Soil Respiration: Implications For Climate Change. *Biogeochemistry*, 1-6.

Saggar, S., Yeates, G. W., & Shepherd, T. G. (2001). Cultivation Effects on Soil Biological Properties, Microfauna and Organic Matter Dynamics in Eutric Gleysol and Gleyic Luvisol Soils in New Zealand. *Soil and Tillage Research*, 58(1-2), 55-68.

Sağlıker, H. A., & Darici, C. (2005). Nutrient Dynamics of *Olea europaea* L. Growing on Soils Derived from Two Different Parent Materials in The Eastern Mediterranean Region (Turkey). *Turkish Journal of Botany*, 29(4), 255-262.

Schlesinger, W. H., & Andrews, J. A. (2000). Soil Respiration and The Global Carbon Cycle. *Biogeochemistry*, 48(1), 7-20.

Stevenson, F.J. (1994). *Humus Chemistry: Genesis, Composition, Reactions.* John Wiley & Sons, New York.

Tate III, R.L. (1992). Humic And Fulvic Acids: Formation and Decomposition. In: Soil *Organic Matter: Biological and Ecological Effects,* pp. 147-164. Krieger Publishing Company, Melebar, Florida.

Wang, Q.K., Wang, S.L., He, T.X., Liu, L. & Wu, J.B. (2014). Response of Organic Carbon Mineralization and Microbial Community to Leaf Litter and Nutrient Additions in Subtropical Forest Soils. *Soil Biology & Biochemistry*, 71, 13-20.

Watts, C.W., Whalley, W.R., Longstaff, D., White, R.P., Brooke, P.C. & Whitmore, A.P. (2001). Aggregation of a Soil with Different Cropping Histories Following the Addition of Organic Materials. *Soil Use and Management*, 17, 263-268.

Zhang, W.D. & Wang, S.L. (2012). Effects of NH_4^+ and NO_3^- on Litter and Soil Organic Carbon Decomposition in a Chinese Fir Plantation Forest in South China. *Soil Biology & Biochemistry*, 47, 116-122.

CHAPTER 6

NOVEL PYRIMIDINE SCHIFF BASE: SYNTHESIS, CHARACTERIZATION, DFT ANALYSIS AND DOCKING STUDY

Meltem AYDIN[1]
Burçin TÜRKMENOĞLU[2]
Zülbiye KÖKBUDAK[3*]

1 MSc Student, Department of Chemistry, Faculty of Science, Erciyes University, Kayseri, Türkiye

ORCID ID: 0000-0002-4863-7508

2 Assist. Prof. Dr., Department of Analytical Chemistry, Faculty of Pharmacy, Erzincan Binali Yıldırım University, Erzincan, Türkiye

ORCID ID: 0000-0002-5770-0847

3 Prof. Dr., Department of Chemistry, Faculty of Science, Erciyes University, Kayseri, Türkiye *Corresponding Author: Email: , ORCID ID: 0000-0003-2413-9595

1. Introduction

Pyrimidine is a six-membered pyrimidine ring and aminopyrimidine core compounds found in the structure of some natural products such as Thiamine (Vitamin B1) and marine alkaloids class Meridianins. (Almeida, Resende, da Costa, Pinto, & Sousa, 2021) (Figure 1). The pyrimidine derivatives show wide range of biological andpharmacological activities. Pyrimidines and their derivatives have been reported as anti-viral (Kumar, Deep, & Narasimhan, 2019), anti-tubercular (Siddiqui, Trivedi, Kataria, & Shah, 2014), anti-microbial (Kaur, Aggarwal, Sharma, & Choudhary, 2012), anti-inflammatory (Goudar, Rashmi, Shantharam, Kuntal, & Laxmivenkatesh, 2012), anti-fungal (Ingarsal, Saravanan, Amutha, & Nagarajan, 2007), anti-bacterial (David, Babu, & Reddy, 2014), anti-cancer agents (Ma et al., 2015) (Figure 2). The reactions of aminopyrimidine derivatives with isothiosiyanate, 1,3-dicarbonyl compounds, chloroacetyl chloride, isophthaloyl chloride, chloro acetone and aromatic aldehydes have been reported different experimental conditions (Cimen, Akkoc, & Kokbudak, 2018; Kokbudak et al., 2020; Onal, Ceran, & Sahin, 2008; Onal & Daylan, 2007) (Devim, Akkoc, Zeyrek, Aslan, & Kokbudak, 2022; KÖKbudak, Aslan, & AkkoÇ, 2020). In addition to, metal complexs of compound (1) have been synthesized (Aslan, Akkoc, & Kokbudak, 2020).

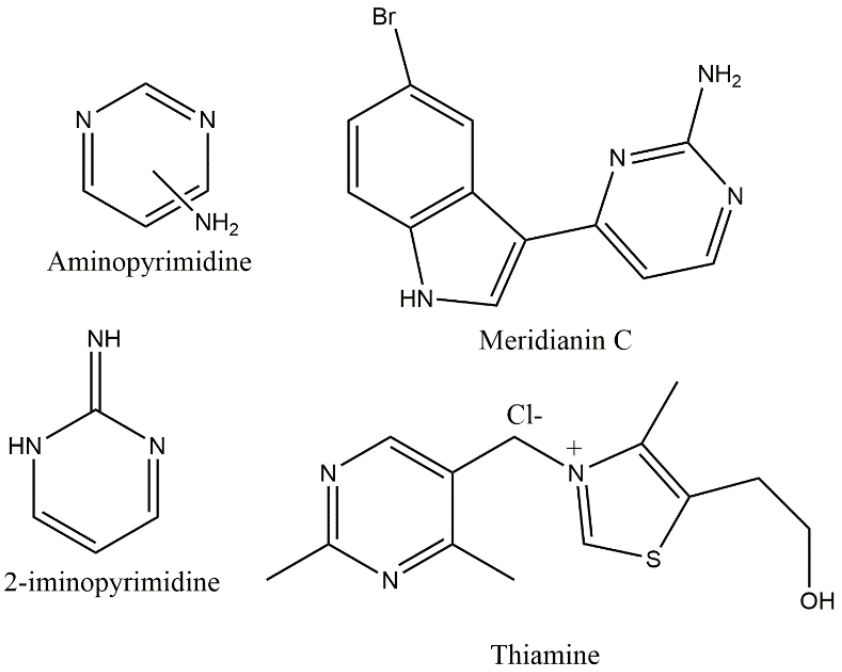

Figure 1. *The aminopyrimidine scaffold.*

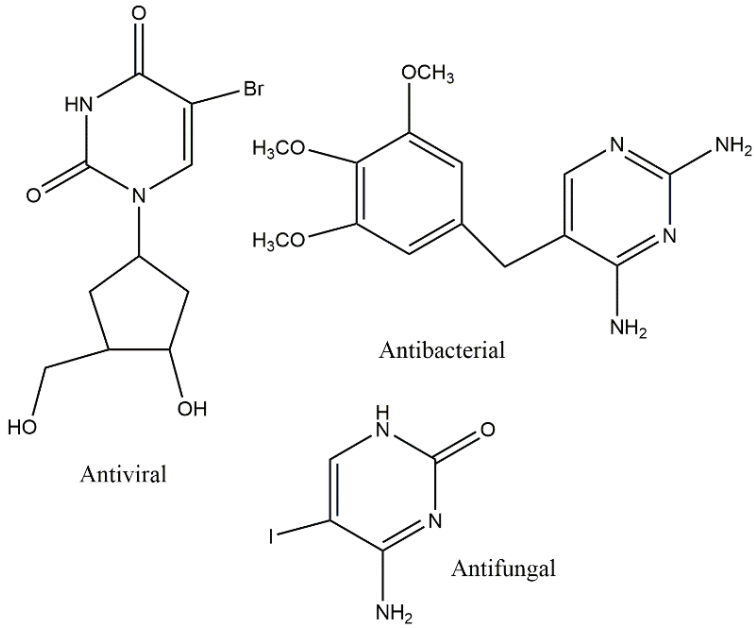

Figure 2. *Antiviral, antifungal, antibacterial active pyrimidine molecules.*

Schiff bases contain an imine or azomethine (–C=N–) functional group. It was first reported by Hugo Schiff (Schiff, 1864) as condensation products of primary amines with carbonyl compounds. Schiff bases are important in pharmaceutical fields due to their effects such as anti-inflammatory (Sathe, Jaychandran, Jagtap, & Sreenivasa, 2011), analgesic (Sondhi, Singh, Kumar, Lozach, & Meijer, 2006), antimicrobial (Jombo, 2011), anticonvulsant (Chaubey et al., 2007), antitubercular (Pandey, Rajavel, Chandraker, & Dash, 2012), anticancer (Ali et al., 2012), antioxidant (Turan, Bingol, Savci, Kocpinar, & Colak, 2021). In addition, Schiff base compounds are used as polymer stabilizers, catalysts, dyes, pigments and intermediates in organic synthesis (Wei, Li, Lu, & Yao, 2006).

The aim of this study is to synthesize heterocyclic compounds containing pyrimidine ring and to examine the efficiency of this compound by DFT and molecular docking. As a first step, 1-amino-5-(4-methylbenzoyl)-4-*p*-tolylpyrimidin-2(1*H*)-one (1) was synthesized from the furan-2,3-dione derivative and acetophenone semicarbazone in benzene. Next, (E)-1-(([1,1'-biphenyl]-4-ylmethylene)amino)-5-(4-methylbenzoyl)-4-(*p*-tolyl)pyrimidin-2(1*H*)-one (2) was prepared from the reaction of compound (1) with biphenyl-4-carbaldehyde under reflux conditions (Scheme 1). The structure of Compound (2) was characterized by IR, ^{1}H NMR and ^{13}C NMR spectral data.

In the molecular docking study, the epidermal growth factor receptor (EGFR) was investigated using the tyrosine kinase domain. Alignment in

molecular docking, surface mapping binding, amino acids and binding energy were calculated. Since theoretical calculations are now considered a good complement for experimental data, the density functional theory (DFT) has become a very important protocol in the investigation of experimental data. These calculations were performed on 6-31 g (d, p) set by DFT method and B3LYP. Using this method, boundary molecular orbitals (FMOs), ighest occupied molecular orbital (HOMO)- lowest unoccupied molecular orbital (LUMO) energy levels, band gap and energy value were found and interpreted.

2. Materials and Method

2.1. Experimental

Since all solvents and reagents are commercially available, they were used in the experimental part without the need for purification. Melting point was not corrected by determination on the digital melting point apparatus (Electrothermal 9100). Compound was routinely checked for homogeneity by TLC using DC Alufolien Kieselgel 60 F254 (Merck) and a Camag TLC lamp (254/366 nm). The instruments we used were the same ones from our other studies (KÖKbudak et al., 2020). IR spectrum was recorded on a Shimadzu Model 8400 FT-IR spectrophotometer. 1H and 13C-NMR spectra were recorded on a Bruker 400(100) MHz Ultra Shield instrument.

2.2. Synthesis of Schiff Base

2.2.1. (E)-1-(([1,1'-biphenyl]-4-ylmethylene)amino)-5-(4-methylbenzoyl)-4-(p-tolyl)pyrimidin-2(1H)-one (2)

A mixture of compound (1) (1 mmol, 0.319 g) and biphenyl-4-carbaldehyde (1.2 mmol, 0.218 g) in 30 mL of ethanol and *p*-toluene sulfonic acid was boiled for 12 hours. The solvent was evaporated with the evaporator and diethyl ether was added onto the remaining solid. It was stirred for 24 hours, filtered and dried. The solid was crystallized twice with ethyl alcohol. The structure of Schiff base (2) was explained with the help of spectroscopic methods. Yield: (65%); m.p.: 231-232 oC; color: yellow. FT-IR: υ = 3054.2 (arom. C-H), 2981.3 (aliph. C-H), 1686.6, 1650.6 (C=O), 1601.7 (C=N), 1567.4 (C=C). 1H NMR (400 MHz, DMSO-d6) δ (ppm) = 9.29 (s, 1H, N=CH), 8.64 (s, 1H, CH in pyrim.), 8.23-7.05 (m, 17H, Ar-H), 2.34, 2.31 (s, 6H, 2CH3-). 13C NMR (101 MHz, DMSO-d6) (ppm) = 192.03 (Ph-C=O), 170.98, 169.42, 166.95, 151.62, 149.16, 143.92, 137.41, 137.33, 133.83, 131.28, 131.06, 130.55, 130.17, 129.11, 129.05, 128.67, 127.38, 126.83, 119.25, 115.94, 99.99 and 24.65-24.61 (2CH3-). Molecular Formula: $C_{32}H_{25}N_3O_2$ and Formula Weight: (483.57 g/mol).

2.3. DFT Calculations

Quantum chemical calculations for **Compound (2)** were calculated using the B3LYP/6 -31 G (d,p) fundamental cluster method (Bozbey et al., 2022) in the Gaussian'09 package program (Frisch et al., 2009). Minimum structural parameters, HOMO, LUMO, ΔE_{gap}, energy values were determined (Oladipo, Yusuf, Zamisa, Shapi, & Ajayi, 2021; Parr, Von Szentpaly, & Liu, 1999).

2.4. Molecular Docking

The Maestro software in the Schrödinger 2021-2 Glide program (Schrödinger Release 2021-2: Glide) was used in the molecular docking study. Molecular docking protocol applied in previous studies was applied. The crystal structure to be used in the *in silico* study was obtained from the Protein Data Bank (https://www.rcsb.org/) Compound (2) was prepared and optimized using Schrödinger Software Suite's LigPrep wizard (Schrödinger Release 2021-2: LigPrep) and minimized using the OPLS2005 force field.

3. Results and Discussion

3.1. Experimental

In this study, compound (1) was prepared from the furan-2,3-dione derivative according to the procedures in the literature. A new Schiff base (2) was synthesized by the condensation of compound (1) with biphenyl-4-carbaldehyde. at 65% (Scheme 1). The compound was purified by recrystallization. Synthesis of Schiff bases are usually carried out by reactions of amines with carbonyl compounds by addition and subtraction. In the IR spectrum of Schiff bases, characteristic stretch bands of carbonyl (C=O) groups are observed. In the 1H NMR spectra of the compounds, the striking peak belongs to the azomethine proton (de Toledo, Pizani, da Silva, Teixeira, & Freire, 2015; Ngan, Lo, & Wong, 2011).

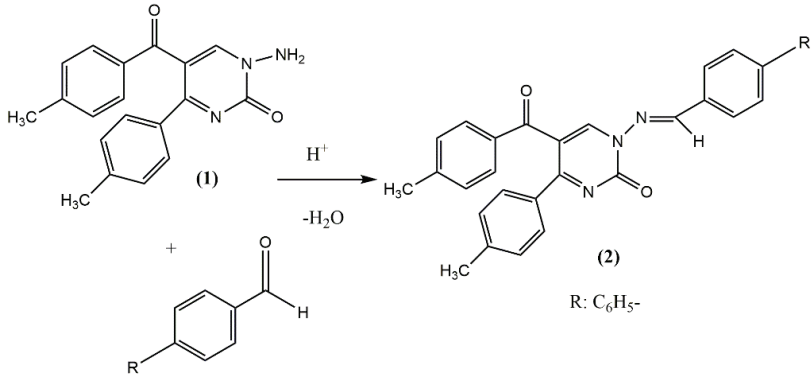

Scheme 1. *A synthesis scheme of compound (***2).**

In the IR spectrum of compound (2), the two C=O absorption bands were observed at 1686 and 1650 cm-1. In the 1H NMR spectrum, the N=CH proton was resonated in the downfield area at δ 9.29 ppm. The proton signal for -CH in the pyrimidine ring for 2 was detected singlet at δ 8.64 ppm. Aromatic protons were observed as multiplet between δ 8.23 and 7.05 ppm. Also, methyl protons were observed singly at 2.34 and 2.31 ppm, respectively. In the 13C NMR spectrum, benzoyl carbon's signal was observed at δ 192.03 ppm. The signals of CH3- groups were observed at 24.64, 24.61 ppm as singlets. Other carbons of the molecule were obtained between δ 169.42-99.99 ppm. The data obtained because of the analyses fully confirmed the structure of Schiff base.

3.2. DFT Calculations

The quantum chemical calculations B3LYP/6 -31 G (d,p) used to explain the electronic and chemical properties of Compound (2) were optimized using the DFT method. The purpose of calculating FMO energies is to identify chemically active sites of the molecule. This theoretical calculation plays an important role in explaining the state of molecules, as it concerns the specific movement of electrons from one energy state to another. In Figure 3, the energy gap value of the molecule was calculated as 3.942 eV. The energy gap, which reveals the stability of the compound's structure, also reflects the chemical activity of the molecule.

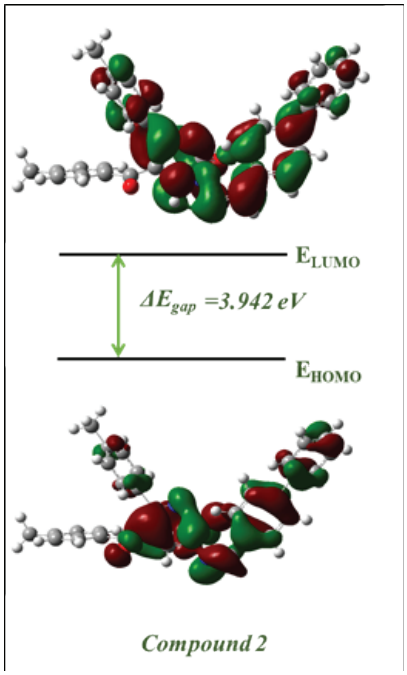

Figure 3. *HOMO-LUMO structures of the* **Compound (2)**.

FMOs, the HOMO and LUMO play an important role in understanding the chemical properties of a molecule. The HOMO-LUMO orbitals of the capped compound are shown in Figure 3. With the help of molecular electrostatic potential (MEP) maps created as a result of quantum chemical calculations, the active sites of drug molecules can be determined (Silverstein & Bassler, 1962).

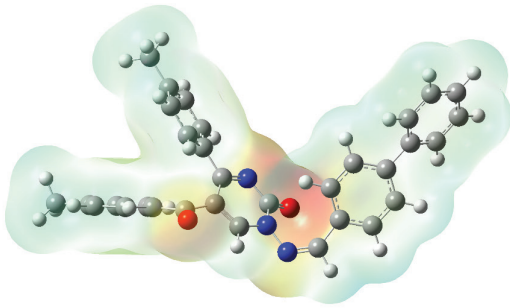

Figure 4. *MEP structure of the* **Compound (2).**

3.3. Molecular Docking

Molecular docking studies were applied to determine the binding interactions of Compound (2) on EGFR by in silico approaches. Therefore, the crystal structure of EGFR (PDB ID: 4HJO (Park, Liu, Lemmon, & Radhakrishnan, 2012)) was used as the primary target for this study. The binding parameters of the molecular docking results of Compound (2) and Erlotinib compounds interacting with the EGFR crystal structure in-silicon are given in Table 1.

Table 1. *Parameter values calculated by molecular docking with 4HJO crystal structure of Compound (2) and Erlotinib.*

Parameters	**Compound (2)**	**Erlotinib**
Glide Energy	-43.034	-56.809
Glide Gscore	-8.766	-9.608
Docking Score	-8.766	-9.608
Glide Emodel	-74.860	-87.554
ΔG_{Bind}	-81.39	-89.81

When the binding parameter values of Compound (2) in Table 1 were examined, the free binding energy was -81.39 kcal/mol, while the Erlotinib value was determined as -89.81 kcal/mol, which is a close value. In addition, when the docking score values in Table 1 were examined, the value of Compound (2) was -8.766 kcal/mol, while the value of Erlotinib was -9.608 kcal/mol. When these values are examined, it can be said that the binding parameter results of Compound (2) can be considered.

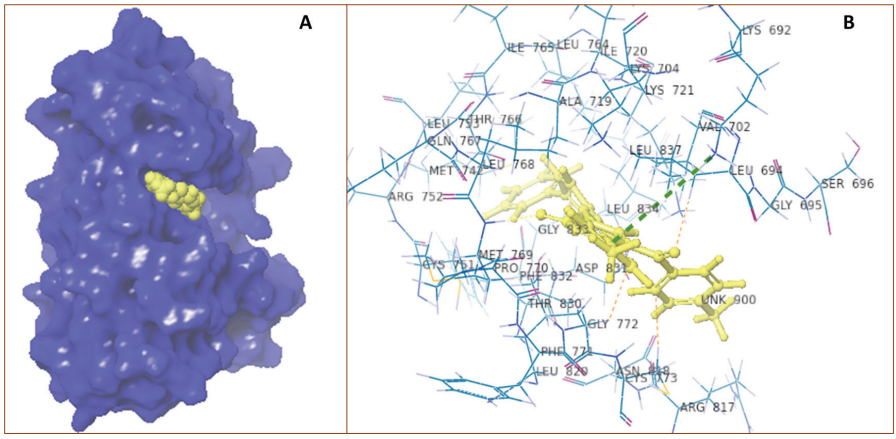

Figure 5. *(A) Molecular docked structure of Compound (2) to 4HJO crystal structure. (B) Amino acid residues at the binding site in the interaction of 4HJO and Compound (2).*

Figure 5A shows that Compound (2) is well located in the active pocket region of the EGFR crystal structure, while Figure 5B shows the amino acid residues interacting between Compound (2) and EGFR crystal structure.

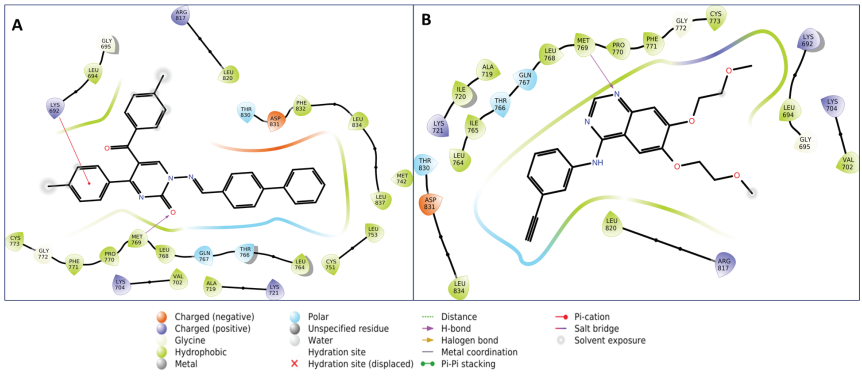

Figure 6. *(A) 2D interaction diagram of Compound (2) with 4HJO. (B) 2D interaction diagram of Erlotinib with 4HJO.*

Figure 6 shows the interaction of both Compound (2) and Erlotinib with the 4HJO crystal structure. In Figure 6A, hydrogen bond interaction with Met769, which is an important amino acid residue, as well as the presence of cation-pi interaction with Lys692 were determined. Since it was determined that Erlotinib made hydrogen bonds with Met769 in Figure 6B, it can be interpreted that it binds from the same pocket region as Compound (2).

4. CONCLUSION

As a result of these studies, a new series of pyrimidin-2(1H)-one derivative (1) was synthesized. It has been brought to the literature by using experimental and computational techniques to determine the structure of the novel Compound (2) and has the quality to lead the next studies. In addition, the synthesized Compound (2) was theoretically investigated by both DFT and molecular docking studies. Compound (2), which is comparable to Erlotinib in molecular docking results, is at a level that can lead to future studies.

Acknowledgements

This study was financially supported by Erciyes University Research Fund (FYL-2020-10303). Authors would like to thank Erzincan Binali Yıldırım University, Basic Sciences Application and Research Center (EBYU-EUTAM) for the Schrödinger Maestro 2021-2 program

REFERENCES

Ali, S. M. M., Azad, M. A. K., Jesmin, M., Ahsan, S., Rahman, M. M., Khanam, J. A., . . . Shahriar, S. M. S. (2012). In vivo anticancer activity of vanillin semicarbazone. *Asian Pacific journal of tropical biomedicine, 2*(6), 438-442.

Almeida, M. C., Resende, D. I. S. P., da Costa, P. M., Pinto, M. M. M., & Sousa, E. (2021). Tryptophan derived natural marine alkaloids and synthetic derivatives as promising antimicrobial agents. *European journal of medicinal chemistry, 209*. doi:ARTN 11294510.1016/j.ejmech.2020.112945

Aslan, H. G., Akkoc, S., & Kokbudak, Z. (2020). Anticancer activities of various new metal complexes prepared from a Schiff base on A549 cell line. *Inorganic Chemistry Communications, 111*. doi:ARTN 107645 10.1016/j.inoche.2019.107645

Bozbey, I., Uslu, H., Türkmenoğlu, B., Özdemir, Z., Karakurt, A., & Levent, S. (2022). Conventional and microwave prompted synthesis of aryl (alkyl) azole oximes, 1H-NMR spectroscopic determination of E/Z isomer ratio and HOMO-LUMO analysis. *Journal of Molecular Structure, 1251*, 132077.

Chaubey, G. S., Barcena, C., Poudyal, N., Rong, C., Gao, J., Sun, S., & Liu, J. P. (2007). Synthesis and stabilization of FeCo nanoparticles. *Journal of the American Chemical Society, 129*(23), 7214-7215.

Cimen, Z., Akkoc, S., & Kokbudak, Z. (2018). Reactions of aminopyrimidine derivatives with chloroacetyl and isophthaloyl chlorides. *Heteroatom Chemistry, 29*(4). doi:ARTN e21458 10.1002/hc.21458

David, V. B., Babu, V. H., & Reddy, V. M. (2014). Synthesis of novel 4, 6-disubstituted-2-amino pyrimidines as antibacterial agents. *Int J Pharm Chem Res, 3*(1), 2278-8700.

de Toledo, T. A., Pizani, P. S., da Silva, L. E., Teixeira, A. M. R., & Freire, P. T. C. (2015). Spectroscopy studies on Schiff base N,N ‘-bis(salicylidene)-1,2-phenylenediamine by NMR, infrared, Raman and DFT calculations. *Journal of Molecular Structure, 1097*, 106-111. doi:10.1016/j.molstruc.2015.04.038

Devim, M., Akkoc, S., Zeyrek, C. T., Aslan, H. G., & Kokbudak, Z. (2022). Design, synthesis, in vitro antiproliferative activity properties, quantum chemical and molecular docking studies of novel Schiff bases incorporating pyrimidine nucleus. *Journal of Molecular Structure, 1254*. doi:ARTN 132421 10.1016/j.molstruc.2022.132421

Frisch, M., Trucks, G. W., Schlegel, H. B., Scuseria, G. E., Robb, M. A., Cheeseman, J. R., . . . Petersson, G. (2009). Gaussian 09, revision D. 01. In: Gaussian, Inc., Wallingford CT.

Goudar, V., Rashmi, P., Shantharam, U., Kuntal, H., & Laxmivenkatesh, G. N. (2012). Synthesis of novel thienopyrimidines and evaluation for their anti-inflammatory activity. *J. Chem. Pharm. Res, 4*, 3100-3106.

Ingarsal, N., Saravanan, G., Amutha, P., & Nagarajan, S. (2007). Synthesis, in vitro antibacterial and antifungal evaluations of 2-amino-4-(1-naphthyl)-6-arylpyrimidines. *European journal of medicinal chemistry, 42*(4), 517-520. doi:10.1016/j.ejmech.2006.09.012

Jombo, G. T. A. (2011). Synthesis, Characterisation and Anti Microbial Activity of Various Schiff Base Complexes of Zinc (II) and Copper (II) Ions. *Asian Journal of Pharmaceutical and Health Sciences, 1*(1).

Kaur, N., Aggarwal, A. K., Sharma, N., & Choudhary, B. (2012). Synthesis and in-vitro antimicrobial activity of pyrimidine derivatives. *Int J Pharm Sci Drug Res, 4*(3), 199-204.

Kokbudak, Z., Saracoglu, M., Akkoc, S., Cimen, Z., Yilmazer, M. I., & Kandemirli, F. (2020). Synthesis, cytotoxic activity and quantum chemical calculations of new 7-thioxopyrazolo[1,5-f]pyrimidin-2-one derivatives. *Journal of Molecular Structure, 1202*. doi:ARTN 127261

10.1016/j.molstruc.2019.127261

KÖKbudak, Z., Aslan, H., & AkkoÇ, S. (2020). New Schiff Bases Based on 1-Aminopyrimidine-2-(1H)-one: Design, Synthesis, Characterization and Theoretical Calculations. *Heterocycles, 100*(3).

Kumar, S., Deep, A., & Narasimhan, B. (2019). A review on synthesis, anticancer and antiviral potentials of pyrimidine derivatives. *Current Bioactive Compounds, 15*(3), 289-303.

Ma, L. Y., Wang, B., Pang, L. P., Zhang, M., Wang, S. Q., Zheng, Y. C., . . . Liu, H. M. (2015). Design and synthesis of novel 1,2,3-triazole-pyrimidine-urea hybrids as potential anticancer agents. *Bioorganic & Medicinal Chemistry Letters, 25*(5), 1124-1128. doi:10.1016/j.bmcl.2014.12.087

Ngan, N. K., Lo, K. M., & Wong, C. S. R. (2011). Synthesis, structure studies and electrochemistry of molybdenum(VI) Schiff base complexes in the presence of different donor solvent molecules. *Polyhedron, 30*(17), 2922-2932. doi:10.1016/j.poly.2011.08.038

Oladipo, S. D., Yusuf, T. L., Zamisa, S. J., Shapi, M., & Ajayi, T. J. (2021). Synthesis, crystal structure, Hirshfeld surface analysis and DFT studies of N-(2,6-diisopropylphenyl)-1-(4-methoxyphenyl) methanimine. *Journal of Molecular Structure, 1241*. doi:ARTN 130620

10.1016/j.molstruc.2021.130620

Onal, Z., Ceran, H., & Sahin, E. (2008). Synthesis of Novel Dihydropyrazolo[1,5-C] Pyrimidin-7(3h)-One/-Thione Derivatives. *Heterocyclic Communications, 14*(4), 245-250. Retrieved from <Go to ISI>://WOS:000262829000005

Onal, Z., & Daylan, A. C. (2007). Reactions of 1-Amino-5-benzoyl-4-phenyl-1H-pyrimidine derivatives with various isothiocyanates. *Asian Journal of Chemistry, 19*(4), 2647-2653. Retrieved from <Go to ISI>://WOS:000251463400027

Pandey, A., Rajavel, R., Chandraker, S., & Dash, D. (2012). Synthesis of Schiff bases of 2-amino-5-aryl-1, 3, 4-thiadiazole and its analgesic, anti-inflammatory and anti-bacterial activity. *E-Journal of Chemistry, 9*(4), 2524-2531.

Park, J. H., Liu, Y. T., Lemmon, M. A., & Radhakrishnan, R. (2012). Erlotinib binds both inactive and active conformations of the EGFR tyrosine kinase domain. *Biochemical Journal, 448*, 417-423. doi:10.1042/Bj20121513

Parr, R. G., Von Szentpaly, L., & Liu, S. B. (1999). Electrophilicity index. *Journal of the American Chemical Society, 121*(9), 1922-1924. doi:DOI 10.1021/ja983494x

Sathe, B. S., Jaychandran, E., Jagtap, V. A., & Sreenivasa, G. M. (2011). Synthesis characterization and anti-inflammatory evaluation of new fluorobenzothiazole schiff's bases. *Int J Pharm Res Dev, 3*(3), 164-169.

Schiff, H. (1864). Mittheilungen aus dem Universitätslaboratorium in Pisa: eine neue Reihe organischer Basen. *Justus Liebigs Annalen der Chemie, 131*(1), 118-119.

Schrödinger Release 2021-2: Glide, S., LLC, New York, NY, 2021.

Schrödinger Release 2021-2: LigPrep, S., LLC, New York, NY, 2021.

Siddiqui, A. B., Trivedi, A. R., Kataria, V. B., & Shah, V. H. (2014). 4,5-Dihydro-1H-pyrazolo[3,4-d] pyrimidine containing phenothiazines as antitubercular agents. *Bioorganic & Medicinal Chemistry Letters, 24*(6), 1493-1495. doi:10.1016/j.bmcl.2014.02.012

Silverstein, R. M., & Bassler, G. C. (1962). Spectrometric identification of organic compounds. *Journal of Chemical Education, 39*(11), 546.

Sondhi, S. M., Singh, N., Kumar, A., Lozach, O., & Meijer, L. (2006). Synthesis, anti-inflammatory, analgesic and kinase (CDK-1, CDK-5 and GSK-3) inhibition activity evaluation of benzimidazole/benzoxazole derivatives and some Schiff's bases. *Bioorganic & Medicinal Chemistry, 14*(11), 3758-3765.

Turan, N., Bingol, M., Savci, A., Kocpinar, E. F., & Colak, N. (2021). Synthesis, structural studies and antioxidant activities of M(II) complexes with NOS donor schiff base ligand. *Sigma Journal of Engineering and Natural Sciences-Sigma Muhendislik Ve Fen Bilimleri Dergisi, 39*(3), 279-289. doi:10.14744/sigma.2021.00017

Wei, D. Y., Li, N., Lu, G., & Yao, K. M. (2006). Synthesis, catalytic and biological activity of novel dinuclear copper complex with Schiff base. *Science in China Series B-Chemistry, 49*(3), 225-229. doi:10.1007/s11426-006-0225-8

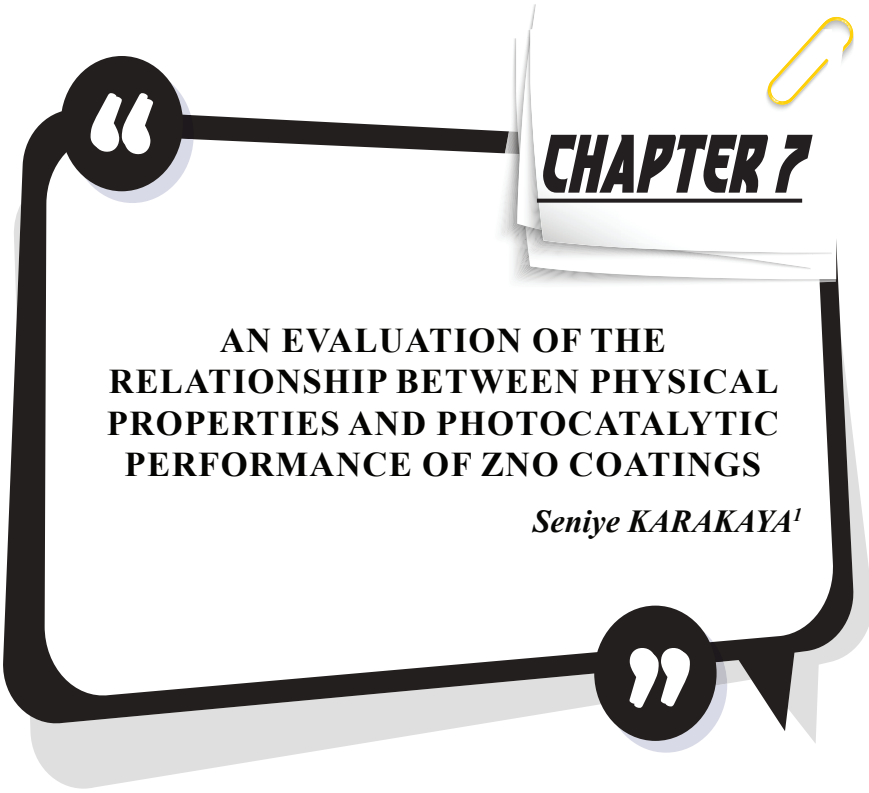

CHAPTER 7

AN EVALUATION OF THE RELATIONSHIP BETWEEN PHYSICAL PROPERTIES AND PHOTOCATALYTIC PERFORMANCE OF ZNO COATINGS

Seniye KARAKAYA[1]

1 Eskisehir Osmangazi University, Faculty of Science and Letters, Department of Physics 26040 Eskisehir, Turkey

Corresponding author. Tel.: +90 222 239 3750; fax: +90 222 239 3578.

E-mail address: seniyek@ogu.edu.tr (S. Karakaya).

Orcid ID: 0000-0003-2658-9282

1. Introduction

ZnO is a semiconductor with a wide direct band gap (E_g ~3.34 eV) and a relatively high exciton binding energy of 60 meV at room temperature [1]. Owing to its unique properties, ZnO has been considered as a potential material for wide range of applications including field effect transistors [2], UV detectors [3, 4], gas sensors [5], dye sensitized solar cells [6, 7, 8], biomedical applications [9, 10], photocatalysis [11-13].

ZnO films have been widely studied in recent years because of its low cost, environmentally friendly nature and being a promising photocatalytic material that provides significant advantages compared to commonly used TiO_2. Especially in the last few years, as global warming and environmental problems are alarming, research on green technologies such as the production and application of photocatalysts has attracted attention. One of these research areas is semiconductor photocatalysts using environmentally safe semiconductor metal oxide materials [14]. Among these materials, TiO_2, SnO_2, Fe_2O_3 and ZnO are frequently used in photocatalytic applications due to their wide optical band gap and suitable optical absorption energies [15-18]. Compared to popular TiO_2, ZnO has two important advantages: (i) it may absorb more light in the UV spectrum and (ii) it is cost-effective than TiO_2 [19]. ZnO was also reported to exhibit higher quantum efficiency and photocatalytic activity than TiO_2 in certain cases [20, 21]. It is also well known that ZnO exhibits the richest range of morphologies among the wide band gap semiconductors [14]. So many research studies on ZnO photocatalysts have been focusing on developments of ZnO nanoparticles to achieve high surface area and hence more superior photocatalytic activity.

ZnO is a matchless material that can be deposited in several forms of nanostructures such as rods, wires, flowers, spheres, tubes and pyramids with extraordinary physical properties by using appropriate physical or chemical techniques [22-24]. ZnO films have been prepared by a variety of methods such as chemical vapor deposition [25], sputtering [26], sol–gel dip-coating [27] and sol–gel spin-coating [28]. One of these techniques, the low-cost sol–gel process is on the vanguard in both research and industrial production owing to its unique application facilities enabling (i) homogeneous film at the molecular level (ii) excellent control of the film composition (iii) low crystallization temperature (iv) easy control of the film thickness by changing the number of spinning cycle [29]. ZnO photocatalysts have been studied using various organic pollutants [30-37].

There are a great number of study and reports attached to the effect of sol-gel parameters during sol preparation such as pH, molarity, temperature etc. [38-40]. However, there are limited number of reports related to the

effect of spinning cycle on the photocatalytic properties of sol-gel spin coated ZnO films [41-44]. In the present work, ZnO films were prepared by sol–gel spin-coating method. Structural, optical and surface properties have been examined in detail to analyze and optimize the quality of ZnO films produced with different spinning cycles. Aim of this study is to reveal and interpret the relationship between these parameters and photocatalytic test results efficiently.

2. Experimental details

2.1. Sol preparation and deposition of ZnO films

ZnO films were synthesized by sol-gel spin coating technique onto glass substrates using zinc acetate dihydrate [$Zn(CH_3COO)_2 2H_2O$]. The precursor solution (0.5 M) was prepared by dissolving required amount of zinc acetate (99.99%, Merck) in a mixture of 2-methoxyethanol ($C_3H_8O_2$, ACROS, %99) and mono-ethanolamine (C_2H_7NO, ALDRICH, %99.5) and stirred at 60 °C for 90 min, leading to the formation of a clear and homogeneous solution. Transparent sol that served as the coating solution after being kept for 24h at room temperature was used for film preparation. A solution of chromic acid and deionized water was used for cleaning process for 30 min and then the substrates exposed to second cleaning in acetone and deionized water at 60 °C for 15 min. After dropping the sol onto glass substrate, coating was performed using a spin coater at room temperature for periods of 30s, gradually increasing the spin rate to 4000 rpm. This process was repeated for different spinning cycles and each layer was dried at 200 °C for 10 min which led to the formation of films. To achieve complete crystallization of films ZnO films were annealed at 500°C during 1 h. The samples were named with respect to corresponding spinning cycle as Z4, Z5 and Z6. The sol-gel route for the synthesis of the ZnO films is shown in Fig. 1.

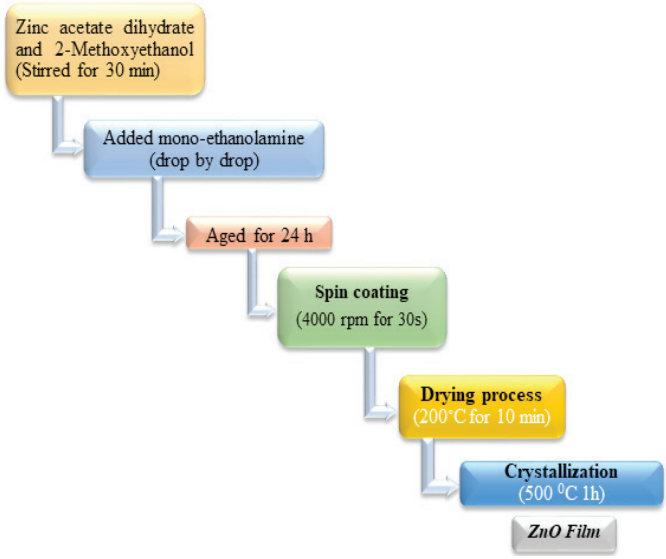

Fig. 1. *Flowchart used in the preparation of ZnO films.*

2.2. Characterization of ZnO films

In this study, the optical, structural, surface and photocatalytic properties of ZnO films were analyzed in detail to examine the effect of spinning cycle. The crystalline structure of the films was analyzed using an X-ray diffractometer (XRD, Bruker-Advance D8) utilizing CuK_{α} radiation (λ=1.5405 Å) by step of 0.02° s^{-1}. Park Systems XE-100 AFM was used to obtain surface images and roughness values. AFM measurements were taken in non-contact mode with 1 Hz scan rate in air enviroment at room temperature. In addition, FESEM measurements were performed for the determination of surface morphology by a Hitachi Regulus 8230 Field Emission Scanning Electron Microscope. Absorption spectra of the films were taken in the wavelength range of 300–900 nm by Shimadzu UV-2550 UV–Vis spectrophotometer and optical band gap values were calculated using the optical method. Perkin Elmer LS 55 Fluorescence Spectrometer was used to obtain photoluminescence spectra (310 nm excitation wavelength). Thickness values of the samples Z4, Z5 and Z6 were obtained as 180, 193 and 225 nm, respectively.

2.3 *Photocatalytic tests of ZnO films*

Photocatalytic degradation tests of the methylene blue ($C_{16}H_{18}ClN_3S$) organic pollutants were accomplished by using the ultraviolet lamp (UVA, PHILIPS 9W) as the source of illumination. The characteristic maximum absorption band of the methylene blue was observed at 664 nm in absorbance spectra taken in the wavelength range of 400-800 nm.

Linear equation of *A= 0.237C-0.011* was obtained after the analysis of these curves. The methylene blue solution with concentration of 2 mg.L^{-1} was used in photocatalytic tests. Schematic diagram of the experimental set-up utilized to perform the photocatalytic tests is presented in Fig. 2. ZnO films were placed 10 cm away from the UV lamp at a horizontal position in a beaker glass containing 15 ml of aqueous solution to perform photocatalytic tests. The solution containing the film was stirred for 30 min in the dark medium and the absorbance spectra was obtained. Then absorption measurements were performed for the solutions processed under UV light in 60 min steps up to 240 min. Percentage degradation values and kinetic rate constants were calculated using the test results.

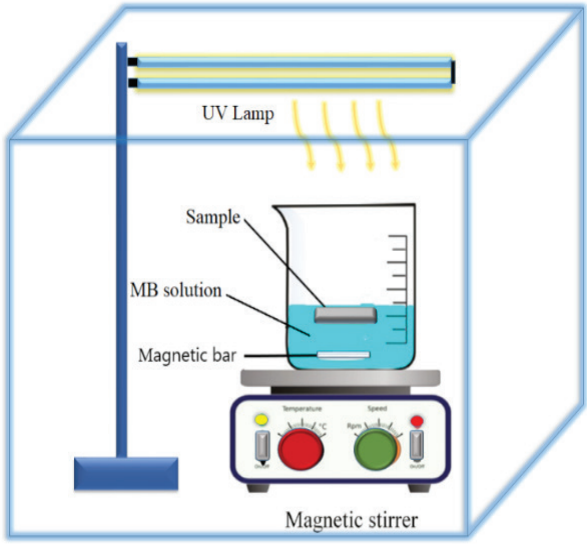

Fig. 2. *Set-up used for photocatalytic tests.*

3. Results and discussion

3.1. Structural properties of ZnO films

Fig. 3 presents the XRD pattern of ZnO films with diffraction peaks belonging to wurtzite hexagonal structure (JCPDS card no: *04-008-8196*). There are primarily three XRD peaks corresponding to the crystal planes of (100), (002) and (101). It was determined that all films were polycrystalline and *c*-axis oriented including two weak peaks through (100) and (101) planes. XRD patterns clearly showed that increasing spinning cycle caused ZnO films to show a more dominant growth along the (002) plane. The intensity of this peak increased gradually with the increase of the spinning cycle which indicates an improvement in the crystallization level.

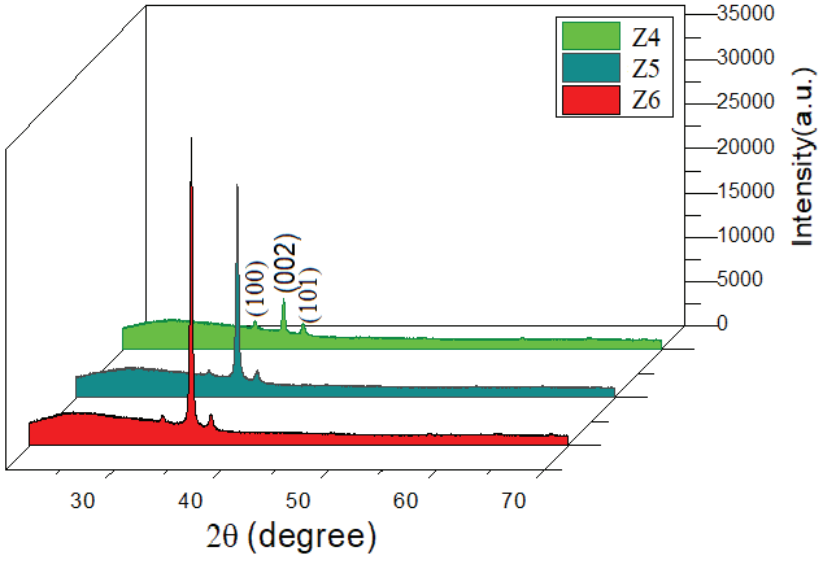

Fig. 3. *XRD patterns of ZnO films.*

In order to examine the possible effect of this change on photocatalytic performance, $I_{(002)}/[I_{(100)}+I_{(101)}]$ ratios were calculated using the absolute values of corresponding peaks to see the effectiveness of the (002) peak in each sample relative to others. Also, structural parameters such as grain size and macrostrain were calculated to make this discussion comprehensive. The grain size and macrostrain values were calculated using equations given below [45,46].

$$D = \frac{0.9\lambda}{\beta \cos\theta} \tag{1}$$

$$< e >= \frac{d-d_0}{d_0} \tag{2}$$

where D is the grain size, β is the full width at half maximum (FWHM), λ is the wavelength of X-ray beam ($\lambda_{CuK\alpha}$ = 1.5406 Å), d_0 is the interplanar distance without deformation and d is the interplanar distance for each sample. All parameters are presented in Table 1. It is clear from Table 1 that there is not a dramatic alteration with increasing spinning cycle neither in grain size nor in macrostrain values. However, when the peak intensity ratios are examined, it is clear that there is an important changing depending on the spinning cycle. Especially, sample

Z6 stands out among others, as the increase in peak intensities represents an improvement in the crystallinity level. This behavior is important in view of photocatalytic applications and sample Z6 has a high potential for these type of applications as it contains less number of defect states which may behave as recombination centers for photo-generated electrons and holes.

Table 1. *Grain size (D), macrostrain (<e>) and ($I_{(002)}/[I_{(100)}+I_{(101)}]$) values for ZnO films.*

Sample	D (nm)	$<e>\times10^{-3}$	$(I_{(002)}/[I_{(100)}+I_{(101)}])$
Z4	93.1	10.7	1.97
Z5	91.4	11.4	14.86
Z6	95.2	12.5	15.18

3.2. Surface properties of ZnO films

Surface morphology of coatings play a significant role in photocatalytic applications. Especially, surface roughness and texture are properties that worth to analyze as they play an important role on the light-triggered interactions between the organic contaminants and photocatalyst surface. AFM measurements were carried out to observe the possible effects of spinning cycle on the surface morphology of the films. AFM images taken from a scanning area of 10 μm×10 μm were also used for determining the surface roughness values of the films. Results are shown in Fig. 4 and Table 2. All samples show homogeneous morphologies with the wrinkles located on the surface. Although sample Z4 has some voids and low number of wrinkles on the surface, samples without voids and having closely packed wrinkles could be obtained by increasing the spinning cycle to 5 and 6. When AFM images of samples Z5 and Z6 compared, the increase in the width of the wrinkles is also noticeable. The change of shape, size and width of the wrinkles shows that it is possible to modify the surface of sol-gel derived ZnO films by changing the spinning cycle. Besides, 3D AFM images show that sample Z6 has rounded and particle like formations resembling spherical symmetry when compared to others. Table 2 shows that there is not a noticeable change in the rms and average roughness values of the films. However, it was previously reported photocatalytic activity is closely related to roughness [37].

For high roughness values, samples Z5 and Z6 may be potential candidates for photocatalytic applications with their increased peak-valley roughness values.

Table 2. *Peak-valley (R_{pv}), rms (R_{rms}) and average (R_a) roughness values for ZnO films.*

Sample	R_{pv} (nm)	R_q (nm)	R_a (nm)
Z4	38	3	2
Z5	45	4	3
Z6	56	5	4

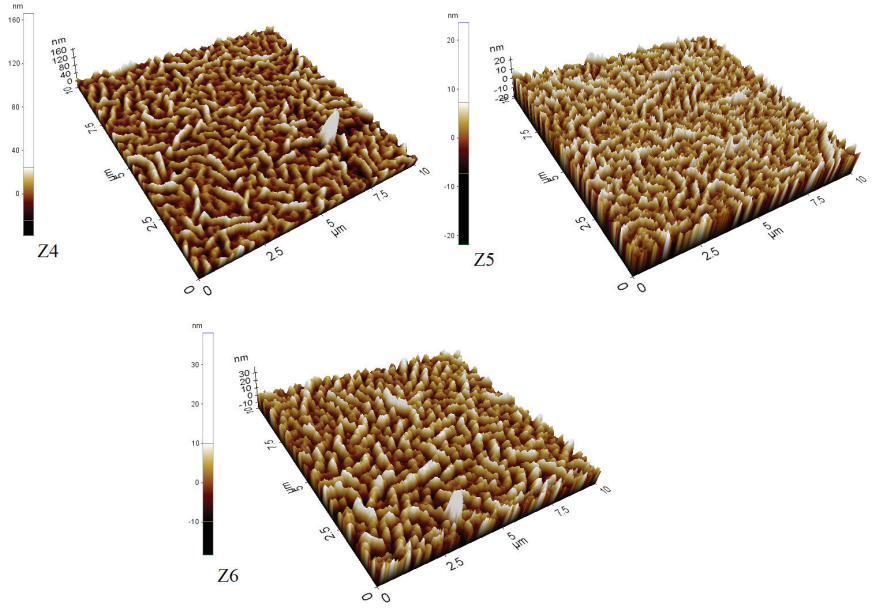

Fig.4. *AFM images of ZnO films*

FESEM measurements were also performed to identify the particle size distribution and morphology of synthesized ZnO films. When FESEM images presented in Fig. 5 are examined, the wrinkle formations draw attention, as in the AFM micrographs. However, it is seen that the wrinkles become more distinct indicating a tighter junction with increasing spinning cycle.

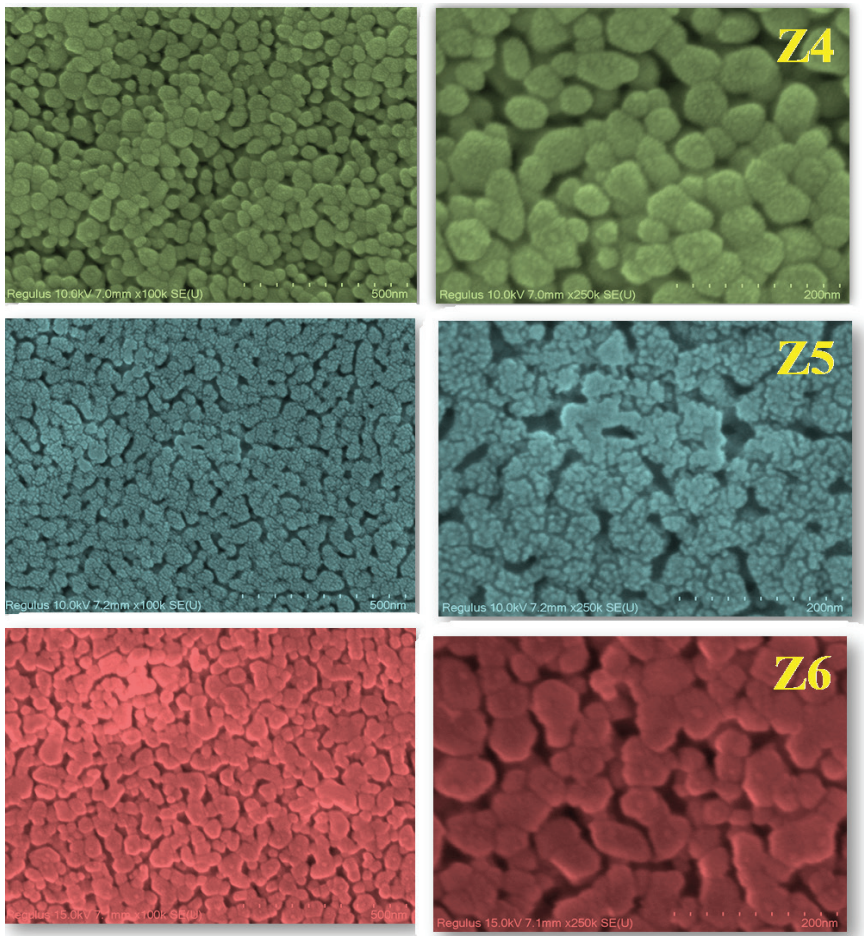

Fig. 5. *FESEM images of ZnO films.*

3.3. Optical band gap values of ZnO films

The optical band gap values were calculated by the following relation [47].

$$(\alpha h\nu) = A\,(h\nu - E_g)^n \qquad (3)$$

where A is a constant that depends on refractive index of the material, E_g is the optical band gap, $h\nu$ is the photon energy. n determines the type of transition in the band gap that is an exponent index. The optical band gap was determined by $(\alpha h\nu)^2$ vs. $(h\nu)$ plots (Fig 6) and were found to be 3.27 eV, 3.27 eV and 3.28 eV for the films produced by spinning cycles of 4, 5 and 6, respectively.

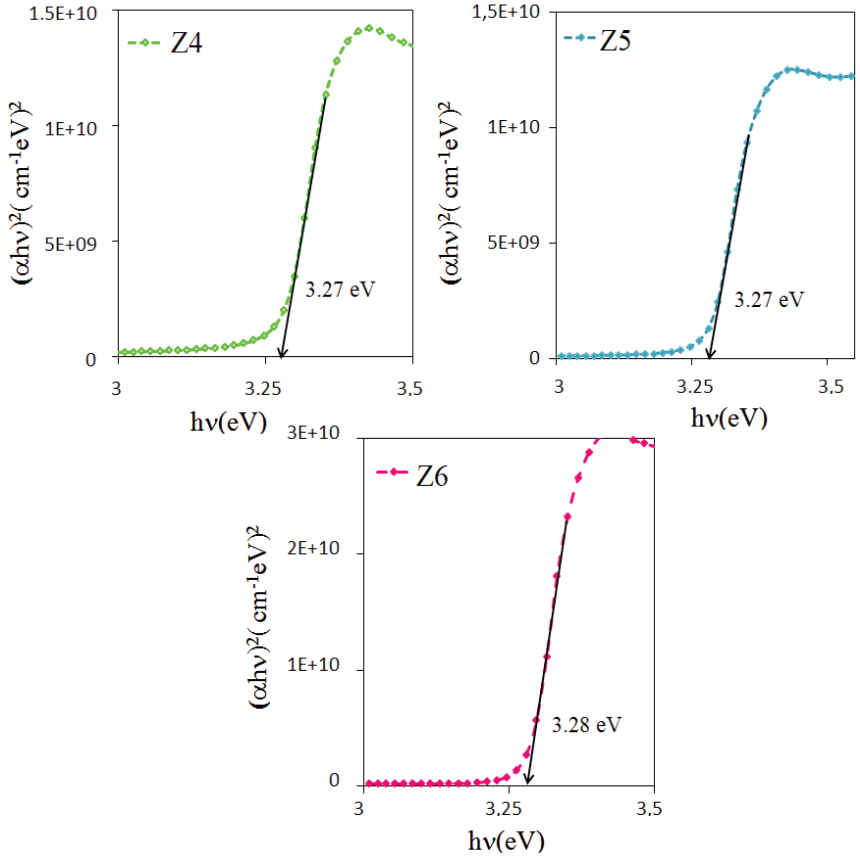

Fig. 6. *Plots used for band gap determination.*

3.4. Photoluminescence properties of ZnO films

Photoluminescence (PL) properties measurements were performed to reveal a possible relationship between traps and photocatalytic activity. Fig. 7 (a) shows the PL spectra of ZnO films obtained.

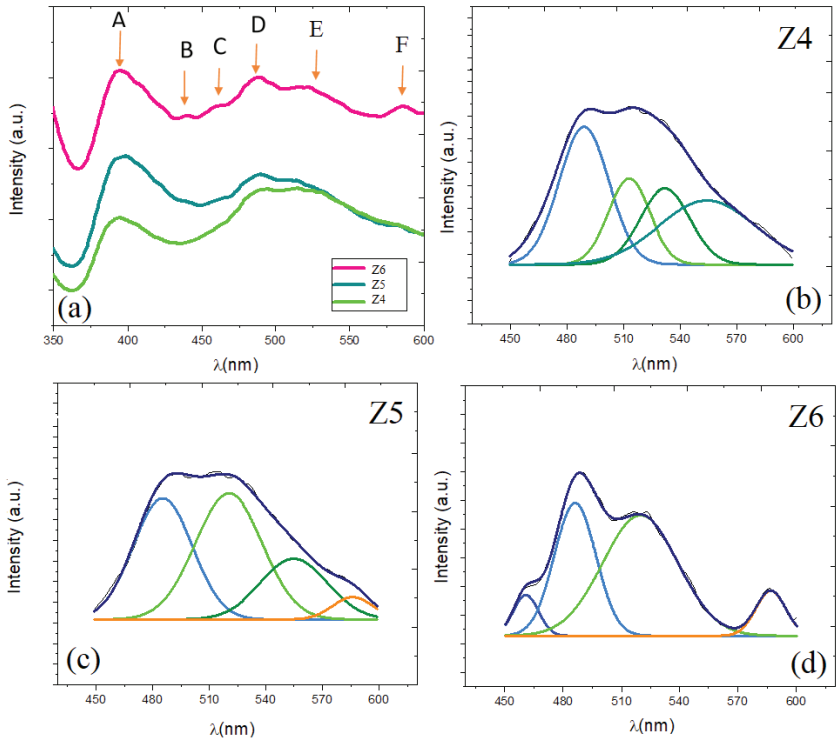

Fig. 7. *Photoluminescence spectra* **(a)** *and multi-peak Gaussian curve fitting for* **(b)** *Z4* **(c)** *Z5 and* **(d)** *Z6.*

PL spectrum can be divided into two regions: the luminescence corresponding to the near band emission (NBE) and emissions related to deep level transitions. It is clear that the intensity of UV emission peak (A in figure) at 394 nm (3.15 eV) which is assigned to the NBE of ZnO [48, 49] increases with spinning cycle. This may be the result of improvement in crystallinity for high spinning cycles as confirmed by XRD patterns. In addition, the sample obtained at 6 spinning cycle contains an extra emission peak (B in the figure) at 440 nm (2.82 eV). This peak is generally assigned to the transitions from extended levels of zinc interstitials to valance band [50].

Emissions related to deep level transitions in PL spectra (C to F in the figure) shows themselves as a broad band composed of possible sub-peaks. So, multi-peak Gaussian curve fitting method was performed to analyze the deep trap levels in optical band gap, as shown in Fig. 7 (b, c and d). In this region, the blue emissions at 489-494 nm (2.54 eV-2.51 eV) are ascribed to the transitions from Zn_i levels to zinc vacancies (V_{Zn}) [50]. The green emissions centered at 519-521 nm (2.39-2.38 eV) are attributed to the

recombination of trapped electrons at singly ionized oxygen vacancy (V_O^+) with photogenerated holes. Another green emission peak at 532 nm (2.33 eV) for sample Z4 represents the transitions related to oxygen vacancies [51]. Samples Z5 and Z6 also show green emission peaks at 554 nm (2.24 eV) and 555 nm (2.23 eV). An interesting result emerges when the green emissions of the films are examined. It was evaluated that the distribution of the traps representing green emission in ZnO films in the band gap recovered with the increasing number of spinning cycle and the effect of green emissions decreased making blue emissions dominant. Another indicator of the strengthening of blue emission by the increase of spinning cycle is the emission peak which appears only for sample Z6. This peak is at 460 nm (2.70 eV) and corresponds to the transitions from V_O levels to valance band [50]. Another point that takes attention in PL analyzes is the yellow emission peaks that occur in high spinning cycles. The yellow emission peaks centered at 587 nm (2.11 eV) and 586 nm (2.12 eV) for samples Z5 and Z6 are attributed to the transitions related to point defects such as oxygen vacancies [52].

3.5. Photocatalytic properties of ZnO films

Photocatalytic mechanism of ZnO is given in other studies [53, 54]. Depending on the reaction conditions, superoxide ions ($O_2^{\cdot-}$), hydroxyl radicals ($OH^{\cdot}$), hydrogen peroxide (H_2O_2) and O_2 perform an efficient role in photocatalytic reactions.

Fig. 8 presents absorbance spectra taken during photocatalytic tests. Percent degradation values of methylene blue for each ZnO film were calculated with the equation expressed in [55]. The time-dependent $ln(C_0/C)$ graphs given in Fig. 9 shows that photocatalytic degradation obeys first order law of velocity. To evaluate the kinetics of photocatalytic activity, photocatalytic rate constants (k) were determined. Photocatalytic rate constant and percent degradation values are given in Table 3.

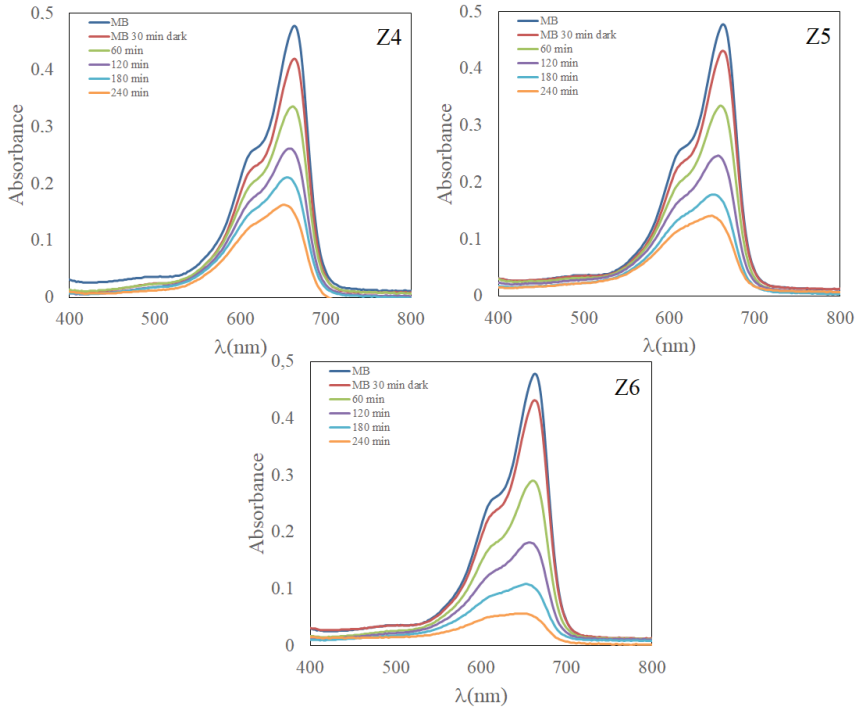

Fig. 8. *The time-dependent absorbance spectra of the methylene blue solution for ZnO films.*

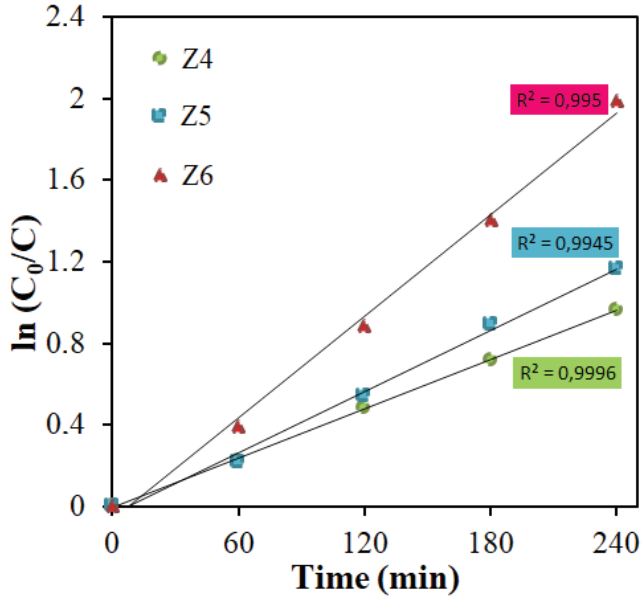

Fig. 9. *Time-dependent ln(C_0/C) plots of the methylene blue solution for ZnO films.*

Table 3. *Photocatalytic rate constants and percent degradation values for ZnO films.*

Sample	Photocatalytic rate constant (k) (min^{-1})	% Degradation
Z4	$4.10x10^{-3}$	66.46
Z5	$5.34x10^{-3}$	72.59
Z6	$8.83x10^{-3}$	87.93

Decreased absorbance values in Fig. 8 shows that ZnO films obtained in this study played an active role as a photocatalyst in the degradation of methylene blue. As can be seen from Table 3, sample Z6 attracts attention with the highest % degradation value and photocatalytic rate constant among others. This refers an increased photocatalytic activity with increasing cycle. As discussed in AFM analysis, there are spherical formations in 3D AFM images of sample Z6 which refer an increased surface area. This creates a positive effect on photocatalytic performance and makes the surface of sample Z6 suitable for the efficient adsorption of the dye. Similar results were obtained by others [56, 57]. In addition, structural defects have an important role on the photocatalytic activity since they behave as recombination centers for photoinduced electrons and holes [58]. Based on this, sample Z6, having high crystallization level as proved by XRD studies, contains lower number of such defects causing increased photocatalytic activity. In view of PL analyzes, this sample has an extra emission peak which was assigned to transitions from V_O sites to valance band. Such defects enable better separation of charges resulting an increase in photocatalytic activity[59].

4. Conclusion

In this work, photocatalytic performance of sol-gel derived ZnO films have been tried to be optimized by changing the spinning cycle. To evaluate the effect of physical parameters on photocatalytic performance optical, surface and structural properties were investigated. Structural analysis showed that increase in spinning cycle causes ZnO films to have increased crystallinity levels with dramatic increase in (002) peak intensities. This behavior is important in view of photocatalytic applications and sample Z6 has a high potential for these type of applications as it contains less number of defect states which may behave as recombination centers. Also, the effect of other structural parameters on photocatalytic performance was evaluated and it was concluded that an effective growth in (002) direction plays a greater role than grain size or macrostrain values. Surface analysis by AFM refers that samples Z5 and Z6 may be potential candidates for photocatalytic applications with their increased peak-valley roughness values. Also, when the spinning cycle increased to 6, spherical

formations were obtained on the surface of sample Z6. This makes the surface of this sample convenient for the effective adsorption of the dye and increases the photocatalytic performance. PL analysis showed that the increase in spinning cycle caused the distribution of the traps related to green emission recovered and decreased, making blue emissions dominant for ZnO films. Also, sample Z6 has an extra emission peak which was assigned to transitions from V_O sites to valance band. As a result of these outputs, increase in defects related to blue emissions causes retardation of electron-hole recombination which in turn makes ZnO films to represent improved photocatalytic performance.

Acknowledgments

This study was supported by the Scientific Research Projects Coordination Unit of Eskisehir Osmangazi University within the scope of the project numbered 201819065.

Author is thankful to Prof. Dr. Ferhunde ATAY and Prof. Dr. İdris AKYÜZ for providing the analysis and conceptualization opportunities.

REFERENCES

[1] T. Saidani, M. Zaabat, M.S. Aida, B. Boudine, Effect of copper doping on the photocatalytic activity of ZnO thin films prepared by sol-gel method, Superlattices Microstruct. 88 (2015) 315-322.

[2] S. Ju, K. Lee, M.H. Yoon, A. Facchetti, T.J. Marks, D.B. Janes, High performance field-effect transistors fabricated with laterally grown ZnO nanorods insolution, Nanotechnology 22 (2011) 185310.

[3] Y. Shimura, S. A. Srinivasan, R. Loo, Microwave assisted synthesis of ZnO nano-sheets and their application in UV-detector, ECS J. Solid State Sci. Technol. 1 (2012) 140–143.

[4] P.P. Murmu, J. Kennedy, G. V. M. Williams, B.J. Ruck, S. Granville, S.V. Chong, Observation of magnetism, low resistivity, and magnetoresistance in the near-surface region of Gd implanted ZnO, Appl. Phys. Lett. 101 (8) (2012) 082408.

[5] H. Xu, X. Liu, D. Cui, M. Li, M. Jiang, A novel method for improving the performance of ZnO gas sensors, Sensors Actuators B Chem. 114 (2006) 301–307.

[6] S.H. Ko, D. Lee, H. Wook Kang, K.H. Nam, J.Y. Yeo, S.J. Hong, C.P. Grigoropoulos, H.J. Sung, Nanoforest of hydrothermally grown hierarchical ZnO nanowires for a high efficiency dye-sensitized solar cell, Nano Lett. 11 (2011) 666–671.

[7] V. Kumar, N. Singh, V. Kumar, L.P. Purohit, A. Kapoor, O.M. Ntwaeaborwa, H.C. Swart, Doped zinc oxide window layers for dye sensitized solar cells, J. Appl. Phys. 114 (2013) 134506.

[8] A. Farrag, M. R. Balboul, Nano ZnO thin films synthesis by sol–gel spin coating method as a transparent layer for solar cell applications, J Sol-Gel Sci Technol. 82 (2017) 269–279.

[9] D. Chu, Y. Masuda, T. Ohji, K. Kato, Formation and photocatalytic application of ZnO nanotubes using aqueous solution, Langmuir. 26 (2009) 2811–2815.

[10] P.P. Murmu, J. Kennedy, B.J. Ruck, S. Rubanov, Microstructural, electrical and magnetic properties of erbium doped zinc oxide single crystals, Electron. Mater. Lett. 11 (6) (2015) 998–1002.

[11] J.B. Shim, H. Chang, S. Kim, Rapid hydrothermal synthesis of zinc oxide nanowires by annealing methods on seed layers, J. Nanomater. 6 (2011) 582764.

[12] Z.R. Tian, J.A. Voigt, J. Liu, B. McKenzie, M.J. McDermott, M.A. Rodriguez, H. Konishi, H. Xu, Complex and oriented ZnO nanostructures, Nat. Mater. 2 (2003) 821–826.

[13] K. Kaviyarasu, C. Maria Magdalane, K. Kanimozhi et al., Elucidation of photocatalysis, photoluminescence and antibacterial studies of ZnO thin films by spin coating method, J. Photochem. Photobiol. B: Biology. 173 (2017) 466–475.

[14] N. Talebian, M. R. Nilforoushan, N. Maleki, Ultraviolet to visible-light range photocatalytic activity of ZnO films prepared using sol–gel method: The influence of solvent, Thin Solid Films. 527 (2013) 50–58.

[15] I. Dundar, M. Krichevskaya, A. Katerski, IO. Acik, TiO2 thin films by ultrasonic spray pyrolysis as photocatalytic material for air purification. R. Soc. Open Sci. 6 (2019) 181578.

[16] N. Talebiann, F. Jafarinezhad, Morphology-controlled synthesis of SnO2 nanostructures using hydrothermal method and their photocatalytic applications, Ceramics International 39 (2013) 8311–8317.

[17] M. Mishra, D.Chun, _□-Fe2O3 as a photocatalytic material: A review, Applied Catalysis A: General 498 (2015) 126–141.

[18] N. Kaneva, I. Stambolova, V. Blaskov et al., A comparative study on the photocatalytic efficiency of ZnO thin films prepared by spray pyrolysis and sol–gel method, Surf. Coat. Tech. 207 (2012) 5–10.

[19] N. Boussatha, M. Gilliot, H. Ghoualem, J. Martin, Formation of nanogranular ZnO ultrathin films and estimation of their performance for photocatalytic degradation of amoxicillin antibiotic, Mater. Res. Bull. 99 (2018) 485–490.

[20] S. K. Kansal, M. Singh, D. Sud, Studies on photodegradation of two commercial dyes in aqueous phase using different photocatalysts, J. Hazard. Mater. 141 (2007) 581.

[21] N. Sobana, M. Swaminathan, The effect of operational parameters on the photocatalytic degradation of acid red 18 by ZnO, Sep. Purif. Technol. 56 (2007) 101.

[22] G. Yi, C. Wang, W. Park II, ZnO nanorods: synthesis, characterization and applications, Semicond. Sci. Technol. 20 (2005) 22–34.

[23] J. Cui, Zinc oxide nanowires, Mater. Charact. 64 (2011) 43–52.

[24] V. K. Jayaraman, A. Hernández-Gordillo, M. Bizarro, Importance of precursor type in fabricating ZnO thin films for photocatalytic applications, Mater. Sci. Semicond. Proces. 75 (2018) 36–42.

[25] K. Haga, M. Kamidaira, Y. Kashiwaba, T. Sekiguchi, H. Watanabe, ZnO thin films prepared by remote plasma-enhanced CVD method, J. Cry. Growth 214–215 (2000) 77–78.

[26] V. Tvarozek, I. Novotny, P. Sutta, S. Flickyngerova, K. Schtereva, E. Vavrinsky, Influence of sputtering parameters on crystalline structure of ZnO thin films, Thin Solid Films 515 (2007) 8756–8760.

[27] S. Aydemir, S. Karakaya, The effect of Al on structure, morphology and optical properties of network texture ZnO thin films synthesized using the sol–gel method, Optik. 126 (18) (2015) 1735-1739.

[28] G. Demircan, E.F. Gurses, A. Acikgoz, S. Yalcin, B. Aktas, Effects of spin coating parameters on stress, electrical and optical properties of multilayer ZnO thin film prepared by sol–gel, Mol. Cryst. Liq. Cryst., 709:1 (2021) 61-69.

[29] A. R. Nimbalkara, M.G. Patil, Synthesis of ZnO thin film by sol-gel spin coating technique for H2S gas sensing application, Physica B 527 (2017) 7–15.

[30] R. Darvishi, C. Soltani, A. Rezaee, M. Safari, Photocatalytic degradation of formaldehyde in aqueous solution using ZnO nanoparticles immobilized on glass plates, Desalin Water Treat. 53 (2013) 1–8.

[31] H. Wang, S. Dong, Y. Chang, X. Zhou, X. Hu, S. A. M. Lima, Microstructures and photocatalytic properties of porous ZnO films synthesized by chemical bath deposition method, Appl. Surf. Sci. 258 (2012) 4288–4293.

[32] V.N. Blaskov, I.D. Stambolova, S.V. Vassilev, C.D. Dushkin, Photocatalytic degradation of malachite green by zinc oxide sprayed films, Bulg. Chem. Commun. 45- 2 (2013) 263–267.

[33] A. Boughelout, R. Macaluso, M. Kechouane, M. Trari, Photocatalysis of rhodamine B and methyl orange degradation under solar light on ZnO and Cu_2O thin films, React. Kinet. Mech. Catal. 129 (2020) 1115–1130.

[34] Y. Zandsalimi, P. Teymouri, R. D. C. Soltani, R. Rezaee, N. Abdullahi, M. Safari, Photocatalytic removal of Acid Red 88 dye using zinc oxide nanoparticles fixed on glass plates. J Adv. Environ. Health. Res. 3(2) (2015).

[35] S.M. Hosseini, I. A. Sarsari, P. Kameli, H. Salamati, Effect of Ag doping on structural, optical, and photocatalytic properties of ZnO nanoparticles, J. Alloys Compd. 640 (2015) 408–415.

[36] S. Shankar, M. Saroja, M. Venkatachalam, M. Kutraleeswaran, Photocatalytic degradation of methylene blue dye using ZnO thin films, Effect of Area of Catalyst, IJRAR 6(2) (2019) 2348-1269.

[37] P. Jongnavakit, P. Amornpitoksuk, S. Suwanboon, T. Ratan, Surface and photocatalytic properties of ZnO thin film prepared by sol–gel method, Thin Solid Films. 520 (2012) 5561–5567.

[38] K. Meziane, A. El Hichou, A. El Hamidi, M. Mansori, A. Liba, A. Almaggoussi, On the sol pH and the structural, optical and electrical properties of ZnO thin films, Superlattices and Microstructures 93 (2016) 297-302.

[39] U. Chaitra, D. Kekuda, K. M. Rao, Dependence of solution molarity on structural, optical and electrical properties of spin coated ZnO thin films, J Mater Sci: Mater Electron 27 (2016) 7614–762.

[40] U. Chaitra, D. Kekuda, K. M. Rao, Effect of annealing temperature on the evolution of structural, microstructural, and optical properties of spin coated ZnO thin films, Ceramics International 43 (2017) 7115–7122.

[41] M. Toubane, R. Tala-Ighil, F. Bensouici, M. Bououdina, W. Cai, S. Liu, M. Souier, A. Iratni, Structural, optical and photocatalytic properties of ZnO nanorods: Effect of aging time and number of layers, Ceram. Int. 42 (2016) 9673–9685.

[42] M.I. Khan, K.A. Bhatti et al., Characterizations of multilayer ZnO thin films deposited by sol-gel spin coating technique, Results Phys. 7 (2017) 651–655.

[43] S. Alavi, H. Bazrafshan, M. Nikazar, An investigation into the simultaneous influence of withdrawal speed and number of coated layers on photocatalytic activity of ZnO thin films, J Sol-Gel Sci Technol. 81 (2017) 652–661.

[44] F. Atay, O. Gultepe, The effect of spinning cycle on structural, optical, surface and photocatalytic properties of sol–gel derived ZnO films, J Sol-Gel Sci Technol. (2021) 100:299–309.

[45] N.F. Mott, E.A. Davis, Electronic Processes in Non-Crystalline Materials, 2nd ed., Clarendon Press/Oxford University Press, Oxford/New York, 1979.

[46] F. Atay, I. Akyuz, D. Durmaz, S. Kose, Characterization of ZnO-SnO_2 oxide systems produced by ultrasonic spray pyrolysis, Sol. Energy. 193 (2019) 666–675.

[47] J. I. Pankove, Optical Processes in Semiconductors, Prentice-Hall, Englewood Cliffs, NJ, USA, 1971.

[48] L. Ouarez, A. Chelouche, T. Touam, Au-doped ZnO sol-gel thin films: An experimental investigation on physical and photoluminescence properties, J. Lumin. 203 (2018) 222–229.

[49] D. Das, P. Mondal, Photoluminescence phenomena prevailing in c-axis oriented intrinsic ZnO thin films prepared by RF magnetron sputtering, RSC Adv. 4 (2014) 35735.

[50] X. Chen, X. Qingshuang, L. Jitao, Significantly improved photoluminescence properties of ZnO thin films by lithium doping, Ceram. Int. 46 (2020) 2309–2316.

[51] H. Qian, L. Xu, F. Xian, Jing Su, X. Luo, Accelerating the formation of high-quality optical surface layer in ZnO thin films by the increase of heat-treatment temperature, Optik. 232 (2021) 166527.

[52] D. Yu, R. Cai, Z. Liu, Studies on the photodegradation of Rhodamine dyes on nanometer-sized zinc oxide, Spectrochim. Acta, Part A. 60 (2004) 1617.

[53] M.A. Behnajady, N. Modirshahla, R. Hamzavi, Kinetic study on photocatalytic degradation of C.I. Acid Yellow 23 by ZnO photocatalyst, J. Hazard. Mater. 133 (2006) 226.

[54] A. Ajmal, I. Majeed, R. N. Malik, H. Idriss, M. A. Nadeem, Principles and mechanisms of photocatalytic dye degradation on TiO_2 based photocatalysts: A comparative overview, RSC Adv. 4 (2014) 37003-37026.

[55] F. Bensouici, T. Souier, A. Iratni, A. Dakhel, R. Tala-Ighil, M. Bououdina, Effect of acid nature in the starting solution on surface and photocatalytic properties of TiO_2 thin films, Surf. Coat. Technol. 251 (2014) 170–176.

[56] K. Eufinger, D. Poelman, H. Poelman, R. De Gryse, G.B. Marin, TiO_2 Thin Films for Photocatalytic Applications, Thin Solid Films: Process and Applications. 314-4 (2008) 189-227.

[57] L. B. Xiong, J. L. Li, B. Yang, Y. Yu, Ti^{3+} in the Surface of Titanium Dioxide: Generation, Properties and Photocatalytic Application, Hindawi J. Nanomat., 831524 (2012) 13.

[58] I. Musa, N. Qamhieh, S. T. Mahmoud, Synthesis and length dependent photoluminescence property of zinc oxide nanorods, Results Phys. 7 (2017) 3552–3556.

[59] S. Kuriakose, B. Satpati, S. Mohapatra, Enhanced photocatalytic activity of Co doped ZnO nanodisks and nanorods prepared by a facile wet chemical method, Phys. Chem. Chem. Phys. 16 (2014) 12741.